UNIVERSITÀ DEGLI STUDI DELL'AQUILA
DIPARTIMENTO DI INGEGNERIA E SCIENZE DELL’INFORMAZIONE E MATEMATICA

Dottorato di Ricerca in Matematica e modelli

XXXVI ciclo

Titolo della tesi

Variational Models for the Design and Diagnosis of the Evolution and Deterioration State of Concrete Dams

SSD ICAR/08

Dottorando

Angelo Scrofani

Coordinatore del corso
Prof. Davide Gabrielli

Tutor
Prof. Luca Placidi

a.a. 2022/2023

Variational models for the design and diagnosis of the evolution and deterioration state of concrete dams

Angelo Scrofani

Contents

List of Figures

Abstract

This research investigates the complex interplay between structural mechanics and material degradation in civil engineering and soil. The focus is on two primary areas: the long-term behaviour of concrete dams subjected to aging and the limitations of linear models in capturing seismic response. Aging-induced deterioration in concrete dams is primarily attributed to the diffusion of deleterious substances, which subsequently trigger internal chemical reactions. This study proposes a unified hemivariational framework for investigating damage and deformation in concrete dams subjected to aging-related processes. The model incorporates both one-dimensional (Timoshenko beam) and two-dimensional representations of the dam structure. A novel aspect of the proposed approach is the introduction of an "external distributed aging fluid influx pressure" as a dual of the concentration of the aging fluid. This pressure drives the inward diffusion of the aging agent, which is coupled with the evolution of damage. Parametric analyses are conducted to evaluate the influence of diffusivity and damage-concentration coupling term on the damage progression and service life prediction. The results indicate that the dam's shape significantly impacts stress distribution and, consequently, damage initiation and propagation. For the bi-dimensional case a more refined damage threshold is introduced to account for the distinct compressive and tensile behaviours of concrete. The proposed modelling approach provides a robust framework for assessing the long-term performance and safety of aging concrete dams, with potential applications in structural health monitoring and life cycle management. The same theory is also used to investigate a particular phenomenon we called *apparent* creep because the underlying mechanism is analogous to the processes occurring subsequent to classical creep deformations. This phenomenon, observed in a two-dimensional polymeric beam, exhibits characteristics akin to creep, as evidenced by numerical simulations demonstrating increased displacements under constant external loading conditions due to fluid ingress into the domain. The presence in soils of deteriorating fluids induce modifications of its mechanical characteristics. However, it is important to preliminary investigate. Additionally, one more research investigates the limitations of linear models in capturing the complex behaviour of geomaterials subjected to extreme loading conditions, such as those induced by seismic events. The research challenges the conventional linear paradigm in geophysics and civil engineering, particularly in the context of seismic events. This research investigates the influence of non-linear material behaviour on seismic response. A non-linear viscoelastic model is developed to capture large deformations near geological discontinuities, commonly observed in complex geological settings (such as those observed in the Aterno River Valley). Numerical simulations demonstrate the critical role of non-linearity in accurately predicting ground motion characteristics, including frequency content and amplitude. By combining these factors, the research provides a comprehensive framework for enhancing the reliability and accuracy of seismic hazard assessment and structural analysis. The findings contribute to

the development of advanced computational tools for mitigating seismic risk and ensuring the safety of critical infrastructure.

Chapter 1

Introduction

The monitoring of dams is a critical part of structural health monitoring, and as such, there has been continuous research efforts in investigating this issue [9, 28, 115, 199]. The mechanical integrity of dams may be affected by many phenomena: not only mechanical loads, but also the diffusion of particles, and the resulting chemical interactions. Indeed, the diffusion of particles may contribute to the nucleation and growth of microcracks inside the dam [68, 76, 197], thus motivating research efforts to model such diffusive phenomena [21]. More specifically, various types of diffusing species may be involved, leading to different effects. For example, moisture content may activate damage through creeping [112, 223, 225]. Aging phenomena may be activated [146] by an aging fluid spreading through the dam by capillary phenomena [17], or sorption of particles [41], resulting in chemical interactions between those aging elements and the dam material [47, 48, 57, 58, 62, 63, 174]. Gravity dams are critical infrastructures designed to hold back water by utilizing the weight of the structure itself to resist the hydraulic pressure. Constructed of concrete, these dams must endure various environmental and operational stressors over their service life. One significant concern in the long-term durability and safety of gravity dams is the phenomenon of aging due to fluid infiltration within the dam body. Fluid diffusion into concrete structures can induce several deleterious effects, including but not limited to, chemical reactions such as alkali-silica reaction (ASR), increased pore pressure, and freeze-thaw cycles. These processes collectively contribute to the deterioration of the mechanical properties of the dam, potentially compromising its structural integrity. The penetration of fluids can be driven by various factors, including the hydraulic gradient, the porosity of the concrete, and the presence of microcracks. Over time, this infiltration can lead to significant changes in the material properties of the concrete, such as increased permeability and reduced strength. Understanding the mechanisms of fluid transport within concrete and their impact on the aging of gravity dams is crucial for developing effective maintenance and rehabilitation strategies. This thesis aims to investigate the diffusion of fluids within concrete gravity dams, identify the key factors influencing this process and evaluate the consequent effects on the structural performance of the dams. To achieve these objectives a numerical simulations will be employed. The numerical simulations model the fluid transport and its impact on the dam structure over time, providing insights into the long-term behaviour of aging dams. The findings from this research will contribute to the development of more robust predictive models for the aging of concrete gravity dams, informing the design of more effective monitoring and maintenance programs to ensure their safety and functionality over extended periods.

Formulation of the problem

For the formulation of this problem, the classical kinematic descriptors (displacements and, possibly, rotations) are supplemented by the concentration of the aging fluid c within the body and the damage ω that describes its deterioration. The aging phenomenon is attributed to the diffusion of the aging fluid within the body, which reduces the material's stiffness as the damage variable evolves. The evolution of the damage variable is hypothesized to be governed by the diffusion process of the damaging fluid using a proper coupling term whose meaning will be thoroughly discussed in subsequent chapters of this work. Damage is an irreversible field whose value increases in time until the failure is reached. This phenomenon is represented by means of a scalar variable ω ranging from 0, denoting the undamaged case, to 1, denoting the complete failure. In order to describe the behaviour of the dam, at the first, the body $\mathcal{B}$ is modeled both as one-dimensional [51, 188] and bi-dimensional domain [187]. The variational principle [4, 73, 103, 122, 140, 157–159, 162, 168, 175, 213] is applied in order to obtain the Eulerian equations and the Karush Kuhn Tucker (KKT) condition. Because the damage ω is an entropic variable (ω is a no decreasing function in time) the variational approach to obtain the KKT conditions is characterized by an inequality and it is called hemi-variational approach [120, 121, 123, 124, 153, 156, 159, 161, 165, 210, 211]. The hemi-variation inequality will be better explained in the following sections for the one- and two-dimensional cases. Using the same theory, one more applications is presented: a specific **creep phenomenon**, called *apparent*. Furthermore, for a **geotechnical** point of view, the findings of this study will inform future research on the evolving mechanical behaviour of soils under seismic conditions influenced by diffusive substances.

Apparent creep

Creep in a polymeric beam has been studied. This creep is called *apparent* because it is induced by the presence of a fluid that, spreading within the body, affects the mechanical properties of the beam, thereby reducing its stiffness. The reduction in stiffness of the polymeric beam under investigation results in an increase in deformations under a constant load. The beam, modelled as a two-dimensional domain, was constrained on three sides and subjected to a uniformly distributed load on the remaining quarter one. The problem at hand is one of elastic damage, devoid of plastic effects. This implies that upon removal of the distributed load acting on the domain, deformations will diminish and vanish, despite the persistence of a damaged region within the domain. The reduction in stiffness is modelled analogously to the aging phenomenon investigated in the dam study (both mono and two-dimensional cases).

Earthquake

The diffusion theory presented in this work introduces a novel theoretical model with interesting potential applications in various scientific fields. In this context, we will focus on how the model can be used in the field of geotechnical engineering. The focal point of the future application for this model lies its ability to deal with materials with mechanical/elastic characteristics that change, in the presence of fluid, over time. This property makes it particularly suitable for studying soils subjected to fluid diffusion phenomena within them, which significantly alter their behaviour. The scientific literature offers numerous examples of geotechnical studies that are based on models of materials with time-varying properties [5, 7, 226] The mechanical characteristics of soils can be described by linear or non-linear relationships between stress and strain. The model developed in this thesis is able to capture both types of behaviour, allowing for a more complete and realistic analysis of geotechnical phenomena. In this first phase of analysis, we will focus on the effects of the non-linear characteristics of the soil. In particular, we will study how non-linearity influences the response of the soil to dynamic loads, the stability of slopes and foundations, and the propagation of seismic waves.

In subsequent studies, we propose to further investigate the time evolution of non-linear coefficients, considering the phenomena of consolidation, creep, and soil deterioration due to the presence of fluids. A non-linear study of seismic events was conducted, with particular attention to the seismic event that severely struck the city of L'Aquila in April 2009. This study stems from the desire to elucidate the significant contribution of non-linearities, under identical seismic intensity, when addressing seismic studies. The results obtained from the non-linear approach are compared with those obtained from a linear approach and experimental data. As demonstrated subsequently, the linear analysis, widely employed in seismic studies, is heavily afflicted by errors and inaccuracies. Non-linear analyses could provide an invaluable tool in the field of prevention and safeguarding human life. In this case, this diffusion theory would be employed to model not a decay but rather an improvement in mechanical properties. The application of the theoretical model developed in the thesis to the field of geotechnical engineering opens up new and interesting perspectives for understanding and predicting soil behaviour in the presence of fluids. The results of this research can provide valuable tools for the design of safer and more efficient civil engineering structures.

Chapter 2

Dam: 1-D Timoshenko beam model

For the type of complex coupled diffusion-deformation-damage phenomena being considered in this work, the beam model [92, 125, 126, 198] can serve as a feasible first step before considering the analysis of the more general 2-D and 3-D problems. The beam theory has, in general, wide interest in the literature of deformable solid bodies (see, for example, [34, 46, 69, 87, 131]) as well as in the modeling of the aging phenomenon [29, 30, 118, 195]. Several studies have also focused on the chemical interactions between the dam material (concrete) and the aging elements, for example silicates (see [47, 48, 57, 58, 62, 63, 174]). Recently some works have focused also on the deformation dependecy of the diffusion flux in solid [224] and polymeric gels or polymeric solids [114, 173]. In some formulations, e.g. [43], the damage evolution equation is assumed *ab initio* without a variational derivation or the consideration of the monolateral condition for the damage that is constrained to be a non-decreasing function of time.

In contrast, in [51] a hemivariatonal approach was considered for aging of concrete dams, in which one 3-D deformable body [22, 69] was modeled using a clamped Timoshenko beam model [15, 78, 79, 154, 221, 229]. However, the aging phenomenon was considered by decreasing arbitrarily a certain damage energy threshold. In particular a time dependent logarithmic law was used for describing the reduction of such a damage energy threshold. As a result the damage could increase with respect to time but it was not directly linked to the diffusion of deteriorating ions within the dam. Interrelationships between damage and these ions should be described by the use of proper coupling terms because of which the damage increases not only because of the external loads but also because of the presence of such a deteriorating fluid in the structure of the dam. Finally, a hemivariational approach is needed to model the irreversible and non-decreasing trend of the damage.

The aim of the present work is to use a variational approach [73, 103, 140, 157, 158, 161, 162, 168, 210], more specifically a hemivariational approach, in order to describe the aging phenomenon due to the spreading of aging fluid (for example, the salts) into the structure (concrete dam). The aging fluid can spread within the dam because imperfections are present in the concrete, such as through capillary phenomenon [17]. Following the approach first described in [51], a 1-D model is considered for the dam in this paper as well. The 3-D body is modeled as a 1-D Timoshenko beam which is subjected to several external loads due to (i) the pressure of the water, (ii) the self-weight of the dam and (iii) the *external distributed aging fluid influx pressure* that represents the dual of the fluid concentration. In this work, the damage threshold is linked with the concentration of the fluid by means of a proper damage-concentration coupling. During the analyzed dynamic case, although the external loads do not change, displacements and deformations evolve as consequence of the reduction of the values of the stiffnesses due to the increasing values of the damage resulting from diffusion. The latter concept will be better discussed in the section 2.2 where the energy functional is presented. The dissipation phenomena during aging is taken into account by means of the Rayleigh functional, as in [55, 105], but other methods can be considered (e.g in [53] where Dahl's model was used). As in [51], and also in this work, the concentration of the fluid is present within the energy functional. In addition parametric analyses are presented in order to explain the roles of the concentration-damage coupling and the diffusion coefficient. In conclusion, it is analyzed how the life of the dam changes when the previous parameters change.

2.1 Preliminary definitions

Body $\mathcal{B}$ is modeled as a 1-dimensional continuum [107, 108, 201] embedded in the 2-dimensional environment and its body points is characterized by means of the coordinate X in a given frame of reference. The set of kinematical descriptors, which depends upon the time t and the coordinate X, is composed of (i) the axial displacement $w = w(X,t)$, (ii) the transversal displacement $u = u(X,t)$, (iii) the rotation of the section $\vartheta = \vartheta(X,t)$, (iv) the concentration $c = c(X,t)$ of a fluid that is supposed to drive the damage evolution and (v) the damage field $\omega = \omega(X,t)$. The sign convention of the displacement components w and u and of the rotation ϑ are made explicit in Figure 2.1. Damage is an irreversible field whose value increases in time until the failure is reached. This phenomenon is represented by means of a scalar variable ω ranging from 0, denoting the undamaged case, to 1, denoting the complete failure.

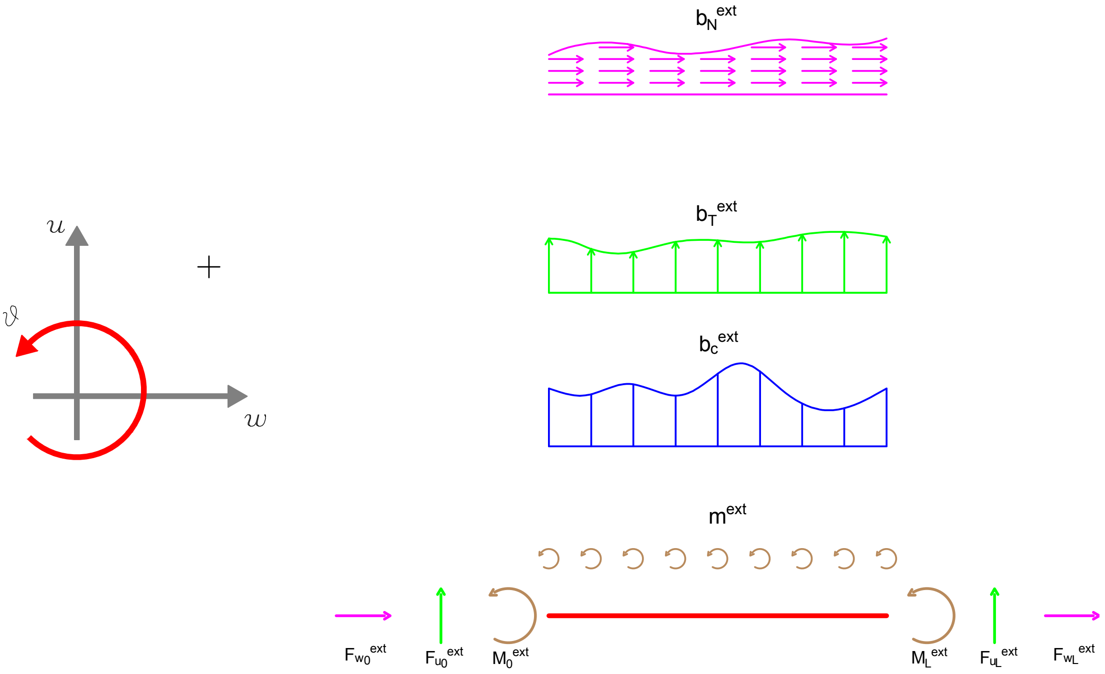

Figure 2.1: Signs convention

2.2 Total deformation energy functional

Let $\mathcal{E}(w, u, \vartheta, c, \omega)$ be the **total deformation energy functional**, which depends upon all the kinematical descriptors listed previously. We note that the kinematical descriptors, as written in subsection 2.1, are functions of the position X and the time t.

$$w(X,t),\ u(X,t),\ \vartheta(X,t),\ c(X,t),\ \omega(X,t) \qquad \forall (X,t) \in [0,L] \times [t_0, +\infty) \tag{2.1}$$

where L is the length of the beam and t_0 is the initial time. The total deformation energy functional is assumed to have the following form:

$$\begin{aligned}
\mathcal{E} =& \mathcal{E}(w,u,\vartheta,c,\omega) \\
=& \int_0^L \left[\frac{1}{2}K_N(1-\omega)\left(w'\right)^2 + \frac{1}{2}K_T(1-\omega)\left(u'-\vartheta\right)^2 + \frac{1}{2}K_M(1-\omega)\left(\vartheta'\right)^2\right] dX \\
&+ \int_0^L \left[\frac{1}{2}K_{DIF}(c')^2 + \frac{1}{2}K_F c^2 + K_{FN}cw' + K_{FT}c\left(u'-\vartheta\right) + K_{FM}c\vartheta'\right] dX \\
&- \int_0^L \left[b_N^{ext}w + b_T^{ext}u + m^{ext}\vartheta + b_c^{ext}c\right] dX - F_{c0}^{ext}c(0) - F_{cL}^{ext}c(L) \\
&- F_{w0}^{ext}w(0) - F_{wL}^{ext}w(L) - F_{u0}^{ext}u(0) - F_{uL}^{ext}u(L) - M_0^{ext}\vartheta(0) - M_L^{ext}\vartheta(L) \\
&+ \int_0^L \left[K_{\omega 0}\omega + K_{c\omega}c\omega + \frac{1}{2}K_\omega\omega^2\right] dX
\end{aligned} \tag{2.2}$$

where K_N, K_T, K_M are the axial, shear and bending stifnesses respectively, b_N^{ext} is the distributed external axial load (dual of w), b_T^{ext} is the distributed external shear load (dual of u), m^{ext} is the distributed external couples (dual of ϑ), b_c^{ext} is the external distributed aging fluid influx pressure (dual of c), F_{c0}^{ext} and F_{cL}^{ext} represent the external concentrated fluid sources at $X=0$ and at $X=L$ respectively, F_{w0}^{ext} and F_{wL}^{ext} represent the external concentrated axial loads at $X=0$ and at $X=L$ respectively, F_{u0}^{ext} and F_{uL}^{ext} represent the external concentrated shear loads at $X=0$ and at $X=L$ respectively and M_0^{ext} and M_L^{ext} represent the external concentrated couples at $X=0$ and at $X=L$ respectively (see Figure 2.1); besides K_{DIF} is a diffusion coefficient, K_F is the fluid elasticity, K_{FN} is the axial-fluid stiffness interaction, K_{FT} is the shear-fluid stiffness interaction, K_{FM} is the bending-fluid stiffness interaction. The terms $K_{\omega 0}$, $K_{c\omega}$ and K_ω represent the damage threshold, the concentration-damage coupling and the resistance to damage respectively. It is worth to notice that the damage is defined by a real variable ω that is no-decreasing in time. So that the following inequality is assumed:

$$\frac{\partial\omega}{\partial t} \geq 0 \qquad \forall X \in [0,L] \tag{2.3}$$

The above condition implies the necessity of a generalization of standard variational principle into a so-called hemivariational principle. For simplicity of notation let us define:

$$\begin{aligned}
\Lambda &= (w,u,\vartheta,c,\omega) & \dot{\Lambda} &= \left(\dot{w},\dot{u},\dot{\vartheta},\dot{c},\dot{\omega}\right) \\
\delta\Lambda &= (\delta w,\delta u,\delta\vartheta,\delta c,\delta\omega) & \Delta\Lambda &= (\Delta w,\Delta u,\Delta\vartheta,\Delta c,\Delta\omega)
\end{aligned} \tag{2.4}$$

where (i) Λ represents the set of the kinematical descriptors and (ii) $\dot{\Lambda}$, (iii) $\delta\Lambda$ and (iv) $\Delta\Lambda$ represent, respectively, the derivative with respect the time, the first variation and the increment of the Λ elements. It follows, trivially:

$$\Lambda + \delta\Lambda = (w+\delta w, u+\delta u, \vartheta+\delta\vartheta, c+\delta c,\ \omega+\delta\omega) \tag{2.5}$$

$$\Lambda + \Delta\Lambda = (w+\Delta w, u+\Delta u, \vartheta+\Delta\vartheta, c+\Delta c,\ \omega+\Delta\omega) \tag{2.6}$$

Furthermore, the subscript ω indicates the set:

$$\Lambda_\omega = \Lambda \backslash \{\omega\} = \{w, u, \vartheta, c\} \tag{2.7}$$

2.3 Hemivariational inequality principle

As in [161], a monotonically increasing time sequence $T_i \in \{T_i\}_{i=0}^n$ with $T_i \in \mathbb{R}_0^+$ and $n \in \mathbb{N}$ is introduced, including an initial and trivial datum (at $t_0 = T_0$) for each of the fundamental kinematical quantities. Let us consider the set of kinematically admissible placements and the kinematically admissible variations of the placements. Also note that the admissible variation of the irreversible kinematic quantity ω must be positive, hence:

$$\delta\omega \in \mathbb{R}_0^+ \tag{2.8}$$

Now, the first variation of the energy functional is calculated as follows:

$$\delta\mathcal{E}\left(\Lambda, \delta\Lambda\right) = \mathcal{E}\left(\Lambda + \delta\Lambda\right) - \mathcal{E}\left(\Lambda\right) \tag{2.9}$$

where the terms of order 2 or higher can be neglected. Let us consider that, at the i-th instant T_i, the increment of the fundamental kinematic quantities is calculated by the difference between these quantities as evaluated at the times T_i and T_{i-1}, namely:

$$\Delta\Lambda = \left(\Lambda\right)_{T_i} - \left(\Lambda\right)_{T_{i-1}} \tag{2.10}$$

and the increment of the energy functional has the consequent definition

$$\Delta\mathcal{E}\left(\Lambda, \Delta\Lambda\right) = \mathcal{E}\left(\Lambda + \Delta\Lambda\right) - \mathcal{E}\left(\Lambda\right) \tag{2.11}$$

As in (2.9) the terms of order 2 or higher can be neglected. The Rayleigh functional is a quadratic form of the velocity-fields,

$$\mathcal{R}(\dot{\Lambda}_\omega) = \frac{1}{2}c_w\dot{w}^2 + \frac{1}{2}c_u\dot{u}^2 + \frac{1}{2}c_\vartheta\dot{\vartheta}^2 + \frac{1}{2}c_c\dot{c}^2 \tag{2.12}$$

and its variation and increment, respectively, are defined as follows:

$$\delta\mathcal{R}\left(\dot{\Lambda}_\omega, \delta\Lambda_\omega\right) = \int_0^L \left[c_w\dot{w}\delta w + c_u\dot{u}\delta u + c_\vartheta\dot{\vartheta}\delta\vartheta + c_c\dot{c}\delta c\right] dX \tag{2.13}$$

$$\Delta\mathcal{R}\left(\dot{\Lambda}_\omega, \Delta\Lambda_\omega\right) = \int_0^L \left[c_w\dot{w}\Delta w + c_u\dot{u}\Delta u + c_\vartheta\dot{\vartheta}\Delta\vartheta + c_c\dot{c}\Delta c\right] dX \tag{2.14}$$

In order to get governing equations for this newly introduced model, we assume that the motion $w(X,t)$, $u(X,t)$, $\vartheta(X,t)$, $c(X,t)$ and $\omega(X,t)$ verifies the following hemivariational principle:

$$\Delta\mathcal{E}\left(\Lambda, \Delta\Lambda\right) + \Delta\mathcal{R}\left(\dot{\Lambda}_\omega, \Delta\Lambda_\omega\right) \leq \delta\mathcal{E}\left(\Lambda, \delta\Lambda\right) + \delta\mathcal{R}\left(\dot{\Lambda}_\omega, \delta\Lambda_\omega\right) \tag{2.15}$$

for any admissible variation $\delta\Lambda$, $\delta\Lambda_\omega$ of the fundamental kinematic quantities. The variational principle implies Euler–Lagrange equations of different types:

(i) a system of partial differential equations for a non homogeneous Timoshenko beam with the reduced stiffnesses due to damage and with a modified stress free reference configuration due to the fluid concentration (i.e. $K_{FN}c$ modifies the axial force, $K_{FT}c$ modifies the shear force and $K_{FM}c$ modifies the bending moment):

$$N' + b_N^{ext} = c_w \dot{w} \tag{2.16}$$
$$V' + b_T^{ext} = c_u \dot{u} \tag{2.17}$$
$$V + M_b' + m^{ext} = c_\vartheta \dot{\vartheta} \tag{2.18}$$

with the following definition:

$$N = K_N(1-\omega)w' + K_{FN}c \tag{2.19}$$
$$V = K_T(1-\omega)(u' - \vartheta) + K_{FT}c \tag{2.20}$$
$$M_b = K_M(1-\omega)\vartheta' + K_{FM}c \tag{2.21}$$

and where N, V, and M_b represent the normal force, the shear force and the bending moment respectively.

(ii) a differential equation for the diffusion of the fluid that is characterized not only by the external distributed aging fluid influx pressure b_c^{ext} but also by deformations (i.e. by the axial deformation $K_{FN}w'$, by the shear deformation $K_{FT}(u' - \vartheta)$ and by the bending deformation $K_{FM}\vartheta'$), by the concentration itself $K_F c$ and by damage $K_{c\omega}\omega$,

$$[K_{DIF}c']' + b_c^{ext} = c_c \dot{c} + K_{FN}w' + K_{FT}(u' - \vartheta) + K_{FM}\vartheta' + K_F c + K_{c\omega}\omega \tag{2.22}$$

(iii) a proper set of boundary conditions that yield:

$$\left[N - F_{wL}^{ext}\right]\delta w = 0, \qquad X = L \tag{2.23}$$
$$\left[N + F_{w0}^{ext}\right]\delta w = 0, \qquad X = 0 \tag{2.24}$$
$$\left[V - F_{uL}^{ext}\right]\delta u = 0, \qquad X = L \tag{2.25}$$
$$\left[V + F_{u0}^{ext}\right]\delta u = 0, \qquad X = 0 \tag{2.26}$$
$$\left[M_b - M_L^{ext}\right]\delta \vartheta = 0, \qquad X = L \tag{2.27}$$
$$\left[M_b + M_0^{ext}\right]\delta \vartheta = 0, \qquad X = 0 \tag{2.28}$$
$$\left[K_{DIF}c' - F_{cL}^{ext}\right]\delta c = 0, \qquad X = L \tag{2.29}$$
$$\left[K_{DIF}c' + F_{c0}^{ext}\right]\delta c = 0, \qquad X = 0 \tag{2.30}$$

(iv) and a Karush Kuhn Tucker (KKT) condition

$$[\omega - \omega_T]\,\Delta\omega = 0, \quad \forall X \in [0, L] \tag{2.31}$$

where

$$\omega_T(X,t) = \left[\frac{1}{2}\frac{K_N}{K_\omega}(w')^2 + \frac{1}{2}\frac{K_T}{K_\omega}(u' - \vartheta)^2 + \frac{1}{2}\frac{K_M}{K_\omega}(\vartheta')^2\right] - \left[\frac{K_{\omega 0}}{K_\omega} + \frac{c \cdot K_{c\omega}}{K_\omega}\right] \tag{2.32}$$

From KKT conditions and from the initial undamaged condition $\omega(X,0) = 0$, the damage variable ω starts to increase when the *normalized undamaged strain energy*

$$\frac{1}{2}\frac{K_N}{K_\omega}(w')^2 + \frac{1}{2}\frac{K_T}{K_\omega}(u' - \vartheta)^2 + \frac{1}{2}\frac{K_M}{K_\omega}(\vartheta')^2 \tag{2.33}$$

reaches the *normalized undamaged energy threshold*

$$\frac{K_{\omega 0}}{K_\omega} + \frac{c \cdot K_{c\omega}}{K_\omega} \tag{2.34}$$

For the fluid to have an aging effect, the following restriction on the coupling term applies

$$K_{c\omega} < 0 \tag{2.35}$$

Note that from (2.32) this restriction will result in the reduction of the energy threshold. Further thermodynamic restrictions are due to the needed positive definiteness of the strain energy. It is worth to note that, among such conditions we also have

$$K_{c\omega}^2 < K_\omega K_F \tag{2.36}$$

2.4 Beam representation of dam

The dam is usually conceived to have a trapezoidal shape, in a 2-D model, and clamped at the bottom. It is, therefore, modelled here by means of a **cantilever beam** as shown in the Figure 2.2 in which the external and triangular distributed loads are considered due to both the water pressure and the self-weight. According to the model presented in [51] the geometry that is shown in Figure 2.2, the water is on the left-hand side and the air is on the right-hand side. As shown in the Figure 2.2 the red line (the geometric locus of the middle points of the sections) represents the 1-D beam by means of which the dam is modeled. In Figure 2.2, β and β' are the angles between the vertical line and, respectively, the 1-D beam and the left-hand side oblique surface of the dam. Thus, passing to the 1-D model, the weight of the dam must be considered on the mean line (the red line) as a triangular distributed external load (with both normal and orthogonal components) while the pressure of the water, because it is applied to the oblique surface of the dam, must be considered not only as a triangular distributed external load (with both normal and orthogonal components) but also as a triangular distributed external couple.

Because the concentration of the fluid is affected by its pressure, it is reasonable to think that the distribution of the external distributed aging fluid influx is higher at the bottom of the dam. In the considered model the water height L_w is equal to that of the dam L_d. Hence, in the 1-D model a triangular distribution of b_c^{ext} is considered which has the higher value at the clamped end (for $X = 0$) and zero value at the top (for $X = \frac{L}{\cos\beta}$) as it will be shown in (2.40). The water presure is due to Stevino's law, it is directed orthogonal by to the left-hand side of the trapezoidal shape and the maximum value is p_w. The self-weight is directed vertically and the maximum value is W, in formulas,

$$p_w = \gamma_w g L_w \qquad \text{and} \qquad W = \gamma_c g L_d \tag{2.37}$$

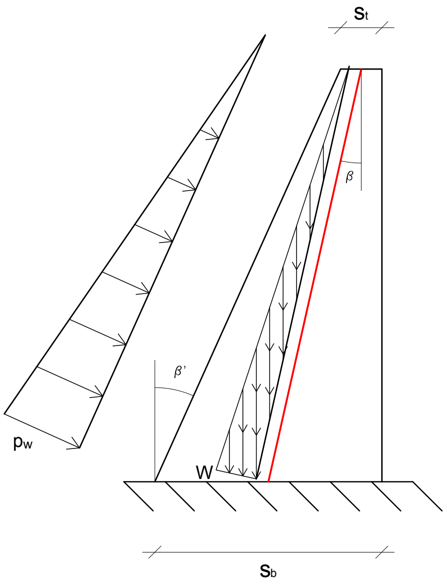

Figure 2.2: Dam profile

Where γ_w and γ_c represent the mass density of the water and of the concrete, respectively. Notice that the weight of the dam is a distributed load on the domain while the pressure of the water is on the upstream facet (i.e., on the left-hand side of the trapezoidal shape) of the dam.

2.4.1 Stiffnesses identification

The stifness of a given material is defined both by the Lamé coefficients λ and μ or by the Young's modulus E and the Poisson's ratio ν. First of all we recall their relations,

$$\lambda = \frac{E \cdot \nu}{(1+\nu)(1-2\nu)}, \qquad \mu = \frac{E}{2(1+\nu)}. \tag{2.38}$$

Thus, it is possible, as in [190], to identify the axial, shear and bending stiffnesses K_N, K_T and K_M as follows

$$\begin{aligned} K_N(X) =& \frac{4\mu(\lambda+\mu)}{\lambda+2\mu} s(X) \cdot t_h \\ K_T(X) =& \frac{2}{3}\mu \cdot s(X) \cdot t_h \\ K_M(X) =& \frac{4\mu(\lambda+\mu)}{\lambda+2\mu} \frac{[s(X)]^3}{12} \cdot t_h \end{aligned} \tag{2.39}$$

Where t_h is the depth, i.e. the out of plane dimension of Figure 2.2 of the dam and where a rectangular cross-section is considered.

2.4.2 The distributed external loads

By assuming that b_c^{ext} is proportional to the pressure of the water and, therefore, it has a triangular distribution

$$b_c^{ext}(X) = b_{c,max}^{ext}\left(1 - \frac{X}{L_w}\right) \cdot H\left(L_w - X \cdot \cos\tilde{\beta}\right), \tag{2.40}$$

then, following the considerations about the weigth of the dam and the pressure of the water at the beginning of the section 2.4, the distributed external loads must be decomposed along the parallel and transverse directions of the beam as in [51]:

$$\begin{aligned} b_N^{ext}(X) = &- t_h\gamma_w \sin\left(\tilde{\beta}' - \tilde{\beta}\right)\left(L_w - X \cdot \cos\tilde{\beta}\right) \cdot H\left(L_w - X \cdot \cos\tilde{\beta}\right) \\ &- \gamma_c t_h s(X)\cos\tilde{\beta}, \end{aligned} \tag{2.41}$$

$$\begin{aligned} b_T^{ext}(X) = &- t_h\gamma_w \sin\left(\tilde{\beta}' + \tilde{\beta}\right)\left(L_w - X \cdot \cos\tilde{\beta}\right) \cdot H\left(L_w - X \cdot \cos\tilde{\beta}\right) \\ &- \gamma_c t_h s(X)\sin\tilde{\beta}, \end{aligned} \tag{2.42}$$

and the external distributed couple is

$$m^{ext}(X) = \frac{1}{2} t_h s(X)\gamma_w\left(L_w - X \cdot \cos\tilde{\beta}\right) \cdot H\left(L_w - X \cdot \cos\tilde{\beta}\right) \tag{2.43}$$

Where (i) X is the abscissa of the beam, (ii) L_w is the height of the water, (iii) s_t and s_b, represented in Figure 2.2, are the thickness at the top and at the bottom section of the dam respectively, (iv) γ_c and γ_w are the density of the materials (as shown in the (2.37)), and (v) the subscripts c and w are refered to concrete and water, respectively. Finally, the function $H(\zeta)$ is the Heaviside function to set to zero the contribution of water pressure above its maximum elevation, i.e.,

$$H(\zeta) = \begin{cases} 1 & \zeta \geq 0 \\ 0 & \zeta < 0 \end{cases} \tag{2.44}$$

2.5 Numerical investigation

The developed model is applied to perform parametric analyses by varying the values of K_{DIF} and $K_{c\omega}$ and for different spatial distributions of b_c^{ext}.

2.5.1 Uncoupled concentration c and the kinematic descriptors w, u, ϑ case

Consdering that concrete dam deformations (w', $u' - \vartheta$ and ϑ'), from (2.19), (2.20) and (2.21), are not expected to be affected by the density of the aging fluid. In the presented analyses, all the coupling terms K_{FN}, K_{FT}, K_{FM} are considered negligible.

$$K_{FN} = 0\,\frac{\mathrm{J}}{\mathrm{kg}}, \qquad K_{FT} = 0\,\frac{\mathrm{J}}{\mathrm{kg}}, \qquad K_{FM} = 0\,\frac{\mathrm{m}^3}{\mathrm{s}^2}. \tag{2.45}$$

In this case, the dam does not have a sponge-like behaviour, which could be of interest for many other porous materials. The considered structural model and loading is shown in the Figure 2.3 and the adopted parameters are reported in Tabel 2.1.

$L_d = L_w = 10\,\mathrm{m}$	$b^{ext}_{c,max} = 5 \cdot 10^5\,\frac{\mathrm{J}}{\mathrm{kg}}$
$s_t = 1\,\mathrm{m}$	$K_{DIF} = 10^5\,\frac{\mathrm{m}^5}{\mathrm{kg{\cdot}s^2}}$
$s_b = 3\,\mathrm{m}$	$K_F = 10^7\,\frac{\mathrm{m}^3}{\mathrm{kg{\cdot}s^2}}$
$\tilde{\beta} = \arctan\left(\frac{s_b - s_t}{2L}\right) = 0.1\,\mathrm{rad}$	$c_c = 10^{16}\,\frac{\mathrm{m}^3}{\mathrm{kg}}$
$\tilde{\beta}' = \arctan\left(\frac{s_b - s_t}{L}\right) = 0.2\,\mathrm{rad}$	$K_{c\omega} = -9 \cdot 10^5\,\frac{\mathrm{J}}{\mathrm{kg}}$
$L = \frac{L_d}{cos\tilde{\beta}} = 10.05\,\mathrm{m}$	$K_{\omega 0} = 800\,\mathrm{N}$
$E = 4 \cdot 10^4\,\mathrm{MPa}$	$K_\omega = 10^5\mathrm{N}$
$t_h = 1\,m$	$\gamma_w = 10\,\frac{\mathrm{kg}}{\mathrm{m}^3}$
$\nu = 0.2$	$\gamma_c = 24\,\frac{\mathrm{kg}}{\mathrm{m}^3}$
$\lambda = 1.1 \cdot 10^{10}\mathrm{MPa}$	$t_f = 3 \cdot 10^9\,\mathrm{s} \approx 95\ years$
$\mu = 1.67 \cdot 10^{10}\mathrm{MPa}$	

Table 2.1: Parameters for numerical investigation

where L_d is the height of the dam and L is the length of the equivalent beam. The values of the paramateres are chosen according to [51]. However, two parametric analyzes have been performed for the values of the new parameters K_{DIF} and $K_{c\omega}$. The results are shown in the section (2.5.3) and (2.5.4). All the analyzes have been carried out using the FEM software Comsol considering the following (i) kinematic boundary conditions:

$$w(0,t) = 0, \quad u(0,t) = 0, \quad \vartheta(0,t) = 0 \tag{2.46}$$

and (ii) initial values

$$w(X,0) = 0, \qquad u(X,0) = 0, \qquad \vartheta(X,0) = 0. \tag{2.47}$$

The value of the damage threshold ω_T, for each time step, is prescribed in (2.32). The value of damage ω at a given time is taken to be the maximum between ω_T and the value of ω at the previous time step to update step-by-step according the KKT condition (2.32). It is noted that the KKT condition imposes the constraint that the damage is always increases in time, so that the monolateral condiction for the damage ω is met. Figures 2.4, 2.5 and 2.6 give the results of this analysis. It is worth noting that the kinematical descriptors w, u, and ϑ evolve in time not because of the increase in the external loads, but because of the increase of damage ω, which results in the reduced values of the stiffnesses K_N, K_T and K_M

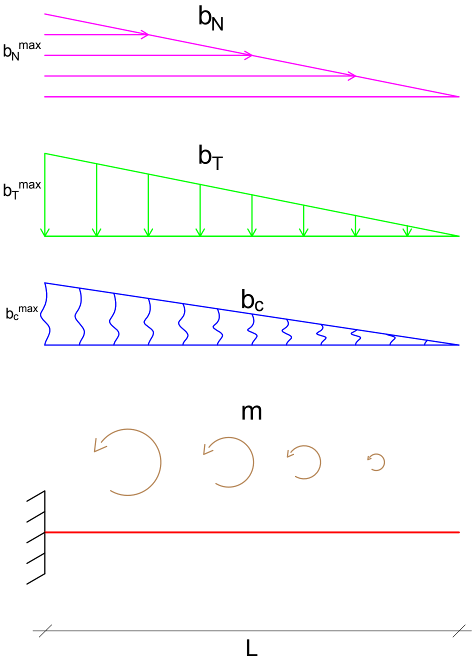

Figure 2.3: Cantilever beam model

in (2.19), (2.20) and (2.21). The negative values of w for $X > 0$ shown in the Figure 2.4a is reasonable because of the considered external gravity load. This results in the loss of strength of the dam.

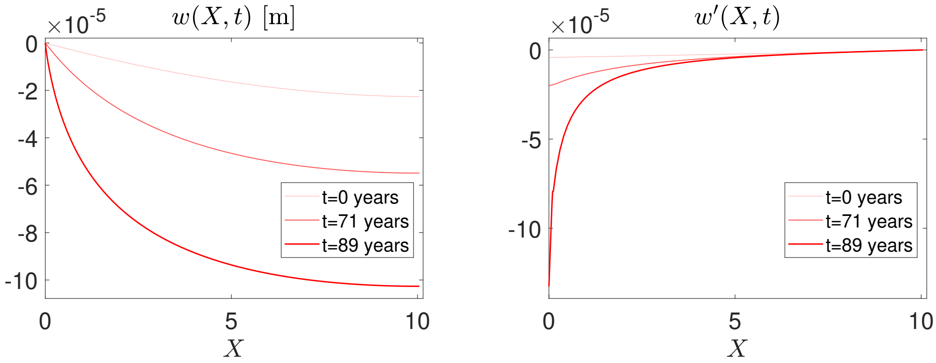

(a)

(b)

Figure 2.4: (a) Axial displacement $w(X, t)$ and (b) strain $w'(X, t)$. The evolution in time of the kinematic quantities by a color gradient is represented. The aging evolution is represented from the lightest color to the most defined one.

Thus, the axial deformation w' is, as shown in Figure 2.4b negative near the base (at $X = 0$) and null at the free side at $X = L$. The modulus of both the axial displacement and deformation are increasing functions of time. Similar observations are made for the transverse displacement from Figure 2.5a and the shear deformation in Figure 2.5b, and for the rotation 2.6a and the curvature 2.6b.

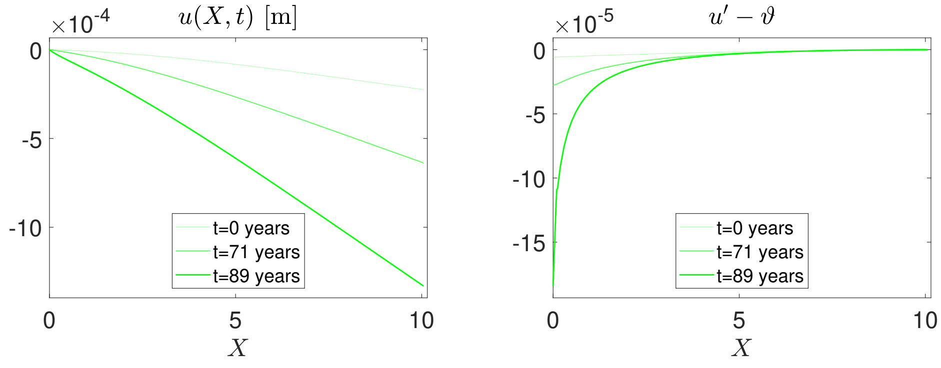

(a) (b)

Figure 2.5: (a) Transversal displacement $u(X,t)$ and (b) shear deformation $u' - \vartheta$. The evolution in time of the kinematic quantities by a color gradient is represented. The aging evolution is represented from the lightest color to the most defined one.

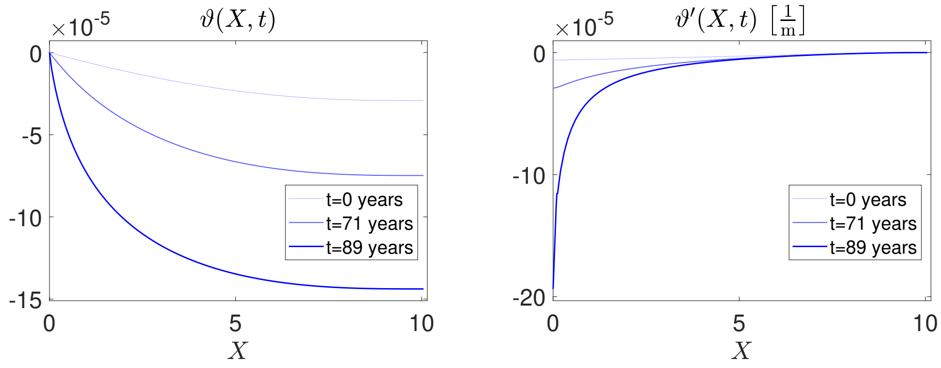

(a) (b)

Figure 2.6: (a) Rotation of the sections $\vartheta(X,t)$ and (b) curvature ϑ'. The evolution in time of the kinematic quantities by a color gradient is represented. The aging evolution is represented from the lightest color to the most defined one.

The concentration of the aging fluid and the damage are shown in the Figures 2.7a and 2.7b. It can be seen that the aging fluid concentration and the damage, because they are coupled by the term $K_{c\omega}$, are both higher at the bottom of the beam at $X = 0$. So, if one increases, the other one increases as well. Finally, it is worth to note that, once damage reaches the unity value (at $X = 0$), the collapse of the dam is expected.

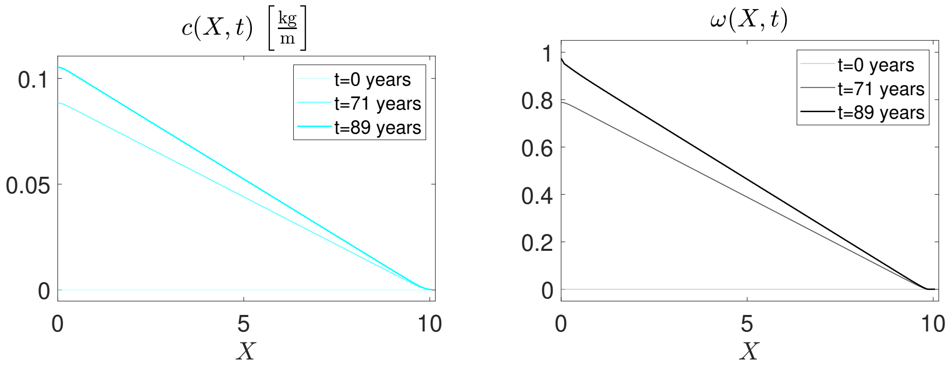

(a) (b)

Figure 2.7: (a) Concentration $c(X,t)$ and (b) damage $\omega(X,t)$. The evolution in time of the kinematic quantities by a color gradient is represented. The aging evolution is represented from the lightest color to the most defined one.

2.5.2 Parametric analysis: distribution of b_c^{ext}

In this subsection, we evalaute the behaviour of the beam subjected to different b_c^{ext} distributions. The real distribution of b_c^{ext} is not known without measurements. Thus, we consider different distributions for demonstrating the potential effects. In order to compare the results with the triangular case the integral of b_c^{ext} on the domain remains the same as that of the previous triangular case. Here as an exemple, the externally distributed aging fluid influx pressure has been considered having an half gaussian curve distribution (see the Figure (2.8)). The half gaussian curve has the peak at $X = 0$. The parameters of the half gaussian distribution is such that:

$$\int_0^L \left[b_{c,triangular}^{ext}\right] dX = \int_0^L \left[b_{c,gaussian}^{ext}\right] dX \tag{2.48}$$

The three different gaussian distributions (with three different maximum values at $X = 0$) and the triangular distribution are compared, in Figure 2.8.

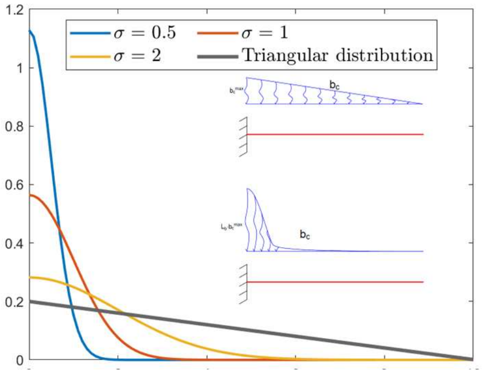

Figure 2.8: Three different gaussian distribution with different σ and the triangular one of b_c^{ext}

It is worthwhile to notice that, for the gaussian distribution, the maximum value of the externally distributed aging fluid influx pressure is $L \cdot b^{ext}_{c,max}$, where L is the length of the beam:

$$\int_0^L \left[b^{ext}_{c,max} \cdot triang(X)\right] dX = \int_0^L \left[L \cdot b^{ext}_{c,max} \cdot gauss(X)\right] dX = b^{ext}_{c,max} \cdot \frac{L}{2} \tag{2.49}$$

where (i) $triang(X) = 1 - \frac{X}{L}$ represents the triangular distribution and (ii) $gauss(X) = \frac{1}{\sigma\sqrt{2\pi}} e^{-\frac{1}{2}\left(\frac{X}{\sigma}\right)^2}$ the gaussian one. Because the considered distribution is an half gaussian curve, we have:

$$\int_0^L \left[gauss(X)\right] dX \approx \frac{1}{2} \tag{2.50}$$

The results for different values of standard deviation $\sigma = \left\{\frac{1}{2},\, 1,\, 2\right\}$ are shown in Figures 2.9, 2.10 and 2.11 for the same values of other parameters, the same of that of the section 2.5.1. In the Figure 2.9 the case with $\sigma = \frac{1}{2}$ is shown.

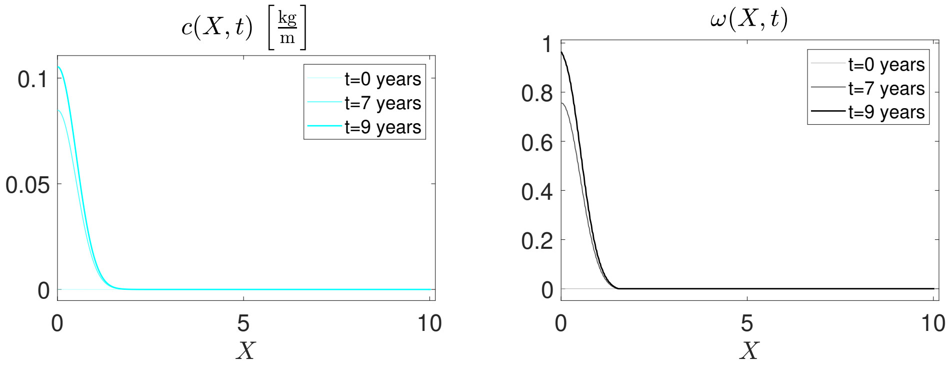

(a) (b)

Figure 2.9: Plot of:(a) concentration $c(X,t)$ and (b) damage $\omega(X,t)$ for $\sigma = \frac{1}{2}$. The evolution in time of the kinematic quantities by a color gradient is represented. The aging evolution is represented from the lightest color to the most defined one.

In the Figure 2.10 the case with $\sigma = 1$ is shown.

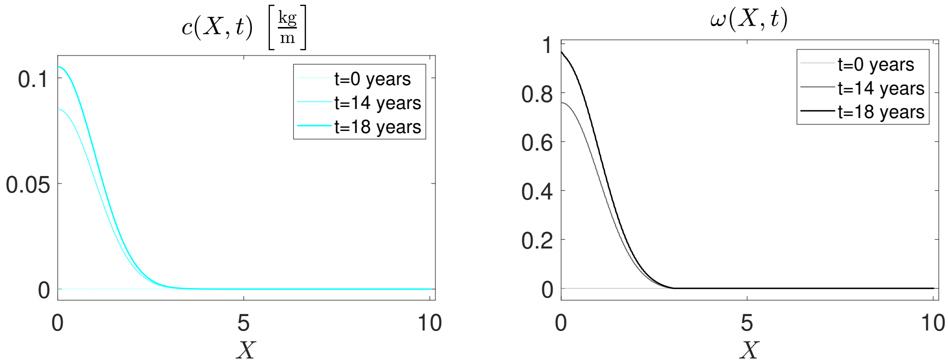

(a) (b)

Figure 2.10: Plot of:(a) concentration $c(X,t)$ and (b) damage $\omega(X,t)$ for $\sigma = 1$. The evolution in time of the kinematic quantities by a color gradient is represented. The aging evolution is represented from the lightest color to the most defined one.

In the Figure 2.11 the case with $\sigma = 2$ are shown.

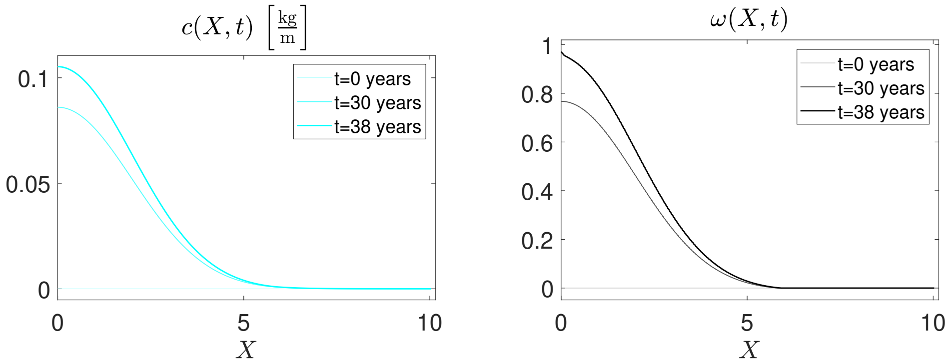

(a) (b)

Figure 2.11: Plot of:(a) concentration $c(X,t)$ and (b) damage $\omega(X,t)$ for $\sigma = 2$. The evolution in time of the kinematic quantities by a color gradient is represented. The aging evolution is represented from the lightest color to the most defined one.

As expected, when σ increases, we show a trend to the triangular case. These results prove that the higher is the concentration of the aging fluid in one part of the beam, the lower is the life time of the dam..

2.5.3 Parametric analysis: K_{DIF}

In this section concentration c and damage ω are evaluated for different values of K_{DIF} such that its role can be better clarified. Four different values of K_{DIF} are considered in Figures 2.12, 2.13, 2.14 and 2.15 by increasing one order of magnitude compared to the previous one, as follows:

$$K_{DIF} = \left\{10^3,\ 10^5,\ 10^7,\ 10^9\right\} \frac{\mathrm{m}^5}{\mathrm{kg}\cdot\mathrm{s}^2}$$

All the other parameters are equal to that given in section 2.5.1.

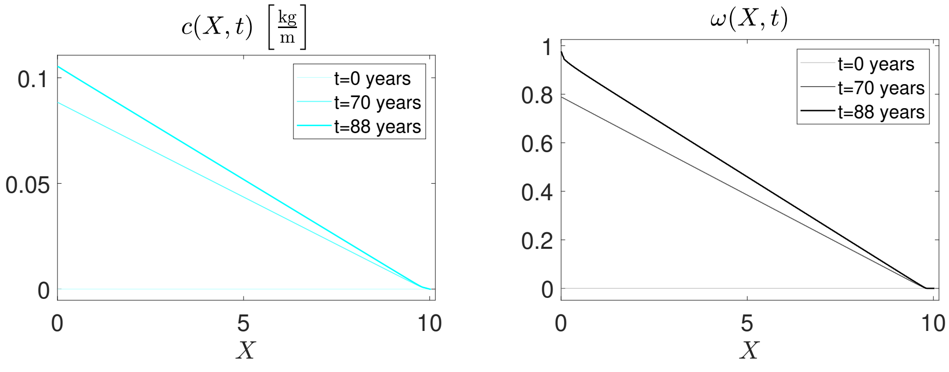

(a) (b)

Figure 2.12: Plot of:(a) concentration $c(X,t)$ and (b) damage $\omega(X,t)$ for $K_{DIF} = 10^3 \frac{\mathrm{m}^5}{\mathrm{kg}\cdot\mathrm{s}^2}$. The evolution in time of the kinematic quantities by a color gradient is represented. The aging evolution is represented from the lightest color to the most defined one.

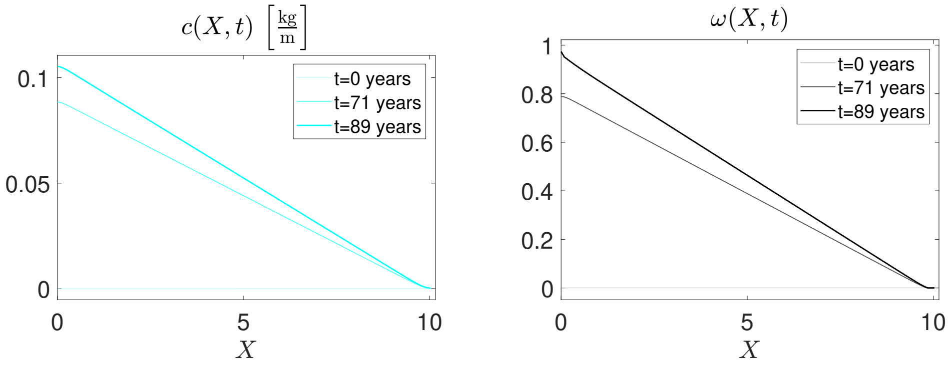

(a) (b)

Figure 2.13: Plot of:(a) concentration $c(X,t)$ and (b) damage $\omega(X,t)$ for $K_{DIF} = 10^5 \frac{\mathrm{m}^5}{\mathrm{kg}\cdot\mathrm{s}^2}$. The evolution in time of the kinematic quantities by a color gradient is represented. The aging evolution is represented from the lightest color to the most defined one.

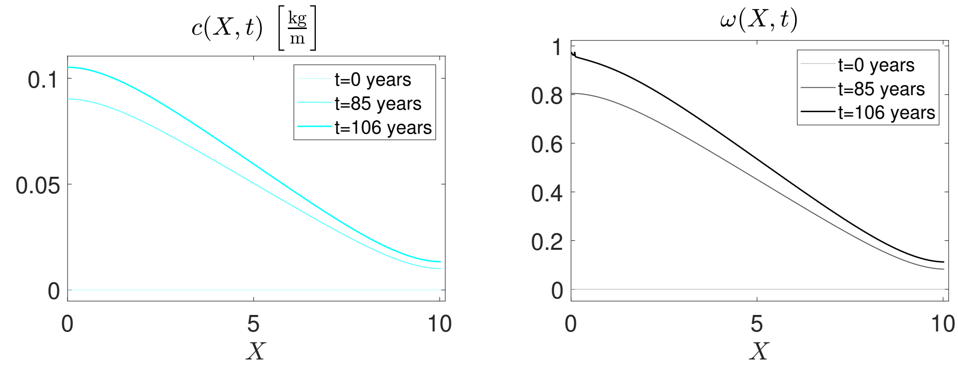

(a) (b)

Figure 2.14: Plot of:(a) concentration $c(X,t)$ and (b) damage $\omega(X,t)$ for $K_{DIF} = 10^7 \frac{\mathrm{m}^5}{\mathrm{kg \cdot s}^2}$. The evolution in time of the kinematic quantities by a color gradient is represented. The aging evolution is represented from the lightest color to the most defined one.

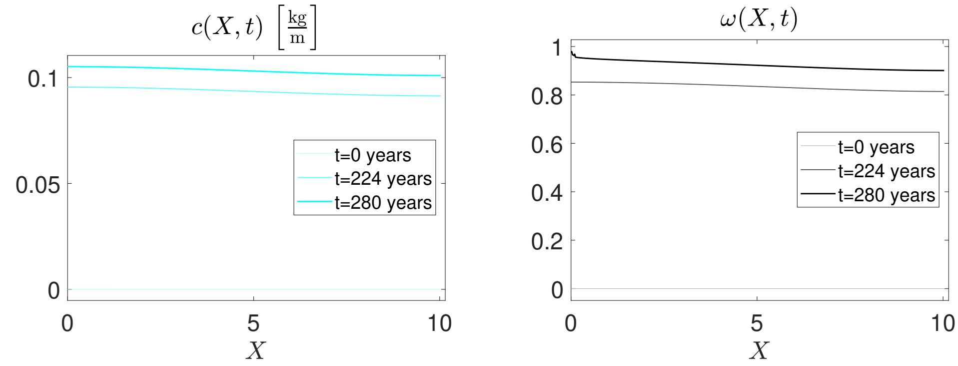

(a) (b)

Figure 2.15: Plot of:(a) concentration $c(X,t)$ and (b) damage $\omega(X,t)$ for $K_{DIF} = 10^9 \frac{\mathrm{m}^5}{\mathrm{kg \cdot s}^2}$. The evolution in time of the kinematic quantities by a color gradient is represented. The aging evolution is represented from the lightest color to the most defined one.

The results in the Figures 2.12, 2.13, 2.14 and 2.15 confirm the interpration of K_{DIF} as a ***diffusivity coefficient***. Indeed, when K_{DIF} is higher the aging fluid spreads easier into the whole body redistributing, at the same time, the damage. In particular, from Figure 2.15, the highest value of K_{DIF} induced the fluid to spread freely and rapidly within the body. The concentration (and the damage) distribution tend therefore to have a rectangular shape. It means that the damage is now longer localized in a small area of the botom of the beam and the life of the dam increases for a given b_c^{ext} distribution. This means that the failure is reached later and the life of the dam increases when the diffusivity is larger. The reason for different values of K_{DIF} may be due, for example, to the quality of the concrete. The sulfate attacks could cause an increase in porosity by allowing fluid to flow more easily within the beam. However, although the poor quality of the concrete implies higher K_{DIF}, the concentration will be more uniformally distributed and therefore the age at which damage reaches 1 is delayed.

2.5.4 Parametric analysis: $K_{c\omega}$

We have already pointed out in (2.34) that the normalized undamaged energy threshold is decreased by a negative value of the concentration-damage coupling term. Thus, a parametric analysis for different values of $K_{c\omega}$ is worth to be done that will be analyzed in Figure 2.16. The considered values of $K_{c\omega}$ are:

$$K_{c\omega} = \{-9.5, \quad -9, \quad -8.5, \quad -8\} \cdot 10^5 \frac{\mathrm{J}}{\mathrm{kg}}$$

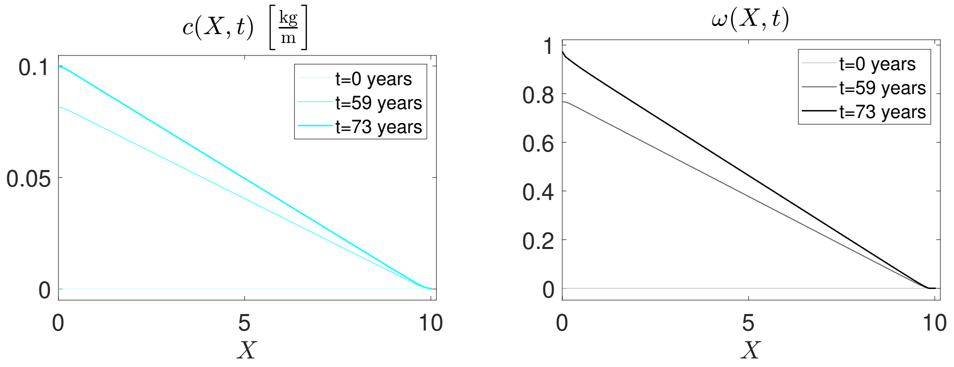

(a) (b)

Figure 2.16: Plot of:(a) concentration $c(X,t)$ (a) and damage $\omega(X,t)$ (b) for $K_{c\omega} = -9.5 \cdot 10^5 \frac{\mathrm{J}}{\mathrm{kg}}$. The evolution in time of the kinematic quantities by a color gradient is represented. The aging evolution is represented from the lightest color to the most defined one.

As the value of $K_{c\omega}$ varies, the behavior of the structure remains the same but the time for reaching the damage ($\omega = 1$) increases. In particular, we observe that the higher is the modulus of such a coupling term, the higher is the transmission of the influence of the concentration of the aging fluid on damage and the lower is the life of the dam.

2.5.5 Dam's life

As a result of the parametric analyses in sections 2.5.3 and 2.5.4 it is possible to analyze how the life of the dam is affected by the diffusivity characteristics and the diffusion-deformation-damage coupling. The dam's life for the triangular distribution of the external distributed aging fluid influx pressure b_c^{ext} and several values of K_{DIF} and $K_{c\omega}$ are shown in the Figures 2.17 and 2.18.

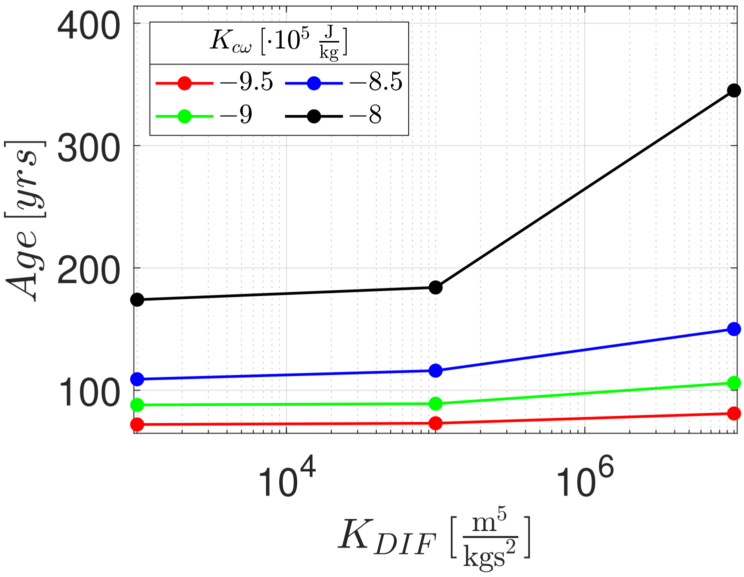

Figure 2.17: Parametric analysis for K_{DIF}

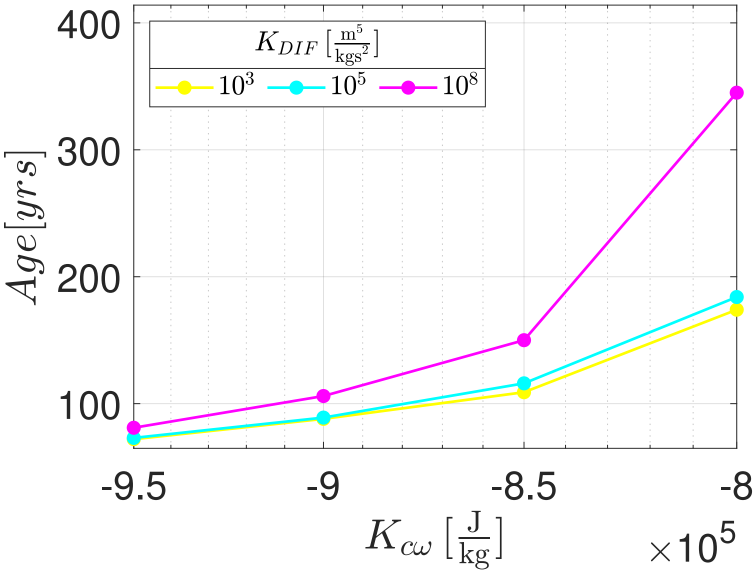

Figure 2.18: Parametric analysis for $K_{c\omega}$

The results shown in the Figures 2.17 and 2.18 show that if the values of K_{DIF} and $K_{c\omega}$ are higher, the dam's life increases. Furthermore Figures 2.18 shows that the damage is sensitive to changes in the value of the coupling term $K_{c\omega}$.

Chapter 3

Dam: 2-D case

The present work is a continuation of previous research efforts to model the deformation and aging-related damage of concrete dams. A one-dimensional model of a shear deformable beam (widely used in literature [65, 100]) has been proposed earlier in [51, 188], and is here extended to a bi-dimensional model. The considered modelling approach lies within the framework of variational principles [73, 103, 140, 157, 158, 162], applied to the derivation of balance equations for generalized continuum models, which involve in a non-classical way the dual quantities of the kinematic ones describing the strain of the continuum [74]. Among those generalised continua, higher-gradient continua have been studied and applied to modelling non-local elastic effects, by taking into account the derivatives of the considered strain tensor in the deformation energy. As a consequence, such models are able to account for phenomena which cannot be seen by classical Cauchy continua [3, 26, 178]. Thus, strain-gradient continua have been used extensively for modelling metamaterials, i.e. synthetic materials specifically engineered to have exotic behaviours resulting from their microstructure [25, 71, 72, 75, 86]. The physical-mathematical model is formulated in Sect. 3.1 and 3.2 as a 2-D problem: the kinematic description is introduced, before defining energy functionals to model the considered phenomena, and then a hemivariational inequality principle is used to formulate the mathematical problem. Then, numerical investigations are carried out and presented in Sect. 3.5 for bodies having two different cross sections.

3.1 Preliminary definition

For the bi-dimensional case, the dam is modeled as a 2-D continuum body $\mathcal{B}$. Its points are characterized by means of the coordinates $\mathbf{X} = X_i \hat{\mathbf{e}}_i$ (where $\|\hat{\mathbf{e}}_i\| = 1$ and $i = 1, 2$) in a given reference configuration. The set of the kinematical descriptors which depend upon X_i and t is composed of (i) the horizontal displacement $u_1\,(X_1, X_2, t)$, (ii) the vertical displacement $u_2\,(X_1, X_2, t)$, (iii) the concentration of a fluid $c\,(X_1, X_2, t)$ and (iv) the damage $\omega\,(X_1, X_2, t)$. The damage, whose evolution is supposed driven by the concentration of the aging fluid c, is a no-decreasing in time irreversible field and it is represented by means of a scalar variable ω raging from 0 (denoting the undamaged state) to 1 (denoting the attainment of the failure). Let $\mathbf{u} = \mathbf{u}(\mathbf{X}, t) = u_i \hat{\mathbf{e}}_i$ (where $\|\hat{\mathbf{e}}_i\| = 1$ and $i = 1, 2$) be the displacement vector, $\boldsymbol{\Phi}\left(\mathbf{X}, t\right)$ is the placement function, $\mathbb{F}$ is the deformation gradient tensor and $\mathbb{G}$ is the Green strain tensor. Indicating with $\mathbf{x} = x_i \hat{\mathbf{e}}_i$ the coordinates, in the current configuration, of the point having coordinates $\mathbf{X}$ in the reference configuration, one has

$$\mathbf{x} = \boldsymbol{\Phi}\left(\mathbf{X}, t\right) = \mathbf{X} + \mathbf{u}, \qquad \mathbb{F} = \nabla \boldsymbol{\Phi}, \qquad \mathbb{G} = \frac{1}{2}\left(\mathbb{F}^T \mathbb{F} - \mathbb{I}\right) \tag{3.1}$$

or, in index notation:

$$x_i = \Phi_i = X_i + u_i, \qquad F_{ij} = \frac{\partial \Phi_i}{\partial X_j} = u_{i,j} + \delta_{ij}, \qquad G_{ij} = \frac{1}{2}\left(F_{ki} F_{kj} - \delta_{ij}\right) \tag{3.2}$$

where

$$u_{i,j} = \frac{\partial u_i}{\partial X_j} \qquad \text{and} \qquad \delta_{ij} = \begin{cases} 1 & i = j \\ 0 & i \neq j \end{cases} \tag{3.3}$$

In terms of the displacement u_i the Green Lagrange strain tensor is:

$$G_{ij} = \frac{1}{2}\left(u_{i,j} + u_{j,i} + u_{h,i} u_{h,j}\right) \tag{3.4}$$

Indicating with U the internal deformation energy density, it is worth note that the stress σ_{ij} and hyperstress T_{ijh} are:

$$\sigma_{ij} = \frac{\partial U}{\partial G_{ij}} = \frac{\partial U}{\partial G_{ji}} = \sigma_{ji} \qquad \text{and} \qquad T_{ijh} = \frac{\partial U}{\partial G_{ij,h}} = \frac{\partial U}{\partial G_{ji,h}} = T_{jih}, \tag{3.5}$$

3.2 Total deformation energy functional

From the [168, 188, 228] the energy functional can be splitted, as in the following, in three part.

(i) The elastic part:

$$\begin{aligned} \mathcal{E}_e(u, \omega) = & \int_{\mathcal{B}} \left[U\left(\mathbb{G}, \nabla \mathbb{G}, \omega\right) - \mathbf{b}^{ext} \cdot \mathbf{u} - \mathbb{M}^{ext} : \nabla \mathbf{u}\right] dA \\ & - \int_{\partial \mathcal{B}} \left[\mathbf{t}^{ext} \cdot \mathbf{u} + \tau^{ext} \cdot \left[\left(\nabla \mathbf{u}\right) \mathbf{n}\right]\right] ds - \int_{\partial \partial \mathcal{B}} \mathbf{f}^{ext} \cdot \mathbf{u}, \end{aligned} \tag{3.6}$$

where $\mathbf{b}^{ext}$ represents the external body force (i.e., per unit area) whereas $\mathbb{M}^{ext}$ represents the external body double force (i.e.,per unit area) and the operator : represents the scalar product between tensors. So that:

$$\mathbb{M}^{ext} : \nabla \mathbf{u} = M_{ij} u_{i,j} \tag{3.7}$$

Instead $\mathbf{t}^{ext}$ and τ^{ext} represent, respectively, the external force and double force per unit length, so they act on the boundary of the domain, denoted as $\partial \mathcal{B}$. The vector $\mathbf{f}^{ext}$, instead, represents the concentrated external force applied on the vertexes, which is the boundary of the boundary denoted as $\partial \partial \mathcal{B}$.

(ii) The diffusion part:

$$\mathcal{E}_c(c) = \int_{\mathcal{B}} \left[\frac{1}{2}K^{DIF}\|\nabla c\|^2 + \frac{1}{2}K_F c^2\right] dA - \int_{\partial\mathcal{B}} \left[b_c^{ext} c\right] ds \tag{3.8}$$

where K^{DIF}, K_F and b_c^{ext} represent the diffusivity of the body, its fluid elasticity and the external distributed aging influx pressure, respectively.

(iii) The dissipative part:

$$\mathcal{E}_\omega(c,\omega) = \int_{\mathcal{B}} \left[K_{\omega 0}\omega + K_{c\omega}c\omega + \frac{1}{2}K_\omega \omega^2\right] dA. \tag{3.9}$$

where $K_{\omega 0}$, $K_{c\omega}$ and K_ω represent the damage threshold, the concentration-damage coupling term and the resistance to damage. Noting that the threshold $K_{\omega 0}$ depends upon the strain state assuming, therefore, different value either in tension or in compression, so as to represent reasonably the behaviour of the concrete. Hence:

$$K_{\omega 0} = \bar{K}_{\omega 0}\left[1 + (\xi - 1)\, H\left(-\mathrm{tr}\mathbb{G}\right)\right] \tag{3.10}$$

where $\bar{K}_{\omega 0}$ is the smaller value of the threshold associated with the tensile state, $tr\mathbb{G}$ (namely the trace of the strain tensor $\mathbb{G}$) represents a measure of the strain state of the body $\mathcal{B}$, ξ is the amplification factor that increases the threshold value and $H(\bullet)$ is the Heaviside function whose value is equal to 0, when its argument is negative, or 1, when its argument is greater or equal than 0. That means that:

$$K_{\omega 0} = \begin{cases} \bar{K}_{\omega 0} & \text{in tension} \\ \xi\bar{K}_{\omega 0} & \text{in comprension} \end{cases} \tag{3.11}$$

The heaviside function is a powerfull tool because it allows us to change the value of the threshold for each case, both in tension or in compression, leaving these terms as a costant which multiplies the descriptor ω. This means that using this kind of function the variation does not change.

So, the energy functional $\mathcal{E}$ is assumed to be additively decomposed in the equations (3.6), (3.8) and (3.9):

$$\begin{aligned}
\mathcal{E}(u,c,\omega) =& \mathcal{E}_e(u,\omega) + \mathcal{E}_c(c) + \mathcal{E}_\omega(c,\omega) \\
=& \int_{\mathcal{B}} \left[U_e\left(\mathbb{G}, \nabla\mathbb{G}, \omega\right) - \mathbf{b}^{ext}\cdot\mathbf{u} - \mathbb{M}^{ext} : \nabla\mathbf{u}\right] dA \\
&+ \int_{\mathcal{B}} \left[\frac{1}{2}K^{DIF}\|\nabla c\|^2 + \frac{1}{2}K_F\,(c)^2\right] dA \\
&- \int_{\partial\mathcal{B}} \left[\mathbf{t}^{ext}\cdot\mathbf{u} + \tau^{ext}\cdot\left[(\nabla\mathbf{u})\,\mathbf{n}\right]\right] ds - \int_{\partial\mathcal{B}} \left[\mathbf{b_c}^{ext} c\right] ds - \int_{\partial\partial\mathcal{B}} \mathbf{f}^{ext}\cdot\mathbf{u} \\
&+ \int_{\mathcal{B}} \left[K_{\omega 0}\omega + K_{c\omega}c\omega + \frac{1}{2}K_\omega\omega^2\right] dA.
\end{aligned} \tag{3.12}$$

and its variation, in index notation, is:

$$
\begin{aligned}
\delta\mathcal{E}(u,c,\omega) =& \delta\mathcal{E}_e(u,\omega)+\delta\mathcal{E}_c(c)+\delta\mathcal{E}_\omega(c,\omega)\\
=& -\int_{\mathcal{B}}\left[\left(\sigma_{ij,j}-T_{ijh,hj}+b_i^{ext}-M_{ij,j}^{ext}\right)\delta u_i\right]dA\\
&-\int_{\mathcal{B}}\left[\left(K^{DIFF}c_{,i}c_{,i}+K_F c+K_{c\omega}\omega\right)\delta c\right]dA\\
&+\int_{\partial\mathcal{B}}\left[\left(t_i-t_i^{ext}-m_{ij}^{ext}n_j\right)\delta u_i\right]ds\\
&+\int_{\partial\mathcal{B}}\left[\left(\tau_i-\tau_i^{ext}\right)n_k\delta u_{i,k}\right]ds\\
&+\int_{\partial\mathcal{B}}\left[\left(K^{DIF}c_{,i}n_j-b_c^{ext}\right)\delta c\right]ds\\
&+\int_{\partial\partial\mathcal{B}}\left[f_i-f_i^{ext}\right]\delta u_i\\
&+\int_{\mathcal{B}}\left[\left(\frac{\partial U_e}{\partial\omega}+K_{\omega 0}+K_{c\omega}c+K_\omega\omega\right)\delta\omega\right]dA.
\end{aligned}
\tag{3.13}
$$

where

$$
t_i=\left[\sigma_{ij}-T_{ijh,h}\right]n_j-\left(T_{ijh}n_hP_{jk}\right)_{,l}P_{jl},\;\tau_i=T_{ijh}n_hn_j,\;f_i=T_{ijh}V_{hj} \tag{3.14}
$$

where, as in [168], $P_{ij}=\delta_{ij}-n_in_j$ is the tangetial projector operator, n_i and n_j are the boundary-normal unit vector $V_{hj}=n_h^lv_j^l+n_h^rv_j^r$ is the vertex operator and v_j represent the external tangent vector. The superscript l and r are referred to the *left* and *right* side of a vertex-point in which a concentrated force would be applied. The damage is defined by a a no-decreasing in time real variable ω. So that, the following inequality is assumed:

$$
\frac{\partial\omega}{\partial t}\geq 0 \qquad \forall\mathbf{X}\in\mathcal{B} \tag{3.15}
$$

The Rayleigh functional, that in this work is linked only with the fluid concentration parameters, is a quadratic form of the velocity-fields

$$
\mathcal{R}(\dot{c})=\int_{\mathcal{B}}\left[\frac{1}{2}c_c\dot{c}^2\right]dA \tag{3.16}
$$

and its variation and increment indicated, respectively, by the symbol $\tilde{\delta}$ and $\tilde{\Delta}$, are assumed as follows:

$$
\tilde{\delta}\mathcal{R}\left(\dot{c},\delta c\right)=\int_{\mathcal{B}}\left[c_c\dot{c}\delta c\right]dA \tag{3.17}
$$

$$
\tilde{\Delta}\mathcal{R}\left(\dot{c},\Delta c\right)=\int_{\mathcal{B}}\left[c_c\dot{c}\Delta c\right]dA \tag{3.18}
$$

As in [188] the condition (3.15) implies the necessity of a generalization of the standard variational principle in the so-called hemivariational principle. Let us introduce the following sets of parameters:

$$\begin{aligned}\Lambda &= (u_1, u_2, c, \omega)\\ \delta\Lambda &= (\delta u_1, \delta u_2, \delta c, \delta\omega)\\ \Delta\Lambda &= (\Delta u_1, \Delta u_2, \Delta c, \Delta\omega)\end{aligned} \tag{3.19}$$

where (i) Λ represents the set of the kinematical descriptors and (ii) $\delta\Lambda$ and (iii) $\Delta\Lambda$ represent, respectively, the first variation and the increment of the elements of Λ. It follows, trivially:

$$\Lambda + \delta\Lambda = (u_1 + \delta u_1, u_2 + \delta u_2, c + \delta c,\ \omega + \delta\omega) \tag{3.20}$$

$$\Lambda + \Delta\Lambda = (u_1 + \Delta u_1, u_2 + \Delta u_2, c + \Delta c,\ \omega + \Delta\omega) \tag{3.21}$$

Furthermore, by the subscript ω it is indicated the set:

$$\Lambda_\omega = \Lambda - \{\omega\} = \{u_1, u_2, c\} \tag{3.22}$$

3.3 Hemivariational inequality principle

As in [161], a monotonically increasing time sequence $T_i \in \{T_i\}_{i=0}^n$ with $T_i \in \mathbb{R}_0^+$ and $n \in \mathbb{N}$ is introduced, considering an initial and trivial datum (at $t_0 = T_0$) for each of the fundamental kinematical quantities. Let us consider the set of kinematically admissible placements and the kinematically admissible variations of the placements. Also noting that, from (3.15), the admissible variation of the irreversible kinematic quantity ω must not be negative, hence:

$$\delta\omega \in \mathbb{R}_0^+ \tag{3.23}$$

Now, the first variation of the energy functional is calculated as follows:

$$\delta\mathcal{E}(\Lambda, \delta\Lambda) = \mathcal{E}(\Lambda + \delta\Lambda) - \mathcal{E}(\Lambda) \tag{3.24}$$

where the terms of order 2 or higher can be neglected. Let us consider that, at the i-th istant T_i, the increment of the fundamental kinematic quantities is calculated by the difference between these quantities as evaluated at the times T_i and T_{i-1}, namely:

$$\Delta\Lambda = (\Lambda)_{T_i} - (\Lambda)_{T_{i-1}} \tag{3.25}$$

and the increment of the energy functional has the consequent definition

$$\Delta\mathcal{E}(\Lambda, \Delta\Lambda) = \mathcal{E}(\Lambda + \Delta\Lambda) - \mathcal{E}(\Lambda) \tag{3.26}$$

As in (3.24) the terms of order 2 or higher can be neglected. In order to get governing equations for this newly introduced model, we assume that the motion $u_1(X_1, X_2, t)$, $u_2(X_1, X_2, t)$, $c(X_1, X_2, t)$ and $\omega(X_1, X_2, t)$ verifies the following hemivariational principle:

$$\Delta\mathcal{E}\left(\Lambda,\Delta\Lambda\right)+\tilde{\Delta}\mathcal{R}\left(\dot{c},\Delta\Lambda_{\omega}\right)\leq\delta\mathcal{E}\left(\Lambda,\delta\Lambda\right)+\tilde{\delta}\mathcal{R}\left(\dot{c},\delta\Lambda_{\omega}\right) \tag{3.27}$$

for any admissible variation $\delta\Lambda$, $\delta\Lambda_{\omega}$ of the fundamental kinematic quantities. The variational principle (for $i=1,2$) implies the Euler–Lagrange equations of different type:(i) a system of partial differential equations for the equilibrium

$$\sigma_{ij,j}-T_{ijh,hj}+b_i^{ext}-M_{ij,j}^{ext}=0, \tag{3.28}$$

(ii) a differential equation for the diffusion

$$K^{DIFF}c_{,i}c_{,i}+K_Fc+K_{c\omega}\omega=c_c\dot{c} \tag{3.29}$$

and (iii) the following set of boundary conditions:

$$\begin{aligned}
\left[t_i-t_i^{ext}-m_{ij}n_j\right]\delta u_i&=0 \qquad \forall\mathbf{X}\in\partial\mathcal{B} &(3.30)\\
\left[\left(\tau_i-\tau_i^{ext}\right)n_k\right]\delta u_{i,k}&=0 \qquad \forall\mathbf{X}\in\partial\mathcal{B} &(3.31)\\
\left[K^{DIFF}c_{,i}n_j-b_c^{ext}\right]\delta c&=0 \qquad \forall\mathbf{X}\in\partial\mathcal{B} &(3.32)\\
\left[f_i-f_i^{ext}\right]\delta u_i&=0 \qquad \forall\mathbf{X}\in\partial\partial\mathcal{B} &(3.33)
\end{aligned}$$

It is worth noting that the term $\frac{K^{DIFF}}{c_c}$ has the role of the diffusion coefficient for the classical diffusion equation.

3.4 2-D isotropic quadratic internal deformation energy density functional

The elastic part of the internal deformation energy density functional U_e of a isotropic second gradient material is provided in [138]:

$$\begin{aligned}
U_e\left(\mathbb{G},\nabla\mathbb{G},\omega\right)=&\frac{\lambda}{2}G_{ii}G_{jj}+\mu G_{ij}G_{ji}+4\alpha_1G_{ii,j}G_{jh,h}+\alpha_2G_{ii,j}G_{kk,j}\\
&+4\alpha_3G_{ij,i}G_{kj,k}+2\alpha_4G_{ij,k}G_{ij,k}+4\alpha_5G_{ij,k}G_{ik,j}
\end{aligned} \tag{3.34}$$

where λ,μ and $\alpha_i\in\mathbb{R}$ are parameteres defined as follows:

$$\begin{aligned}
\lambda=\left(1-\omega\right)\lambda_0,\ \mu=&\left(1-\omega\right)\mu_0 \text{ and } \alpha_i=\left(1+n\omega\right)\alpha_i^0\\
n\in&\left[-1,+\infty\right),\ i=\{1,2,3,4,5\}
\end{aligned} \tag{3.35}$$

λ_0 and μ_0 are the Lamé parameters and the α_i^0's are the Mindlin coefficient which are linked with the characteristic length and the Young's modulus. It is worth notice that the stiffnesses are affected by the damage, whose increasing reduces them resistance contribution. From the (3.35) and citing [168], the parameter n is a weight for the damage which ranges from -1 to infinite, i.e., $n\in[-1,+\infty)$. The case $n=-1$ is related to the fracture because no elastic energy can be accumulated in the completely cracked region [160]. The case $n=0$ means that coefficients α_i does not depend upon on the damage ω, this corresponds to the case where the damage does not affect the characteristic length scales of the material. The (3.34) becomes:

$$
\begin{aligned}
U_e(\mathbb{G}, \nabla\mathbb{G}, \omega) = & \left(\frac{\lambda}{2} + \mu\right) \left(G_{11}^2 + G_{22}^2\right) + \lambda G_{11} G_{22} + 2\mu G_{12}^2 \\
& + \left(G_{11,1}^2 + G_{22,2}^2\right) (4\alpha_1 + \alpha_2 + 4\alpha_3 + 2\alpha_4 + 4\alpha_5) \\
& + (G_{11,1} G_{12,2} + G_{12,1} G_{22,2}) (4\alpha_1 + 8\alpha_3) \\
& + (G_{11,2} G_{12,1} + G_{12,2} G_{22,1}) (4\alpha_1 + 8\alpha_5) \\
& + (G_{11,2} G_{22,2} + G_{11,1} G_{22,1}) (4\alpha_1 + 2\alpha_2) \\
& + \left(G_{11,2}^2 + G_{22,1}^2\right) (\alpha_2 + 2\alpha_4) \\
& + \left(G_{12,1}^2 + G_{12,2}^2\right) (4\alpha_3 + 4\alpha_4 + 4\alpha_5)
\end{aligned}
\tag{3.36}
$$

The α_i^0s parameters are identified, as in [23] , in the following way:

$$
\begin{aligned}
\alpha_1^0 &= \frac{L^2}{112} \lambda_0 \\
\alpha_2^0 &= \frac{L^2}{112} \lambda_0 \\
\alpha_3^0 &= \frac{L^2}{1120} (7\mu_0 + 3\lambda_0) \\
\alpha_4^0 &= \frac{L^2}{1120} (7\mu_0 - 4\lambda_0) \\
\alpha_5^0 &= \frac{L^2}{1120} (7\mu_0 + 3\lambda_0)
\end{aligned}
\tag{3.37}
$$

If only the self weight $\mathbb{W}$, the pressure of the water p and the influx pressure b_c^{ext} act on the body, the internal energy functional in (3.12) becomes:

$$
\begin{aligned}
\mathcal{E} = &\int_{\mathcal{B}} \left[\left(\frac{\lambda}{2} + \mu \right) \left(G_{11}^2 + G_{22}^2 \right) + \lambda G_{11} G_{22} + 2\mu G_{12}^2 \right] dA \\
&+ \int_{\mathcal{B}} \left[\left(G_{11,1}^2 + G_{22,2}^2 \right) \left(4\alpha_1 + \alpha_2 + 4\alpha_3 + 2\alpha_4 + 4\alpha_5 \right) \right] dA \\
&+ \int_{\mathcal{B}} \left[\left(G_{11,1} G_{12,2} + G_{12,1} G_{22,2} \right) \left(4\alpha_1 + 8\alpha_3 \right) \right] dA \\
&+ \int_{\mathcal{B}} \left[\left(G_{11,2} G_{12,1} + G_{12,2} G_{22,1} \right) \left(4\alpha_1 + 8\alpha_5 \right) \right] dA \\
&+ \int_{\mathcal{B}} \left[\left(G_{11,2} G_{22,2} + G_{11,1} G_{22,1} \right) \left(4\alpha_1 + 2\alpha_2 \right) \right] dA \\
&+ \int_{\mathcal{B}} \left[\left(G_{11,2}^2 + G_{22,1}^2 \right) \left(\alpha_2 + 2\alpha_4 \right) \right] dA \\
&+ \int_{\mathcal{B}} \left[\left(G_{12,1}^2 + G_{12,2}^2 \right) \left(4\alpha_3 + 4\alpha_4 + 4\alpha_5 \right) \right] dA \\
&+ \int_{\mathcal{B}} \left[\frac{1}{2} K^{DIF} \|\nabla c\|^2 + \frac{1}{2} K_F c^2 \right] dA \\
&+ \int_{\mathcal{B}} \left[K_{\omega 0} \omega + K_{c\omega} c \omega + \frac{1}{2} K_\omega \omega^2 \right] dA \\
&- \int_{\mathcal{B}} \left[\rho g u_2 \right] dA - \int_{\partial\mathcal{B}} \left[p \left(\mathbf{u} \cdot \mathbf{n} \right) + b_c^{ext} c \right] ds
\end{aligned}
\tag{3.38}
$$

where ρ, g and $\mathbf{n}$ are, respectively, the density of the body $\mathcal{B}$, the gravity acceleration and the unit normal vector of the boundary where the action of the pressure of the water acts. From the Karush-Kuhn-Tucker and the (3.15), the damage is obtained:

$$
\begin{aligned}
\tilde{\omega}\left(X,t\right) = &\frac{1}{K_\omega} \left\{ \left(\frac{\lambda_0}{2} + \mu_0 \right) \left(G_{11}^2 + G_{22}^2 \right) + \lambda_0 G_{11} G_{22} + 2\mu_0 G_{12}^2 \right. \\
&- n \left[\left(G_{11,1}^2 + G_{22,2}^2 \right) \left(4\alpha_1^0 + \alpha_2^0 + 4\alpha_3^0 + 2\alpha_4^0 + 4\alpha_5^0 \right) \right. \\
&+ \left(G_{11,1} G_{12,2} + G_{12,1} G_{22,2} \right) \left(4\alpha_1^0 + 8\alpha_3^0 \right) \\
&+ \left(G_{11,2} G_{12,1} + G_{12,2} G_{22,1} \right) \left(4\alpha_1^0 + 8\alpha_5^0 \right) \\
&+ \left(G_{11,2} G_{22,2} + G_{11,1} G_{22,1} \right) \left(4\alpha_1^0 + 2\alpha_2^0 \right) \\
&+ \left(G_{11,2}^2 + G_{22,1}^2 \right) \left(\alpha_2^0 + 2\alpha_4^0 \right) \\
&\left. \left. + \left(G_{12,1}^2 + G_{12,2}^2 \right) \left(4\alpha_3^0 + 4\alpha_4^0 + 4\alpha_5^0 \right) \right] \right\} \\
&- \frac{1}{K_\omega} \left\{ K_{\omega_0} + K_{c\omega} \cdot c \right\}
\end{aligned}
\tag{3.39}
$$

In order to have an aging effect $K_{c\omega}$ has to be negative. Such a condition is necessary to enable the reduction of the threshold with increasing concentration, as in (3.39). Clearly in order to obtain the monolateral behaviour of ω, numerically, the following condition is imposed:

$$
\dot{\tilde{\omega}} < 0 \Longrightarrow \dot{\tilde{\omega}} = 0 \tag{3.40}
$$

Or, equivalently:

$$\tilde{\omega}\left(X_1, X_2, T_i\right) < \tilde{\omega}\left(X_1, X_2, T_{i-1}\right) \Longrightarrow \tilde{\omega}\left(X_1, X_2, T_i\right) = \tilde{\omega}\left(X_1, X_2, T_{i-1}\right) \quad (3.41)$$

3.5 Numerical investigation

In the following numerical example two cases are shown for two different shape of the body $\mathcal{B}$. In the first case the body is modeled using a rectangular shape while in the second case the shape chosen is that of the realistic gravity dam having the same area of the rectangular model. In both of the cases the water is in the left-hand side. The models, either the rectangular one and the dam one, are shown in the Fig. 3.1

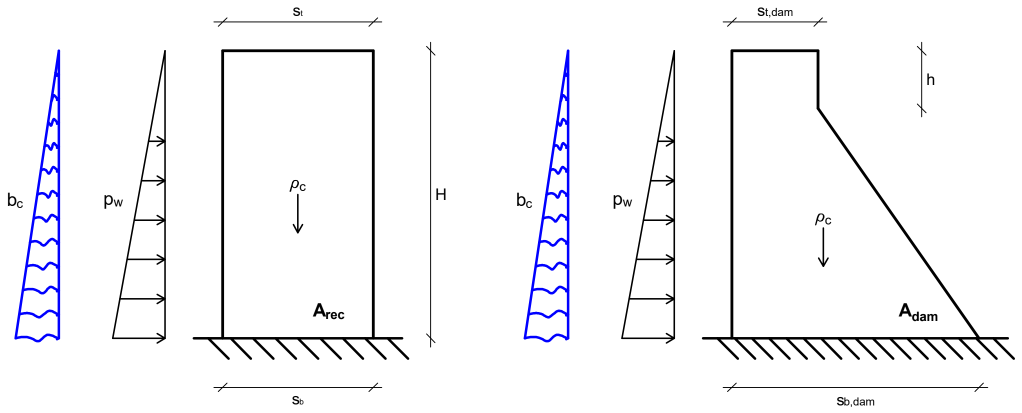

Figure 3.1: Model and boundary conditions for the rectangular shape (left hand side) and the dam shape (right hand side)

where ρ_c is the mass density of the body $\mathcal{B}$, p_w is the pressure of the water, H is the height of the body, h is the height of the crest of the dam and, clearly, the areas (A_{rec} for the rectangular case and A_{dam} for the dam case) respect the condition:

$$A_{rec} = A_{dam}.$$

In the Table 3.1 the 2-D case parameters used for the analysis are shown. It is assumed that the aging fluid diffuses into the structure from the left side and it is reasonable to think that the distribution of the dual of the concentration b_c is considered triangular at the boundary as well as that of the pressure of the water. So that:

$$b_c^{ext} = b_c^{ext}\left(X_2\right) = \bar{b}_c^{ext} \frac{L - X_2}{L} \quad (3.42)$$

where $\bar{b}_c^{ext}$ is a costant and represents the maximun value of the external distributed aging influx pressure b_c^{ext}

$H_d = 10$ m	$\xi = 10$
$H_w = 10$ m	$\bar{b}_c^{ext} = 10^{13}\frac{\mathrm{m}^2}{\mathrm{s}^2}$
$s_t = 5.24$ m	$c_c = 10^{21}\frac{\mathrm{m}^4}{\mathrm{kg}}$
$s_b = 5.24$ m	$K_F = 10^{10}\ \frac{\mathrm{m}^4}{\mathrm{kg}\cdot\mathrm{s}^2}$
$s_{t,dam} = 3$ m	$K_{c\omega} = -1\ \frac{\mathrm{m}^2}{\mathrm{s}^2}$
$s_{b,dam} = 8.6$ m	$\bar{K}_{\omega 0} = 4\ \frac{\mathrm{N}}{\mathrm{m}}$
$h = 2$ m	$K_\omega = 1\frac{\mathrm{N}}{\mathrm{m}}$
$E = 4 \cdot 10^{10}\frac{\mathrm{N}}{\mathrm{m}}$	$K^{DIFF} = 10^{11}\ \frac{\mathrm{m}^6}{\mathrm{kg}\cdot\mathrm{s}^2}$
$\lambda_0 = 1.11 \cdot 10^{10}\frac{\mathrm{N}}{\mathrm{m}}$	$\gamma_w = 10\ \frac{\mathrm{kN}}{\mathrm{m}^3}$
$\mu_0 = 1.67 \cdot 10^{10}\frac{\mathrm{N}}{\mathrm{m}}$	$\gamma_c = 25\ \frac{\mathrm{kN}}{\mathrm{m}^3}$
$\nu = 0.2$	$n = 0$

Table 3.1: Parameters for numerical investigation

Analyzes are conducted by carring out a damage check. In particular, the analysis is over when in a certain percentage (in the numerical examples 1%) of the total area the damage ω reaches its maximum value, 1.

3.5.1 Rectangular case

The domain is splitted in two subdomain in order to use two different sizes of the mesh and reducing the computational time. We expected a finer mesh is needed in the area of the domain where higher are the phenomena of the diffusion, i.e. the subdomain at the left hand side of the body. In particular:

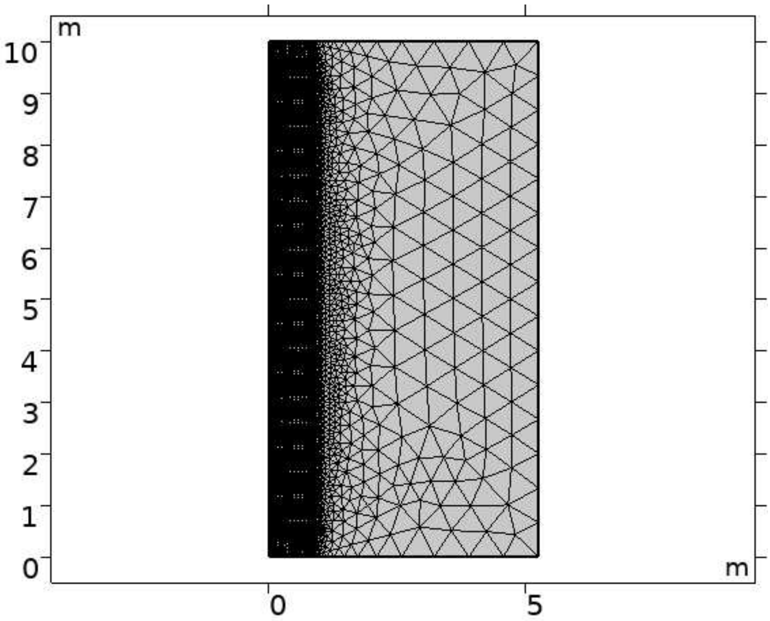

Figure 3.2: Different sizes of the mesh that allowed to investigate with higher accuracy the area where the evolution of the concentration c and the damage ω is strongly present. The domain is discretized into elements with side lengths of up to 67 cm, while the subdomain on the left is further refined with elements having maximum side lengths of 5 cm.

Initially, the displacements are only affected by the pressure of the water, as it is shown in the Fig 3.3-a and 3.4-a. They increase, like a cantilever model, when the stiffnesses decrease, because the material becames softer in the region where the damage is concentrated (see Fig. 3.3-b and 3.4-b). When the damage parameter ω attains the value of 1 in a specific region, the material in that region is considered completely failed and no longer contributes to the load-bearing capacity. Consequently, the effective cross-section of body $\mathcal{B}$ is reduced. In this numerical example, a constraint is placed on the extent of damage. The maximum allowable damaged area is set to 1% of the total area. This constraint on damaged area is the reason why the final displacements are slightly higher than the initial ones.

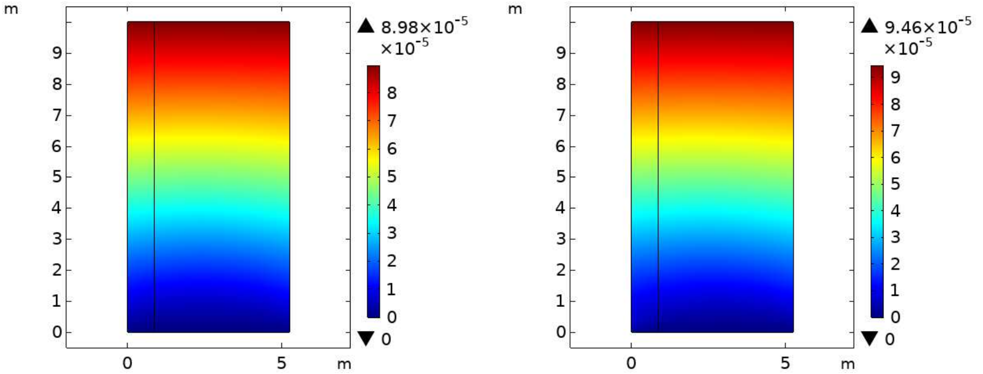

(a) (b)

Figure 3.3: Horizontal displacement u_1 at the (a) initial time and (b) final time $t \approx 85$years

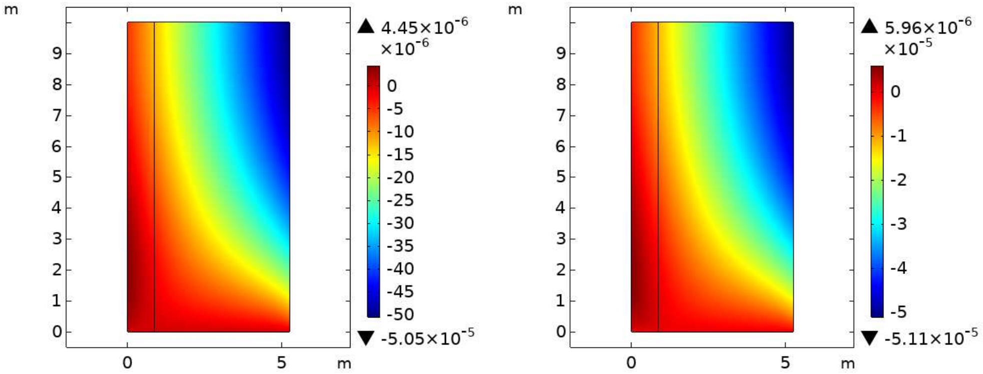

(a) (b)

Figure 3.4: Vertical displacement u_2 at the (a) initial time and (b) final time $t \approx 85$years

It is worth to notice that, as in [188] the concentration c and the damage ω evolve in a similar way. This behaviour is clear thinking how, by means the coupling term $K_{c\omega}$, the two descriptors are linked each other.

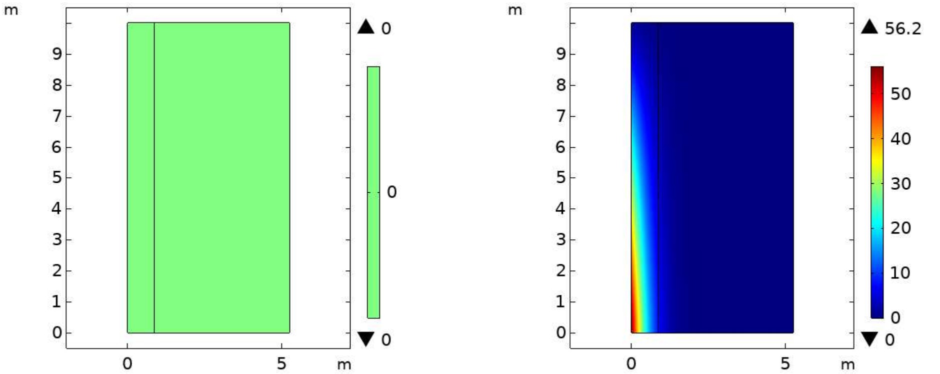

(a) (b)

Figure 3.5: Concentration c at the (a) initial time and (b) final time $t \approx 85$years

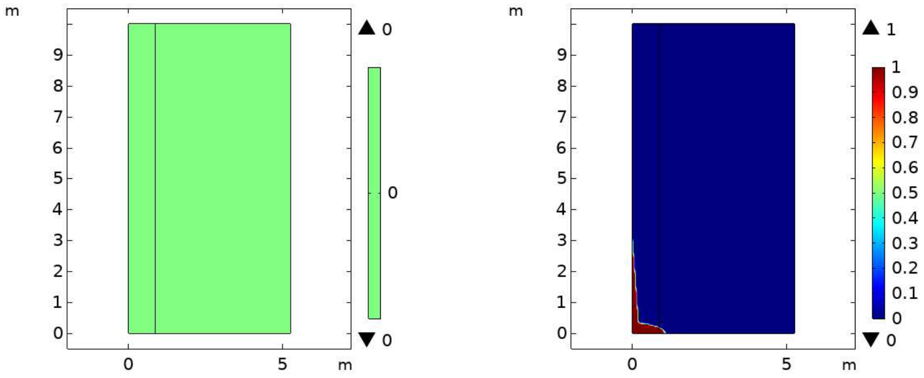

(a) (b)

Figure 3.6: Damage ω at the (a) initial time and (b) final time $t \approx 85$years

To clarify the distribution of concentration c and damage ω across the cross-section, the evolution of these descriptors at a section with coordinate $X_2 = 0.2$ (the red line in Fig. 3.7) m is shown in Fig. 3.7.

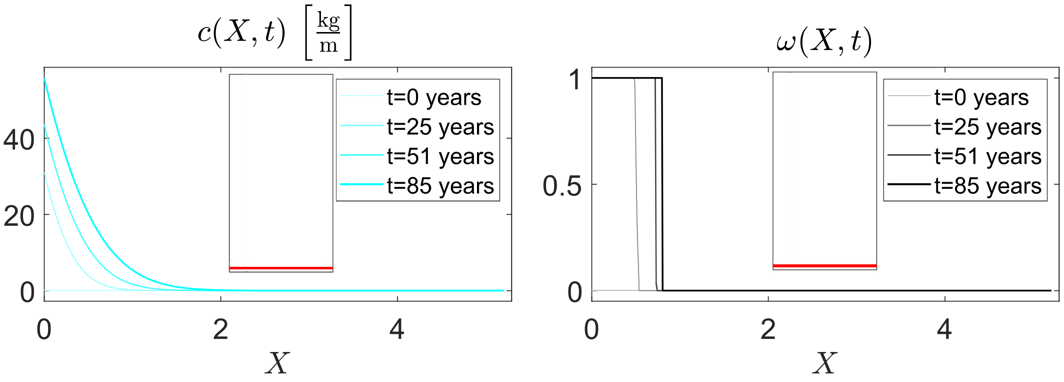

(a) (b)

Figure 3.7: Concentration (a) and damage (b) on the section line with $X_2 = 0.2$m for each instant of time

Several analyses for different values of K^{DIF}, $K_{c\omega}$ are done in Sec.s 3.5.1.1 and 3.5.1.2 to clarify the role of the diffussivity parameter.

3.5.1.1 Parametric analysis: K^{DIFF}

As it is shown in the following, the diffussivity term K^{DIF} give us a measure of the permeability of the body. The concentration c and the damage ω are shown for various values of the diffusivity term K^{DIF}. A parametric analysis was conducted by examining both higher and lower values of K^{DIF} than that reported in Table 3.1 (Section 3.5.1) to investigate its influence. Fig.s 3.8 and 3.9 show that when permeability is lower, the body's lifetime increases because the fluid cannot spread easily into the material. Consequently, the fluid needs more time to attain a concentration sufficient to initiate the damage ω.

- For $K^{DIF} = 5 \cdot 10^8 \frac{\mathrm{m}^6}{\mathrm{kg} \cdot \mathrm{s}}$ the analysis is conclused for $t \approx 63$years

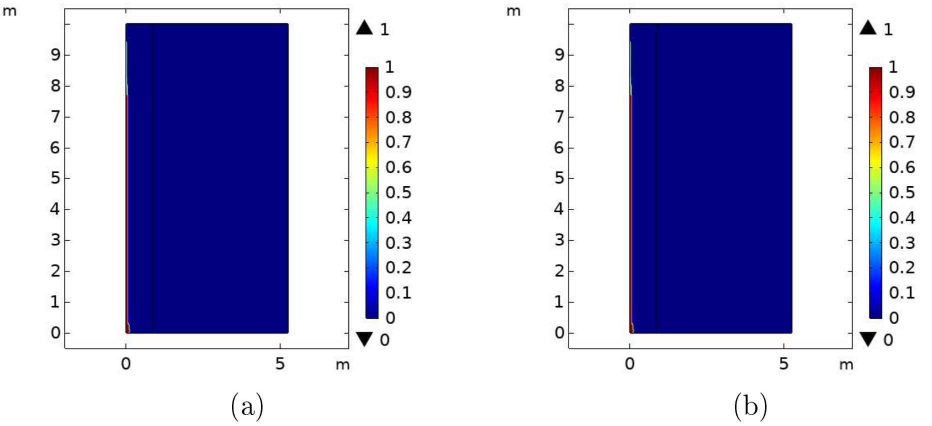

(a) (b)

Figure 3.8: (a) Concentration c and (b) damage ω for $K^{DIFF} = 5 \cdot 10^8 \frac{\mathrm{m}^6}{\mathrm{kg} \cdot \mathrm{s}}$

- For $K^{DIF} = 10^{10} \frac{\mathrm{m}^6}{\mathrm{kg} \cdot \mathrm{s}}$ the analysis is conclused for $t \approx 38$years

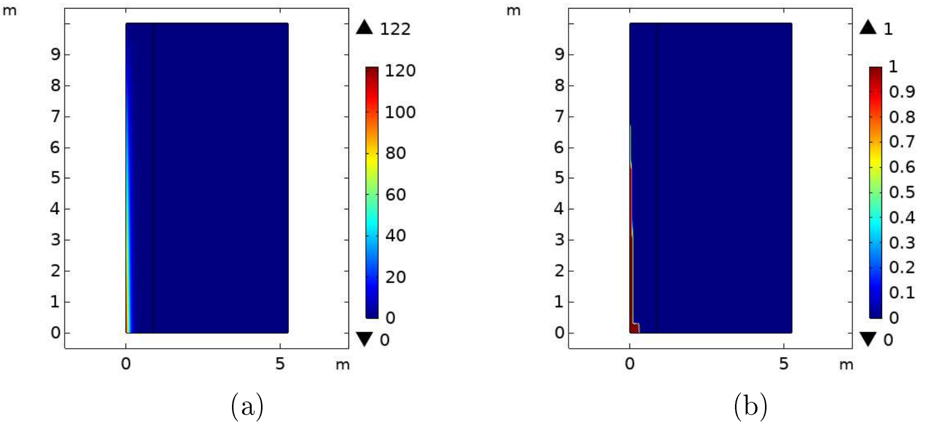

(a) (b)

Figure 3.9: (a) Concentration c and (b) damage ω for $K^{DIFF} = 10^{10} \frac{\mathrm{m}^6}{\mathrm{kg} \cdot \mathrm{s}}$

The decreasing trend in lifetime is no longer observed for higher values of K^{DIF}. Instead, after reaching a minimum value (as it will be shown in Fig. 3.31 the trend reverses, and lifetime becomes an increasing function of K^{DIF}. This phenomenon can be readily explained by considering that higher permeability leads to a more widespread distribution of the fluid, thereby reducing the local value of c and its rate within the body. The lower diffusion rate of the fluid, in turn, corresponds to a slower damage growth rate reducing the evolution in time of the damage ω.

- For $K^{DIF} = 10^{11} \frac{\mathrm{m}^6}{\mathrm{kg} \cdot \mathrm{s}}$ the analysis is conclused for $t \approx 85$years

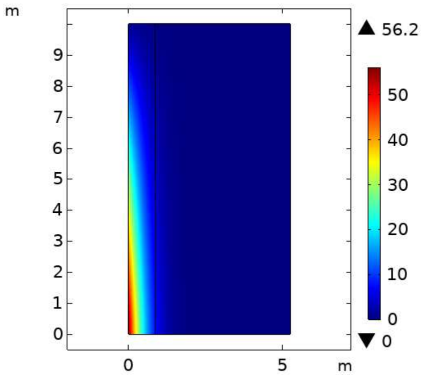

(a) (b)

Figure 3.10: (a) Concentration c and (b) damage ω for $K^{DIF} = 10^{11}\frac{\mathrm{m}^6}{\mathrm{kg{\cdot}s}}$

- For $K^{DIF} = 2 \cdot 10^{11}\frac{\mathrm{m}^6}{\mathrm{kg{\cdot}s}}$ the analysis is conclused for $t \approx 143$years

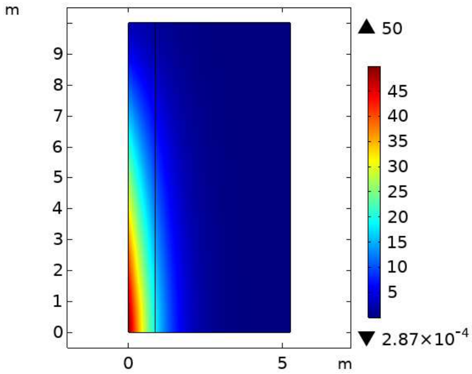

(a) (b)

Figure 3.11: (a) Concentration c and (b) damage ω for $K^{DIF} = 2 \cdot 10^{11}\frac{\mathrm{m}^6}{\mathrm{kg{\cdot}s}}$

- For $K^{DIF} = 3 \cdot 10^{11}\frac{\mathrm{m}^6}{\mathrm{kg{\cdot}s}}$ the analysis is conclused for $t \approx 204$years

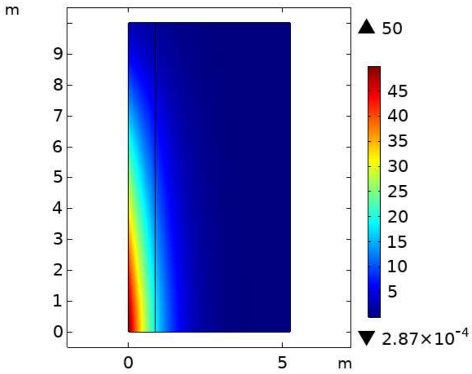

(a) (b)

Figure 3.12: (a) Concentration c and (b) damage ω for $K^{DIF} = 3 \cdot 10^{11}\frac{\mathrm{m}^6}{\mathrm{kg{\cdot}s}}$

The increased diffusivity value K^{DIF}, by influencing the fluid diffusion within the body, also affects the damage evolution. Fig.s 3.8, 3.9, 3.10, 3.11 and 3.12 show that as K^{DIF} increases, the damage ω concentrates at the base and "diffuses" horizontally, in contrast to the behavior observed for lower values of K^{DIF}, where the fluid is hindered from easily propagating within the body $\mathcal{B}$ and is concentrated near the interface boundary in contact with the fluid (left side).

3.5.1.2 Parametric analysis: $K_{c\omega}$

One more parametric analysis is conducted with respect to the concentration-damage coupling term $K_{c\omega}$. This term links the fluid concentration within the body $\mathcal{B}$ to the damage of the body itself. The increasing in modulus of the diffusivity (remember that $K_{c\omega} < 0$ as in (3.39)) reducing the threshold $K_{\omega 0}$ and thereby activating damage under the same external loads. The analysis was carried out by systematically varying the value of parameter $K_{c\omega}$, while keeping all other parameters fixed at the values given in Tab. 3.1. Concentration c and the damage ω for different values of $K_{c\omega}$ are shown. In particular $K_{c\omega} = -1.1\frac{\mathrm{m}^2}{\mathrm{s}^2}$ (Fig. 3.13), $K_{c\omega} = -1\frac{\mathrm{m}^2}{\mathrm{s}^2}$ (Fig.3.14) and $K_{c\omega} = -0.9\frac{\mathrm{m}^2}{\mathrm{s}^2}$ (Fig.3.15). One can see how the life of the body $\mathcal{B}$ increases for lower value (in modulus) of the coupling parameter $K_{c\omega}$.

- For $K_{c\omega} = -1.1\frac{\mathrm{m}^2}{\mathrm{s}^2}$ the analysis is stopped for $t \approx 73$years

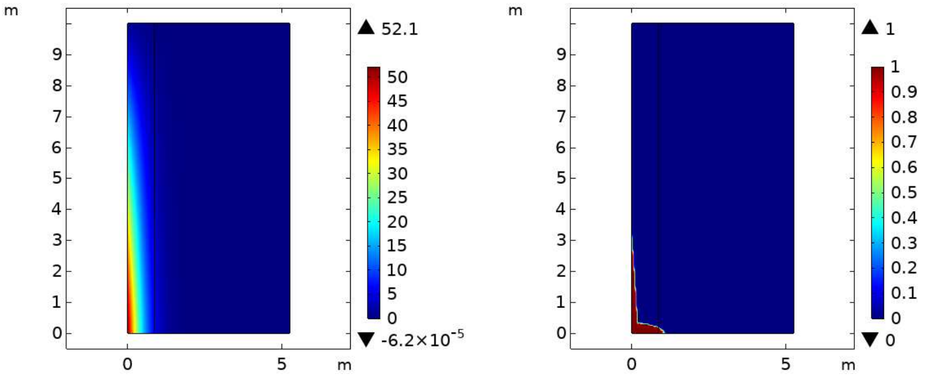

(a)

(b)

Figure 3.13: (a) Concentration c and (b) damage ω for $K_{c\omega} = -1.1\frac{\mathrm{m}^2}{\mathrm{s}^2}$

- For $K_{c\omega} = -1\frac{\mathrm{m}^2}{\mathrm{s}^2}$ the analysis is stopped for $t \approx 85$years

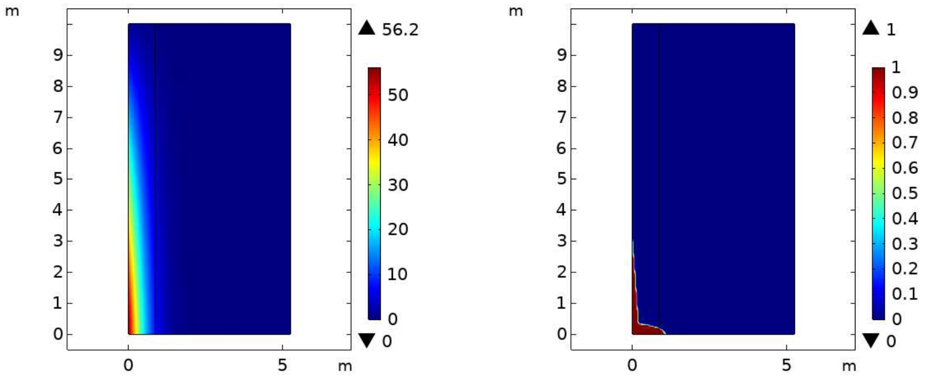

(a) (b)

Figure 3.14: (a) Concentration c and (b) damage ω for $K^{DIFF} = -1\frac{\mathrm{m}^2}{\mathrm{s}^2}$

- For $K_{c\omega} = -0.9\frac{\mathrm{m}^2}{\mathrm{s}^2}$ the analysis is stopped for $t \approx 102$years

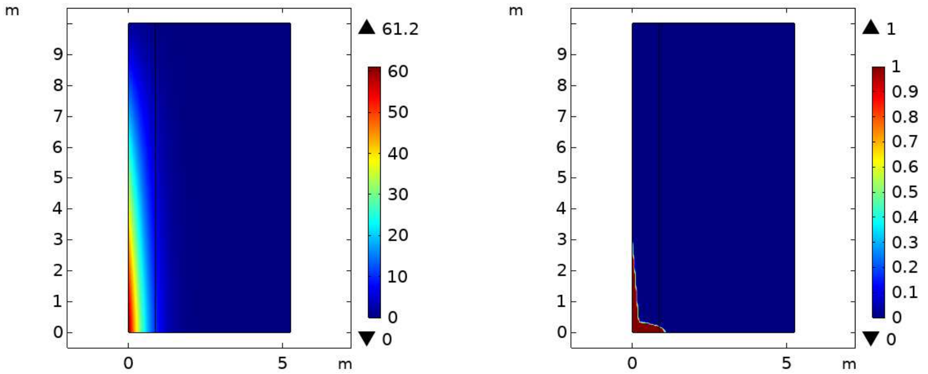

(a) (b)

Figure 3.15: (a) Concentration c and (b) damage ω for $K_{c\omega} = -0.9\frac{\mathrm{m}^2}{\mathrm{s}^2}$

The damage parameter ω is strongly influenced by the coupling term $K_{c\omega}$. As clearly shown in Figs. 3.13, 3.14 and 3.15, even small variations in $K_{c\omega}$ (on the order of 10^{-1}) lead to significant changes in the lifetime. This parameter warrants further investigation for future developments, as it can be influenced by the chemical composition of the body $\mathcal{B}$, the damaging fluid, and, of course, their interaction.

3.5.2 Dam's case

In this section a real dam's case is shown. Also for this case we chose to split the domain to optimize the sizes of the mesh and in the Fig. 3.16 the model is shown, one more time the area in which the mesh must be finer is that one near the upstream boundary (on the left-hand side):

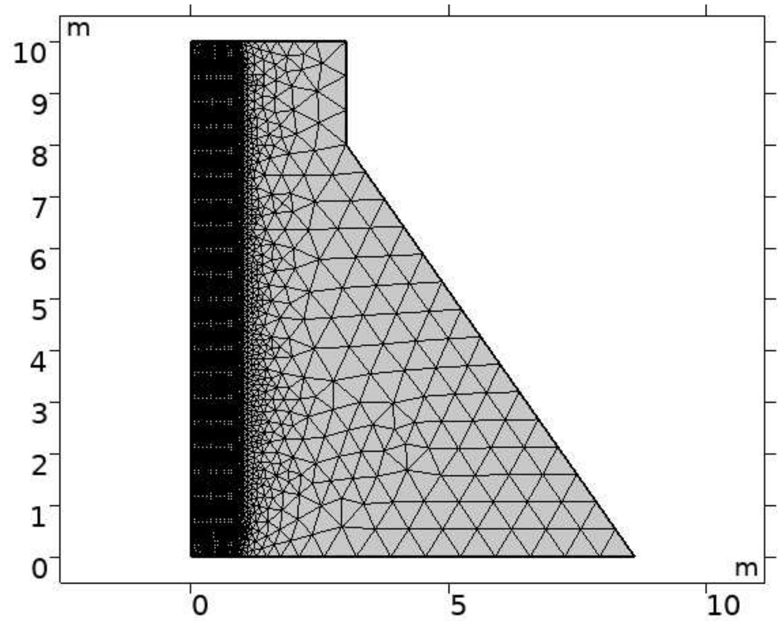

Figure 3.16: Different sizes of the mesh that allowed to investigate with higher accurasy the areas where the evolution of the concentration c and the damage ω is present

From the [220] the investigated shape has the follow characteristics: the upstream face is vertical instead the downstream face has usually a uniform slope transitioning to a vertical face near the crest. The ratio of the slope is usually in the range of 0.7H (Horizontal) to 1V (Vertical), to 0.8H to 1V. In the next example a crest having a width of 3m (for allowing the transit of vehicles) and a height of 2m. The parameters, as shown in Tab. 3.1,remain unchanged from the rectangular case discussed in Sec. 3.5.1. In contrast to the rectangular counterpart, the proposed shape demonstrates enhanced resistance to external loads through an improved contribution of its own weight to stability. Also for this case, under compressive stress conditions the body $\mathcal{B}$ responds with a remarkably high damage threshold (see Eq.(3.2)), confining damage ω to the interface and preserving its resistant cross-section almost entirely. This significantly reduces the body's displacements. Damage in the vicinity of the lower left corner relaxes the stress state, causing the structure to reduce bending and, consequently, slightly diminish the horizontal displacement at the top. Fig. 3.17 illustrates the plot of displacement u_1 in the deformed configuration. Only the horizontal displacement deformation is emphasized (a multiplication factor of 150000 was applied to enhance visibility). Instead the vertical displacements increase due to stiffness reduction caused by the presence of damage (see Fig. 3.18).

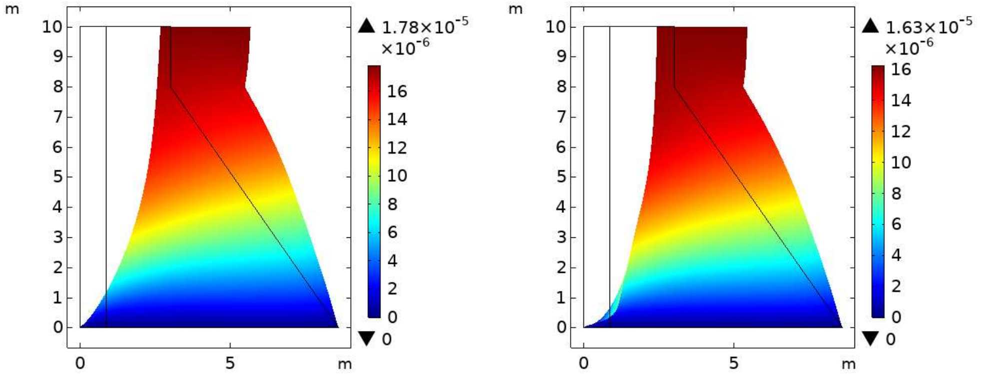

(a) (b)

Figure 3.17: Horizontal displacement u_1 at the (a) initial time and (b) final time $t \approx 101$years

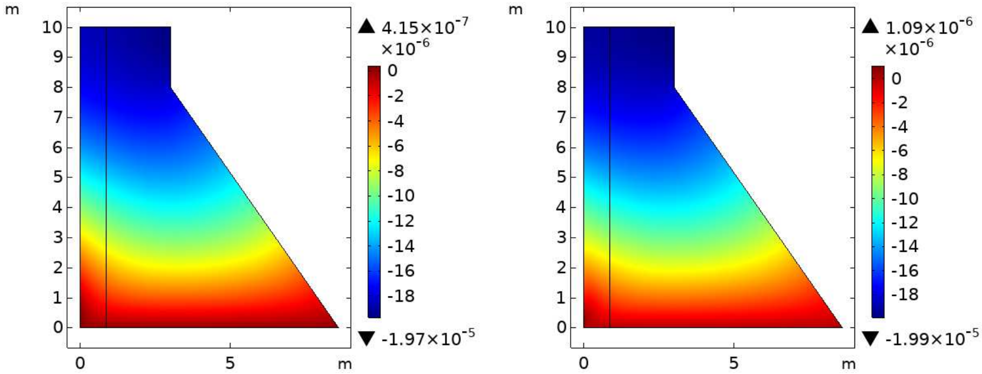

(a) (b)

Figure 3.18: Vertical displacement u_2 at the (a) initial time and (b) final time $t \approx 101$years

As for the rectangular case, concentration c and damage ω evolve in a similar way but, in this case, the damage need longer time to "spread" through the section because, as remarked before, the compressive stress state is associated with a higher damage threshold $K_{\omega 0}$, enabling the body to better resist the onset of damage. This is why its lifetime is significantly longer compared to the rectangular case.

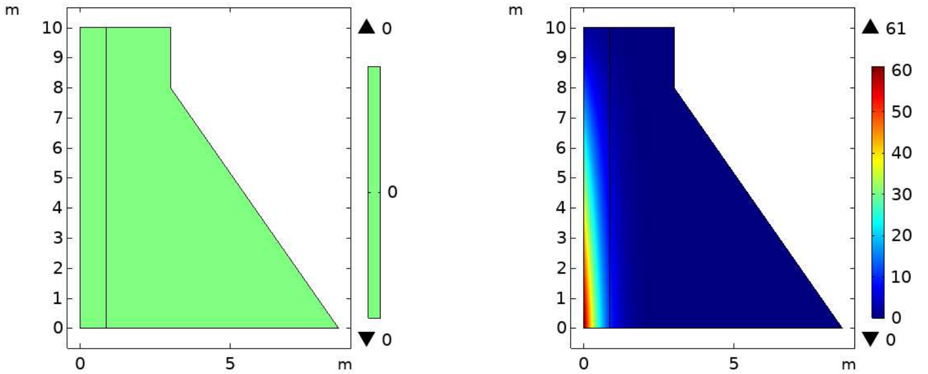

(a) (b)

Figure 3.19: Concentration c at the (a) initial time and (b) final time $t \approx 101$years

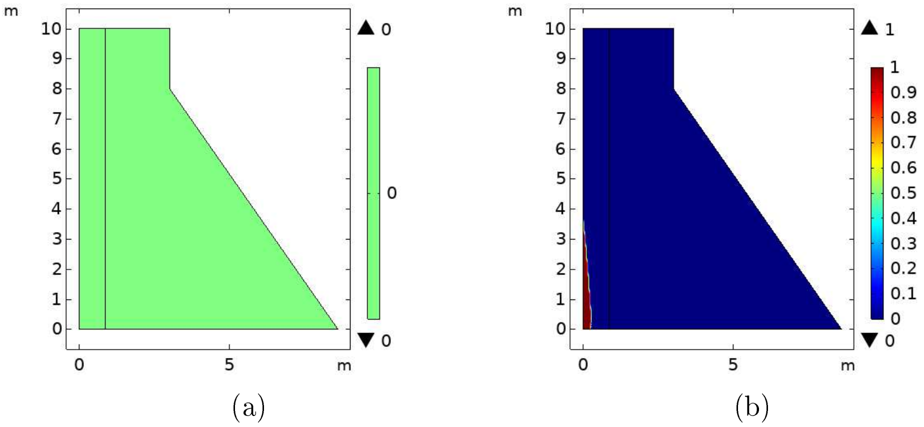

(a) (b)

Figure 3.20: Damage ω at the (a) initial time and (b) final time $t \approx 101$years

The evolution of the concentration c and the damage ω for a section with coordinates $X_2 = 0.2$m are shown in the Fig. 3.21

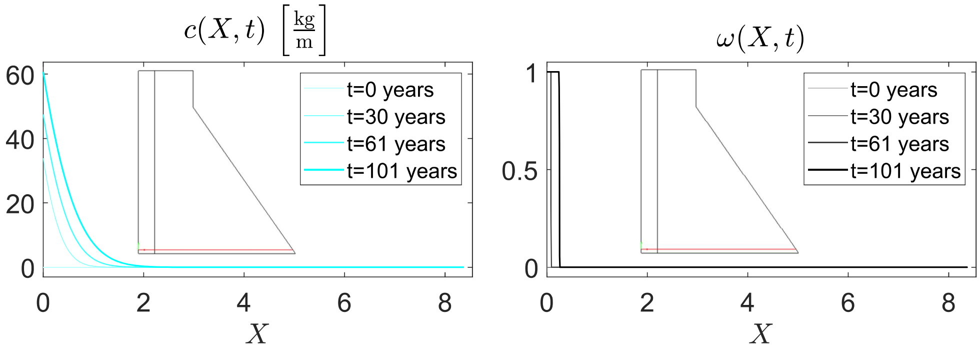

(a) Concentration c (b) Damage ω

Figure 3.21: Concentration c and Damage ω at the section having coordinate $X_2 = 0.2m$

3.5.2.1 Parametric analysis: K^{DIFF}

Also for this case, as for the rectangular one, the concentration c and the damage ω for different values of the diffusivity term K^{DIFF} are shown in the Fig. 3.22, 3.23, 3.24, 3.25 and 3.26. The parametric analysis is carried out adopting the same values of K^{DIFF} used in Sec. 3.5.1.1, id est:

- For $K^{DIFF} = 5 \cdot 10^8 \frac{\mathrm{m}^6}{\mathrm{kg} \cdot \mathrm{s}}$ the analysis is conclused for $t \approx 65$years

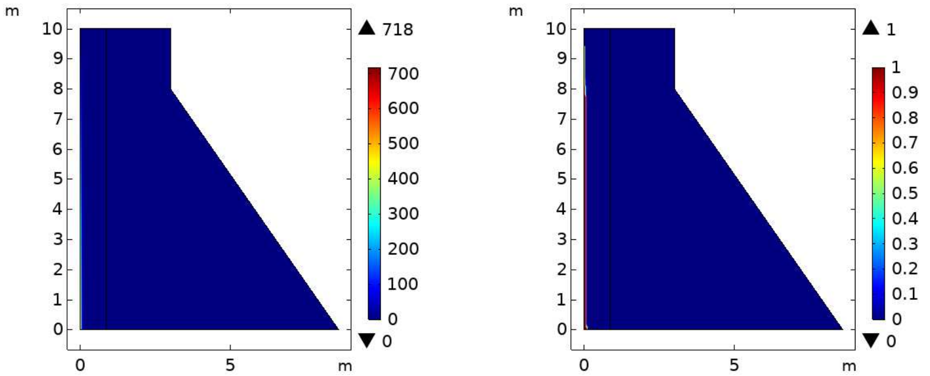

(a) (b)

Figure 3.22: (a) Concentration c and (b) damage ω for $K^{DIFF} = 5 \cdot 10^8 \frac{\text{m}^6}{\text{kg}\cdot\text{s}}$

- For $K^{DIFF} = 10^{10} \frac{\text{m}^6}{\text{kg}\cdot\text{s}}$ the analysis is conclused for $t \approx 41$years

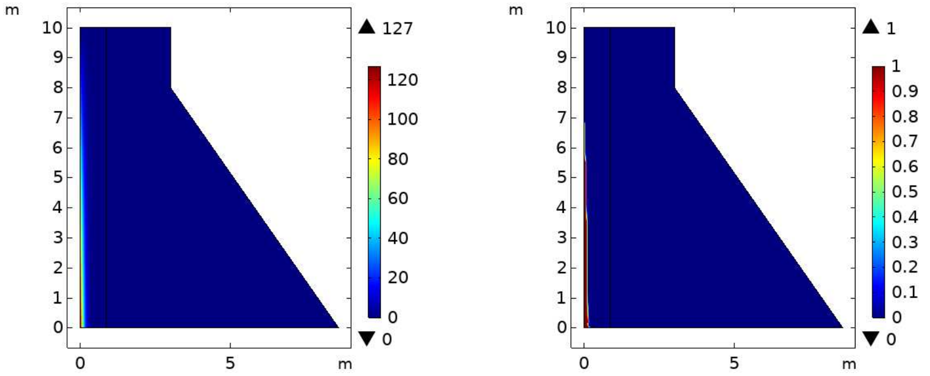

(a) (b)

Figure 3.23: (a) Concentration c and (b) damage ω for $K^{DIFF} = 10^{10} \frac{\text{m}^6}{\text{kg}\cdot\text{s}}$

- For $K^{DIFF} = 10^{11} \frac{\text{m}^6}{\text{kg}\cdot\text{s}}$ the analysis is conclused for $t \approx 101$years

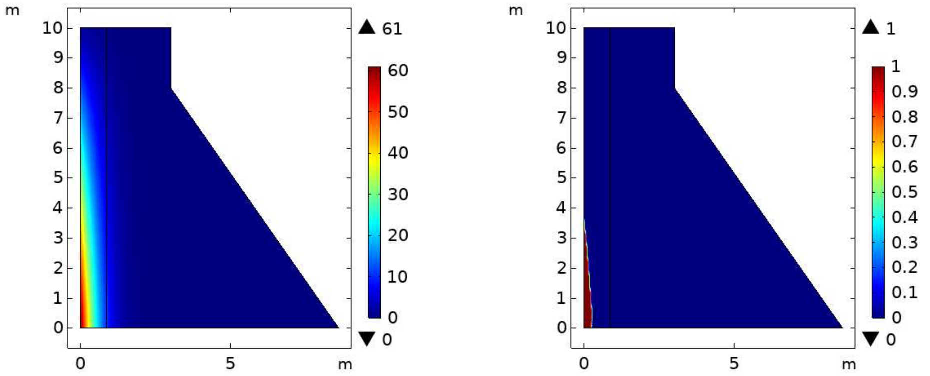

(a) (b)

Figure 3.24: (a) Concentration c and (b) damage ω for $K^{DIFF} = 10^{11} \frac{\text{m}^6}{\text{kg}\cdot\text{s}}$

- For $K^{DIFF} = 2 \cdot 10^{11} \frac{\mathrm{m}^6}{\mathrm{kg} \cdot \mathrm{s}}$ the analysis is conclused for $t \approx 161$years

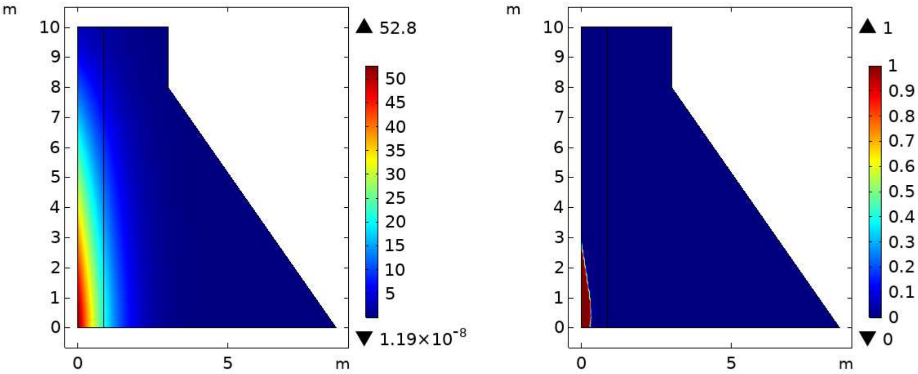

(a) (b)

Figure 3.25: (a) Concentration c and (b) damage ω for $K^{DIFF} = 2 \cdot 10^{11} \frac{\mathrm{m}^6}{\mathrm{kg} \cdot \mathrm{s}}$

- For $K^{DIFF} = 3 \cdot 10^{11} \frac{\mathrm{m}^6}{\mathrm{kg} \cdot \mathrm{s}}$ the analysis is conclused for $t \approx 233$years

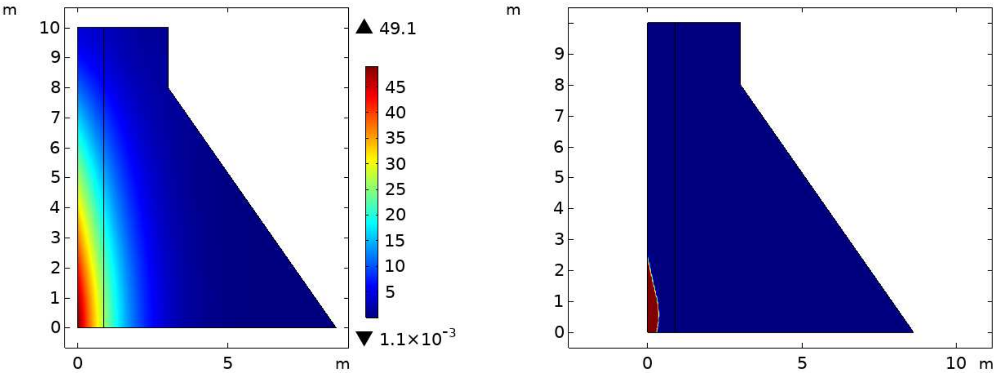

(a) (b)

Figure 3.26: (a) Concentration c and (b) damage ω for $K^{DIFF} = 3 \cdot 10^{11} \frac{\mathrm{m}^6}{\mathrm{kg} \cdot \mathrm{s}}$

From the figures 3.22, 3.23, 3.24, 3.25 and 3.26 one notes that when the diffusivity K^{DIF} increases not always the life time of the structures increases. The motivation is the same we explained for the rectangular case in the Sec. 3.5.1.1. In other words, when diffusivity is high, the fluid can spread across a larger area of body $\mathcal{B}$, resulting in lower values and rates. This slows down the damage diffusion process. Conversely, when diffusivity is low, the impermeability restricts the fluid's ability to permeate the structure. Consequently, the damaged area reaches a limit that cannot be exceeded if K^{DIF} is much smaller. As observed in the rectangular case (Sec. 3.5.1.1), when the diffusivity increases a "migration" of the damaged zone from the structure-fluid interface towards the base continues to be evident.

3.5.2.2 Parametric analysis: $K_{c\omega}$

As for the rectangular case shown in Sec. 3.5.1.2, the parametric analysis in terms of $K_{c\omega}$ is here presented. In the following the concentration c and the damage ω for different values of $K_{c\omega}$ (one higher and one smaller than the main example shown in Sec. 3.5.2) are presented. Also for this case the aforementioned analysis aims to elucidate the role of $K_{c\omega}$ and quantify the extent to which this parameter influences the evolution of damage. The different values of $K_{c\omega}$ are the same of the rectangular case to allow to make a comparison. So

$$K_{c\omega} = \left\{-1.1 \cdot 10^6, -1 \cdot 10^6, -0.9 \cdot 10^6\right\} \frac{\mathrm{m}^2}{\mathrm{s}^2}$$

- For $K_{c\omega} = -1.1\frac{\mathrm{m}^2}{\mathrm{s}^2}$ the analysis is stopped for $t \approx 87$years

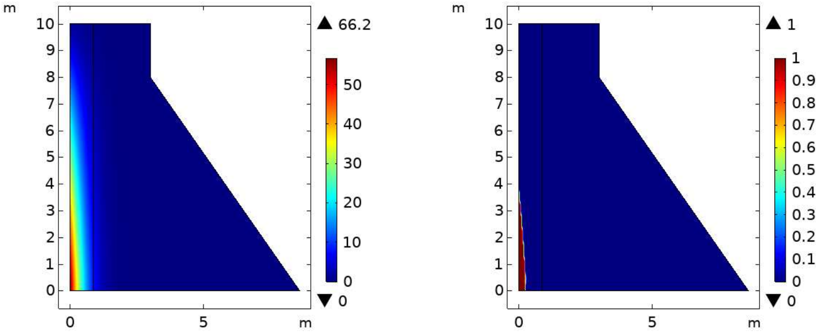

(a) (b)

Figure 3.27: (a) Concentration c and (b) damage ω for $K_{c\omega} = -1.1\frac{\mathrm{m}^2}{\mathrm{s}^2}$

- For $K_{c\omega} = -1\frac{\mathrm{m}^2}{\mathrm{s}^2}$ the analysis is stopped for $t \approx 101$years

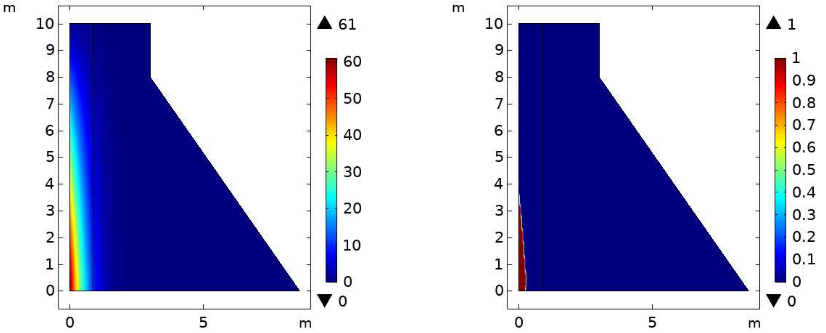

(a) (b)

Figure 3.28: (a) Concentration c and (b) damage ω for $K^{DIFF} = -1\frac{\mathrm{m}^2}{\mathrm{s}^2}$

- For $K_{c\omega} = -0.9\frac{\mathrm{m}^2}{\mathrm{s}^2}$ the analysis is stopped for $t \approx 120$years

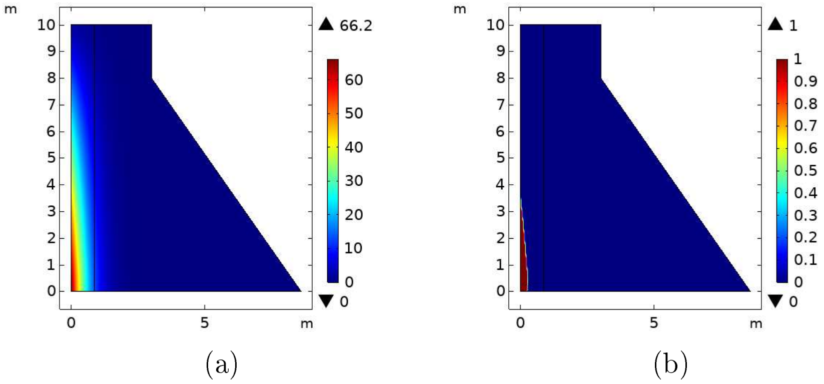

(a) (b)

Figure 3.29: (a) Concentration c and (b) damage ω for $K_{c\omega} = -0.9\frac{\mathrm{m}^2}{\mathrm{s}^2}$

3.5.3 Comparison

Some comparisons are reported here between the two cases analyzed above (rectangular case and dam case) which show how the stockier shape continues to have a better mechanical response. The comparison are carried out in terms of lifetime of the dam. In Fig. 3.30 the evolution of the damaged area in time of the body $\mathcal{B}$ is shown for both the rectangular and the dam cases. As can be easily observed, the rectangular case takes less time to reach 1% of damaged area (and the difference between the two cases is around 15%)

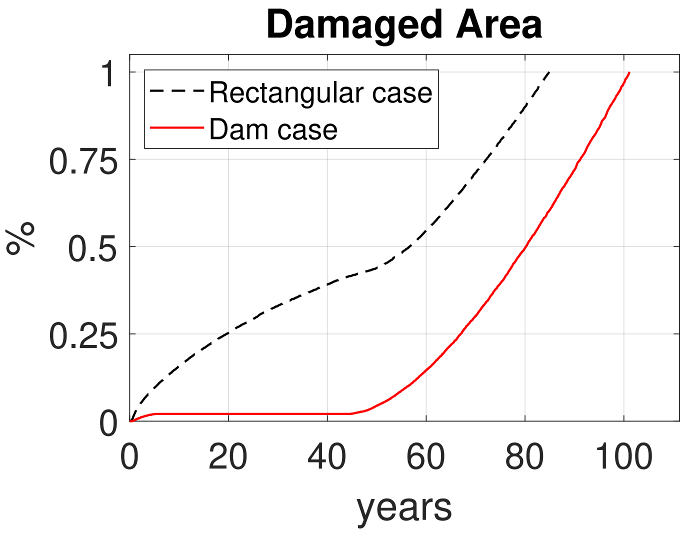

Figure 3.30: Evolution of the damaged area in time

The evolution of the lifetime shown in Sec. 3.5.1 (Fig. 3.8, 3.9, 3.10, 3.11 and 3.12) and in Sec. 3.5.2 (Fig. 3.22, 3.23, 3.24, 3.25 and 3.26) is plotted at Fig. 3.31. One can be observed that the lifetime of body B exhibits a decreasing trend for lower diffusivity values K^{DIF} and, after reaching a minimum value, starts to increase again. This behavior is highly realistic because for lower diffusivity values K^{DIF}, the fluid remains confined to the interface and, unable to diffuse easily, the concentration c reaches remarkably high values in a relatively confined area. Consequently, through the coupling parameter $K_{c\omega}$, the damage ω also spreads slowly, leading to a very slow attainment of the imposed limit (1% of the total area). Conversely, when the diffusivity increases beyond a certain range, the fluid penetrates and diffuses more easily into the body, causing the same amount of fluid to distribute over a larger region, thus reducing the concentration rate in the affected area. This lower growth rate of c clearly corresponds to a lower growth rate of the damage ω. Bigger differences are observable for the extreme values of K^{DIF} (see Fig. 3.31 and Fig. 3.32).

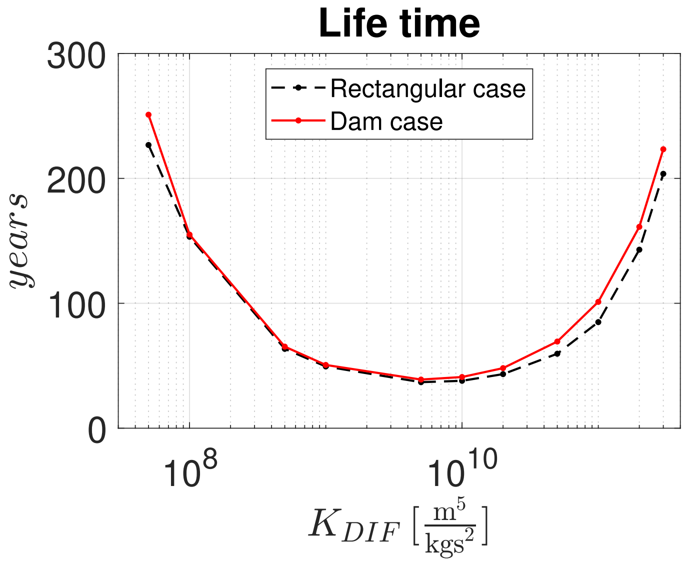

Figure 3.31: Lifetime of the body $\mathcal{B}$ as K^{DIF} varies

Denoting, for each value of diffusivity K^{DIF}, the lifetime of the dam case as t_d and the lifetime of the rectangular case as t_r, the percentage difference is calculated as follows:

$$100\frac{t_d - t_r}{t_r} \tag{3.43}$$

one can see in Fig. 3.32 that the differences in lifetime are negligible within the range of K^{DIF} between $10^8 \frac{\mathrm{m}^6}{\mathrm{kg\cdot s}}$ and $10^9 \frac{\mathrm{m}^6}{\mathrm{kg\cdot s}}$. However, these differences becomes more pronounced for both lower and higher values of K^{DIF}, as already depicted in the Sec. 3.5.1.1 and Sec. 3.5.2.1.

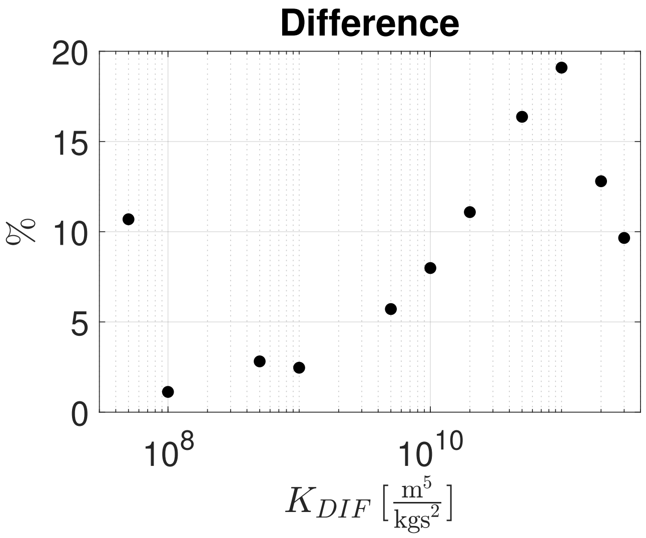

Figure 3.32: Lifetime of the body $\mathcal{B}$ as K^{DIF} varies

In the Fig. 3.33 and 3.34 the plot of the evolution of the eigenvalues and trace of the strain tensor $\mathbb{G}$ is shown in order to analyze the stress state of the body as the shape changes. The colormap for the eigenvalue plots is scaled to a maximum of 0, thus enhancing the visibility of regions of compressive stress, as indicated by negative eigenvalues. Notably, for the dam case, unlike the rectangular case, the trace is negative throughout the entire domain, signifying overall compressive behavior. Thus giustifying the shape largely used to design the gravity dams.

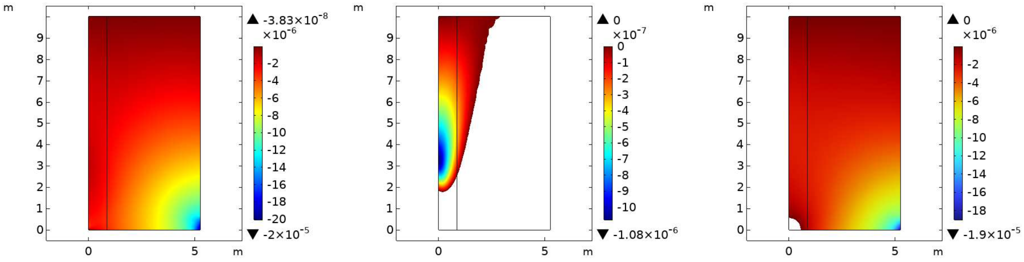

(a) Lowest eigenvalue of $\mathbb{G}$ at $t = 0$ years (b) Highest eigenvalue of $\mathbb{G}$ at $t = 0$ years (c) Trace of $\mathbb{G}$ at $t = 0$ years

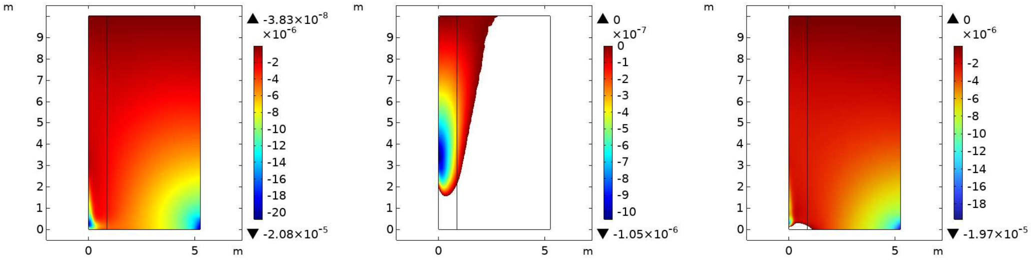

(d) Lowest eigenvalue of $\mathbb{G}$ at $t \approx 85$ years (e) Highest eigenvalue of $\mathbb{G}$ at $t \approx 85$ years (f) Trace of $\mathbb{G}$ at $t \approx 85$ years

Figure 3.33: Eigenvalues and trace of $\mathbb{G}$ at the initial and final time

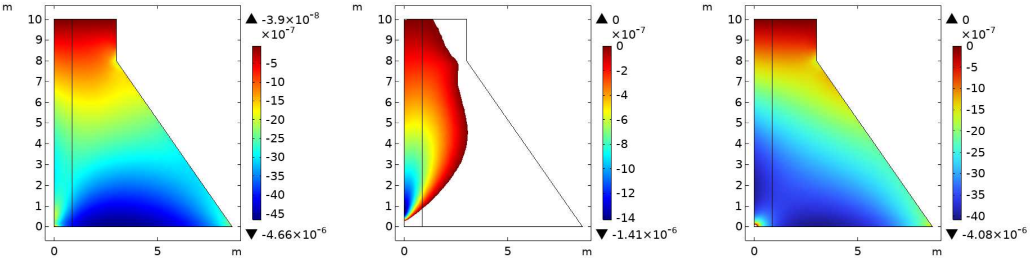

(a) Lowest eigenvalue of $\mathbb{G}$ at $t = 0$ years (b) Highest eigenvalue of $\mathbb{G}$ at $t = 0$ years (c) Trace of $\mathbb{G}$ at $t = 0$ years

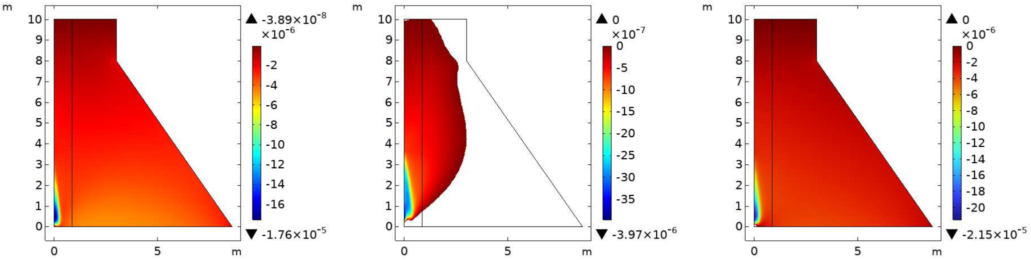

(d) Lowest eigenvalue of $\mathbb{G}$ at $t \approx 101$ years (e) Highest eigenvalue of $\mathbb{G}$ at $t \approx 101$ years (f) Trace of $\mathbb{G}$ at $t \approx 101$ years

Figure 3.34: Eigenvalues and trace of $\mathbb{G}$ at the initial and final time

Comparing Fig.s 3.33-c and 3.33-f with Fig.s 3.34-c and 3.34-f, a substantial difference in terms of the extent of the area subjected to tension is observed. In the rectangular case, a significant portion of the domain, particularly at the base, is found to be in tension ($tr\mathbb{G} > 0$). The dam case exhibits a markedly different response: Fig.s 3.34-c and 3.34-f reveal only a negligible region near the bottom-left corner with spurious positive values, likely attributable to numerical round-off errors.

Chapter 4

Miscellaneous

This dissertation presents a novel numerical model for simulating a creep behaviour and a non-linear approach to study the seismic event (with a particular focus on the 2009 L'Aquila earthquake).

Creep, traditionally associated with time-dependent deformation of materials under constant stress, is a phenomenon characterized by a time-dependent reduction in stiffness under constant load, here called *apparent* because in this simulation the deformations (that are elastic) are consequence of the reduction in stiffness is attributed to fluid-induced degradation, extending it to a more general framework that accounts for the influence of fluid-body interactions that produce degradation on the domain. While the classical view of creep is rooted in material properties, the concept of apparent creep emphasizes the role of external factors, such as fluid pressure or chemical reactions, in inducing time-dependent deformation.

The L'Aquila earthquake provides a compelling case study for exploring the implications of non-linear behaviour in seismic analysis. The region's complex geological structure, characterized by significant stratigraphic heterogeneity, highlights the limitations of linear models in capturing the full spectrum of seismic response. Our findings reveal that the neglect of non-linear effects, particularly in regions with pronounced stratigraphic variations, can lead to substantial errors in the estimation of seismic energy and peak ground accelerations. These results underscore the importance of developing more sophisticated numerical models that can capture the complex interplay between geological heterogeneity and seismic loading.

4.1 Creep phenomenon

Creep is a phenomenon of critical importance in various engineering disciplines. In aeronautical engineering, where gas turbines operate under extreme temperatures, creep is a primary consideration in the design of turbine blades and other components. In nuclear engineering, the exceptionally high operating temperatures within reactors render creep a significant challenge for ensuring the safety and structural integrity of reactor components. In civil engineering, bridges, buildings, and other structures are susceptible to creep over time due to the sustained loads imposed by their own weight and other permanent forces. Creep is a slow and inescapable deformation. In engineering, the term creep describes a permanent deformation phenomenon that occurs in materials subjected to constant loads over long periods of time, generally at high temperatures. It's as if the material slowly yields under prolonged stress, deforming gradually and inexorably. This phenomenon should not be confused with elastic deformation, which is temporary and disappears when the load is removed. Creep, on the other hand, is a plastic deformation, or permanent, that remains imprinted on the material even after the load ceases. To fully comprehend creep, it is essential to examine the underlying physical mechanisms. Several factors collectively influence the creep rate. Temperature plays a pivotal role, as elevated temperatures energize atomic vibrations, weakening atomic bonds and facilitating dislocation motion, a process that underpins plastic deformation. Typically, creep becomes pronounced at temperatures exceeding approximately half the material's melting point. Concurrently, the magnitude of applied stress significantly impacts the creep rate, with a critical stress level below which creep is imperceptible. Moreover, the temporal aspect is crucial, as creep is a time-dependent process where deformation accumulates progressively under sustained load. Finally, the material's microstructure, characterized by grain size, porosity, and inclusions, profoundly affects creep resistance. A refined microstructure, with smaller grains and precipitates, generally exhibits enhanced creep resistance compared to coarser-grained materials. The creep process, easily recognizable in the Fig. 4.1 (from [106]), can be divided into three stages:

- Primary creep: in this initial stage, the creep rate decreases over time due to the hardening of the material caused by the rearrangement of dislocations.
- Secondary creep: in this stage, the creep rate becomes constant and the material deforms at a nearly uniform rate. This phase is of greatest engineering interest as it represents the long-term behaviour of the material.
- Tertiary creep: in this final stage, the creep rate increases rapidly due to grain breakage and cavity formation within the material, leading to structural failure.

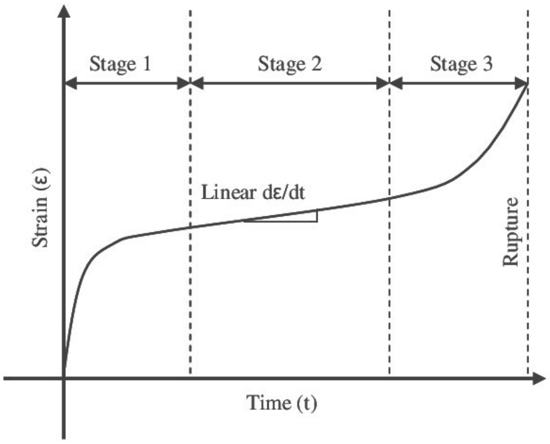

Figure 4.1: Generic creep behaviour: the three stages are clearly observable

4.1.1 Mathematical model

In order to describe the apparent creep phenomenon the same approach shown in the Sec. 3 is used. The mathematical model is the same shown in Sec. 3.1 and 3.2. So the total deformation energy is:

$$
\begin{aligned}
\mathcal{E} = & \int_{\mathcal{B}} \left[\left(\frac{\lambda}{2} + \mu \right) \left(G_{11}^2 + G_{22}^2 \right) + \lambda G_{11} G_{22} + 2\mu G_{12}^2 \right] dA \\
& + \int_{\mathcal{B}} \left[\left(G_{11,1}^2 + G_{22,2}^2 \right) \left(4\alpha_1 + \alpha_2 + 4\alpha_3 + 2\alpha_4 + 4\alpha_5 \right) \right] dA \\
& + \int_{\mathcal{B}} \left[\left(G_{11,1} G_{12,2} + G_{12,1} G_{22,2} \right) \left(4\alpha_1 + 8\alpha_3 \right) \right] dA \\
& + \int_{\mathcal{B}} \left[\left(G_{11,2} G_{12,1} + G_{12,2} G_{22,1} \right) \left(4\alpha_1 + 8\alpha_5 \right) \right] dA \\
& + \int_{\mathcal{B}} \left[\left(G_{11,2} G_{22,2} + G_{11,1} G_{22,1} \right) \left(4\alpha_1 + 2\alpha_2 \right) \right] dA \\
& + \int_{\mathcal{B}} \left[\left(G_{11,2}^2 + G_{22,1}^2 \right) \left(\alpha_2 + 2\alpha_4 \right) \right] dA \\
& + \int_{\mathcal{B}} \left[\left(G_{12,1}^2 + G_{12,2}^2 \right) \left(4\alpha_3 + 4\alpha_4 + 4\alpha_5 \right) \right] dA \\
& + \int_{\mathcal{B}} \left[\frac{1}{2} K^{DIF} \|\nabla c\|^2 + \frac{1}{2} K_F c^2 \right] dA \\
& + \int_{\mathcal{B}} \left[K_{\omega 0} \omega + K_{c\omega} c \omega + \frac{1}{2} K_{\omega} \omega^2 \right] dA \\
& - \int_{\partial \mathcal{B}} \left[f \left(\mathbf{u} \cdot \mathbf{n} \right) + b_c^{ext} c \right] ds
\end{aligned}
\tag{4.1}
$$

Where, as in Sec. 3.2, (i) K^{DIF} is the diffusivity parameter, (ii) K_F is the fluid elasticity of the body $\mathcal{B}$, (iii) $K_{\omega 0}$ represents the damage threshold, (iv) $K_{c\omega}$ is the concentration-damage coupling term, (v) K_{ω} is the resistance to the damage and (vi) b_c^{ext} is the external distributed aging influx pressure. Given its negligible density, the mass of the beam is not included in the analysis. From the hemivariational principle shown in Sect. 3.3, by means the Karush–Kuhn–Tucker conditions, the damage is obtained:

$$
\begin{aligned}
\tilde{\omega}\left(X,t\right) =& \frac{1}{K_{\omega}}\left\{\left(\frac{\lambda_0}{2}+\mu_0\right)\left(G_{11}^2+G_{22}^2\right)+\lambda_0 G_{11}G_{22}+2\mu_0 G_{12}^2\right. \\
& -n\left[\left(G_{11,1}^2+G_{22,2}^2\right)\left(4\alpha_1^0+\alpha_2^0+4\alpha_3^0+2\alpha_4^0+4\alpha_5^0\right)\right. \\
& +\left(G_{11,1}G_{12,2}+G_{12,1}G_{22,2}\right)\left(4\alpha_1^0+8\alpha_3^0\right) \\
& +\left(G_{11,2}G_{12,1}+G_{12,2}G_{22,1}\right)\left(4\alpha_1^0+8\alpha_5^0\right) \\
& +\left(G_{11,2}G_{22,2}+G_{11,1}G_{22,1}\right)\left(4\alpha_1^0+2\alpha_2^0\right) \\
& +\left(G_{11,2}^2+G_{22,1}^2\right)\left(\alpha_2^0+2\alpha_4^0\right) \\
& \left.\left.+\left(G_{12,1}^2+G_{12,2}^2\right)\left(4\alpha_3^0+4\alpha_4^0+4\alpha_5^0\right)\right]\right\} \\
& -\frac{1}{K_{\omega}}\left\{K_{\omega_0}+K_{c\omega}\cdot c\right\}
\end{aligned}
\tag{4.2}
$$

Clearly, remembering that

$$
\frac{\partial\omega}{\partial t}\geq 0 \qquad \forall\mathbf{X}\in\mathcal{B} \tag{4.3}
$$

in order to obtain the monolateral behaviour of ω, numerically, the following condition is imposed:

$$
\dot{\tilde{\omega}}<0\Longrightarrow\dot{\tilde{\omega}}=0 \tag{4.4}
$$

Or, equivalently:

$$
\tilde{\omega}\left(X_1,X_2,T_i\right)<\tilde{\omega}\left(X_1,X_2,T_{i-1}\right)\Longrightarrow\tilde{\omega}\left(X_1,X_2,T_i\right)=\tilde{\omega}\left(X_1,X_2,T_{i-1}\right) \tag{4.5}
$$

Where X_1 and X_2 are the spatial coordinates and T_i represent the i-th time instant.

4.1.2 Numerical Investigation

The beam is supposed constrained on three boundaries. In the fourth boundary no constrains are applied but only a distributed external tensile force f, as shown in Fig. 4.2

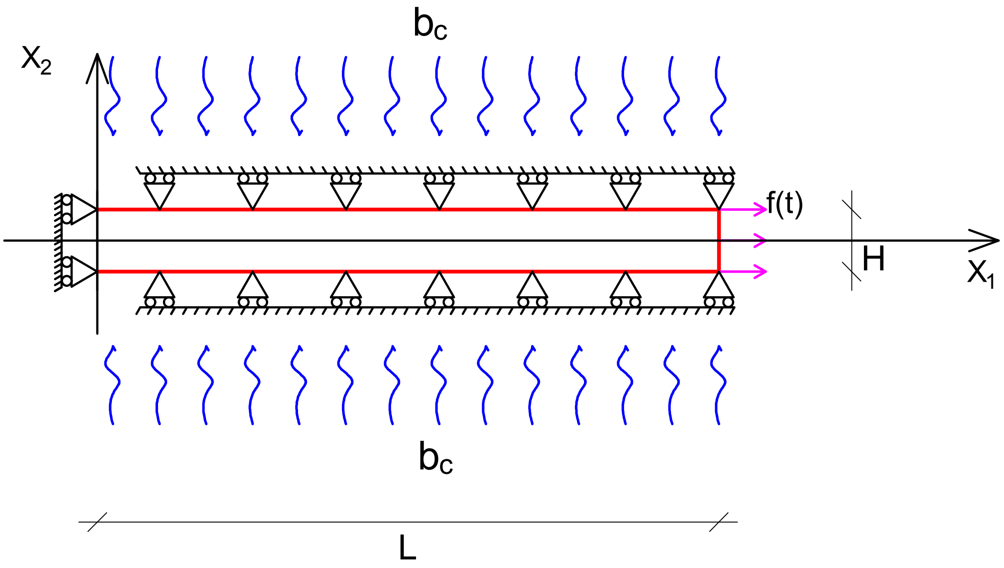

Figure 4.2: 2-D beam model

where L is the length of the beam and H is its height. The imposed external load is represented by a time-dependent external load $f(t)$ whose behaviour in time is shown in Fig. 4.3

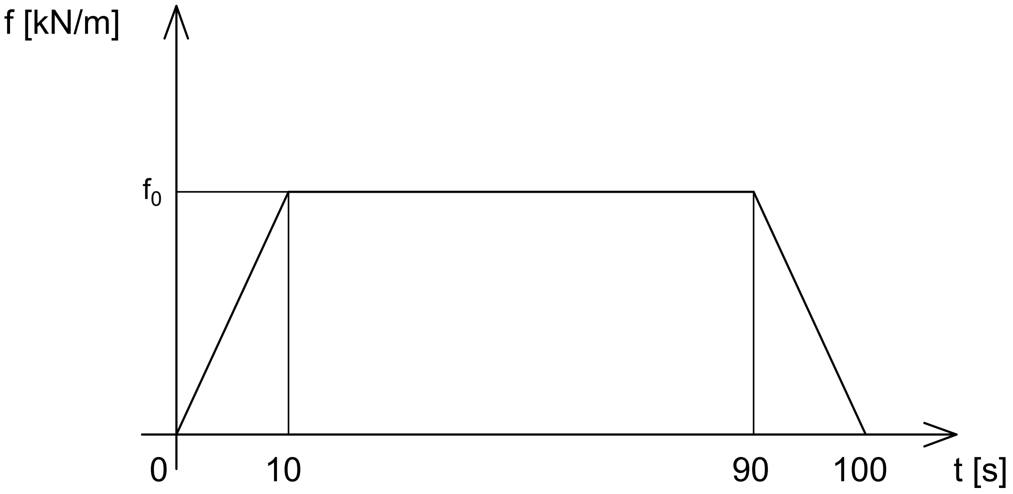

Figure 4.3: Evolution of the distributed external force $f(t)$

The parameters employed in the numerical simulation are presented in Tab. 4.1

$L = 1$ m	$K^{DIFF} = 10^{12}\ \frac{\mathrm{m}^6}{\mathrm{kg \cdot s^2}}$
$H = 0.1$ m	$\bar{b}_c^{ext} = 10^8 \frac{\mathrm{m}^2}{\mathrm{s}^2}$
$t_h = 0.1$ m	$c_c = 10^{16} \frac{\mathrm{m}^4}{\mathrm{kg}}$
$f_0 = 1000 \frac{\mathrm{N}}{\mathrm{m}}$	$K_F = 10^{12}\ \frac{\mathrm{m}^4}{\mathrm{kg \cdot s^2}}$
$E = 4 \cdot 10^9 \frac{\mathrm{N}}{\mathrm{m}^2}$	$K_{c\omega} = -1.25 \cdot 10^3\ \frac{\mathrm{m}^2}{\mathrm{s}^2}$
$\nu = 0.2$	$\bar{K}_{\omega 0} = 4.5 \cdot 10^{-3}\ \frac{\mathrm{N}}{\mathrm{m}}$
$n = 0$	$K_\omega = 4.5 \cdot 10^{-2} \frac{\mathrm{N}}{\mathrm{m}}$

Table 4.1: Parameters for numerical investigation

The Lamè coefficient, λ_0 and μ_0 are calculated from the 2-D Young's modulus $E_{\text{2-D}}$, obtained as $E_{\text{2-D}} = t_h E$. Finally:

$$\lambda_0 = \frac{\nu E_{\text{2-D}}}{(1+\nu)(1-2\nu)} \qquad \mu_0 = \frac{E_{\text{2-D}}}{2(1+\nu)} \tag{4.6}$$

where t_h is the thickness of the specimen. In light of the applied boundary conditions, only the horizontal component of the displacement is shown. Notably, the horizontal displacement at the midpoint of the loaded boundary, with coordinates $(L, 0)$ is highlighted (red point in Fig. 4.4)

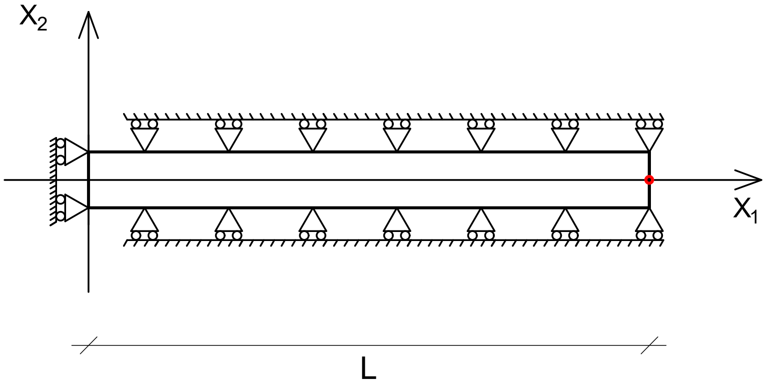

Figure 4.4: Midpoint of the loaded boundary

It is clearly observable how the concentration of the fluid c, by means the damage ω, produce an increasing displacement.

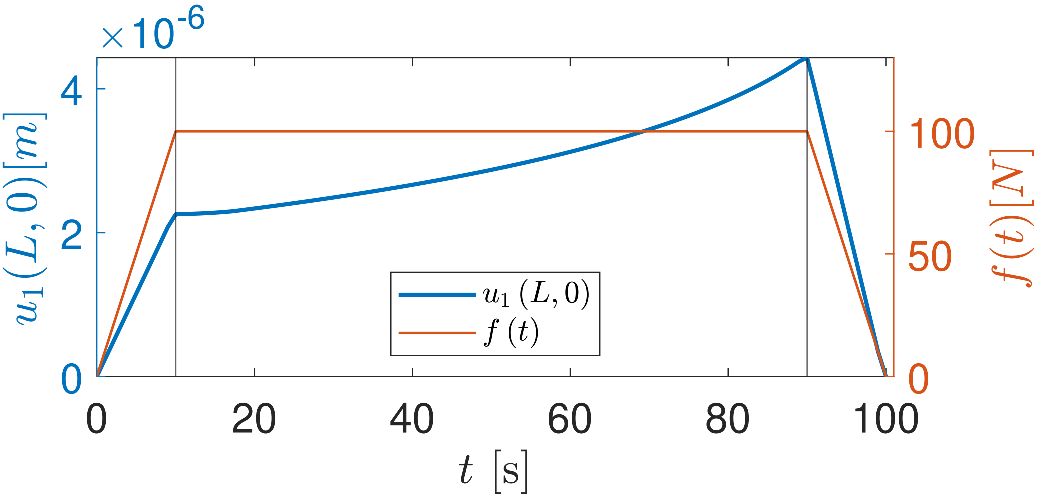

Figure 4.5: Horizontal displacement u_1 of the midpoint with coordinates $(L, 0)$

In the Figs. 4.6 and 4.7 the domain is plotted in its deformed configuration in order to make the evolution of the horizontal displacement easly visible. The force has an increasing ramp during the firsts 10s then it remains constant until the instant $t = 90$s and, finally its value decreases vanishing at instant time $t = 100$s. During the analysis the concentration increases as it is shown in Fig. 4.6.

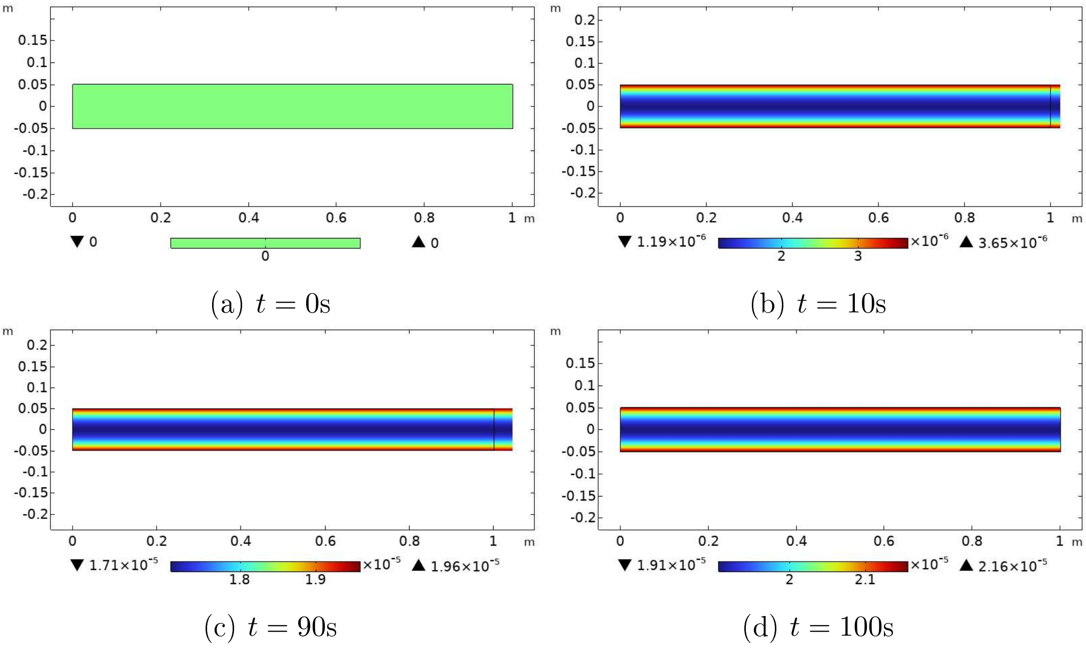

(a) $t = 0$s

(b) $t = 10$s

(c) $t = 90$s

(d) $t = 100$s

Figure 4.6: Concentation c at several time instant: (a) at the beginning of the analysis, (b) at the end of the increasing ramp of the force, (c) at the beginning of the decreasing ramp of the force and (d) at the end of the analysis

For the same time instant in Fig. 4.6 the evolution of the damage ω is shown in the following:

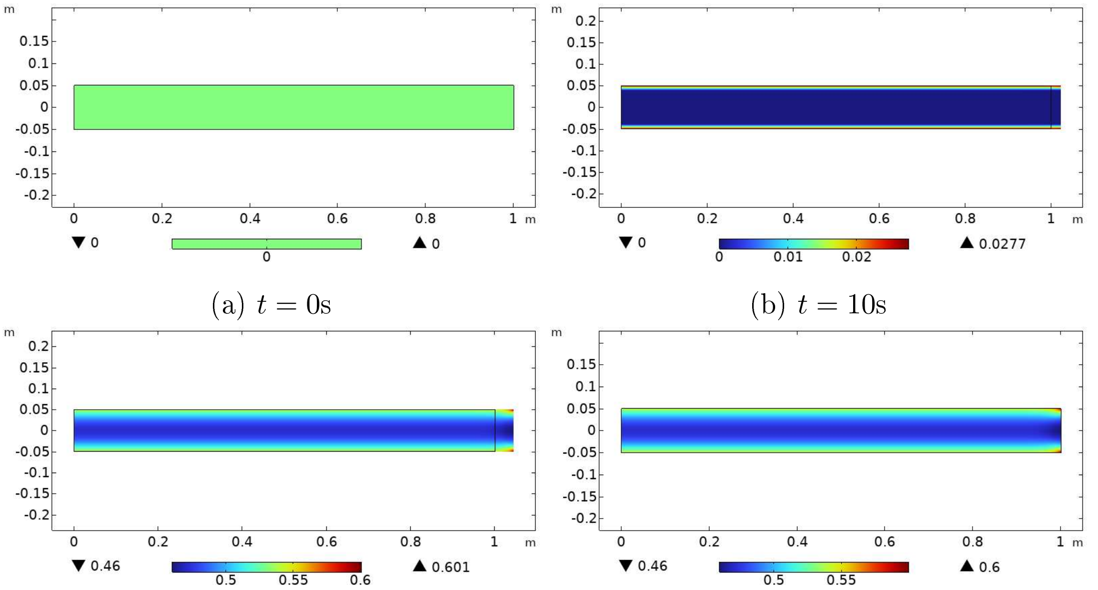

(a) $t = 0$s

(b) $t = 10$s

(c) $t = 90$s

(d) $t = 100$s

Figure 4.7: Damage ω at several time instant: (a) at the beginning of the analysis, (b) at the end of the increasing ramp of the force, (c) at the beginning of the decreasing ramp of the force and (d) at the end of the analysis

Similarly to the dam case, the damage evolution in this instance also resembles that of the concentration following the coupling of the two kinematic descriptors. It should also be noted that there is a localized damage concentration at the right-hand corners. This result is reasonable considering that at these points, with coordinates $(X_1, X_2) = \left(L, \pm\frac{H}{2}\right)$, a double solicitation acts: that due to the external force f applied to the right edge and that related to the presence of b_c^{ext} applied to the upper and lower edges. The softening effect caused by the fluid-induced damage, which reduces the local stiffness. Consequently, the external load results in enhanced horizontal displacements, leading to a positive loop of damage propagation. The temporal profiles of concentration c and damage ω are plotted for the cross-section at the loaded edge (see Fig. 4.9), specifically for all points with coordinates (L, X_2) (with $X_2 \leq \pm\frac{H}{2}$), red line in Fig. 4.8.

The softening effect caused by the fluid-induced damage, which reduces the local stiffness. Consequently, the external load results in enhanced horizontal displacements, leading to a positive loop of damage propagation

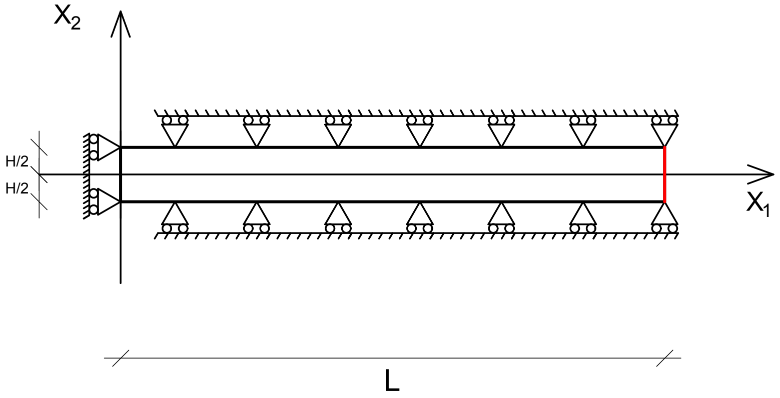

Figure 4.8: Cross-section in which the time-dependent evolution of concentration and damage is tracked

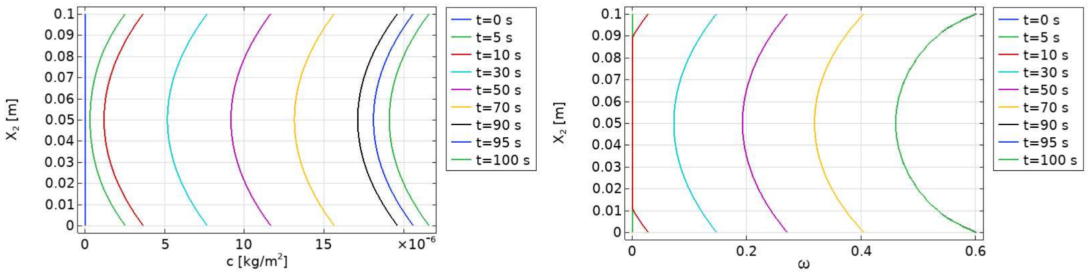

(a) $c(L, X_2, t)$

(b) $\omega(L, X_2, t)$

Figure 4.9: Evolution in time of (a) concentration $c(L, X_2, t)$ and (b) damage $\omega(L, X_2, t)$

Additionally, in Fig. 4.10, the evolution in time of the aforementioned kinematic descriptor at the midpoint (with coordinates $(L, 0)$) at the corner (with coordinates $(L, \frac{H}{2})$) of the loaded boudary (see the red points in Fig. 4.11)

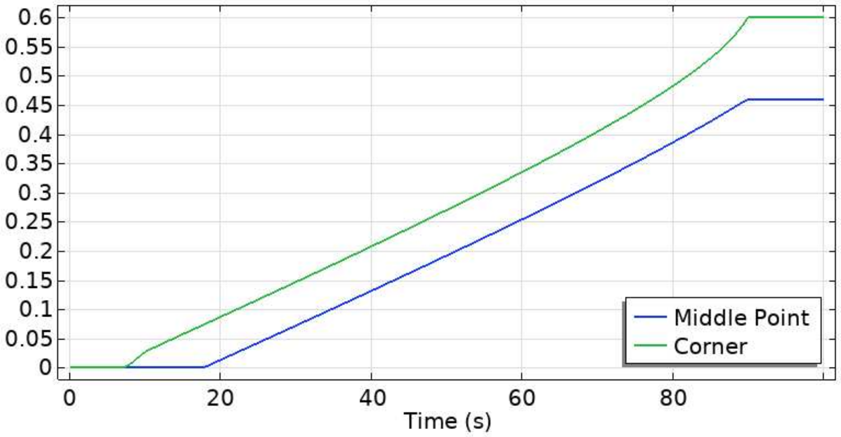

Figure 4.10: Damage ω at the corner and at the middle point of the loaded boundary

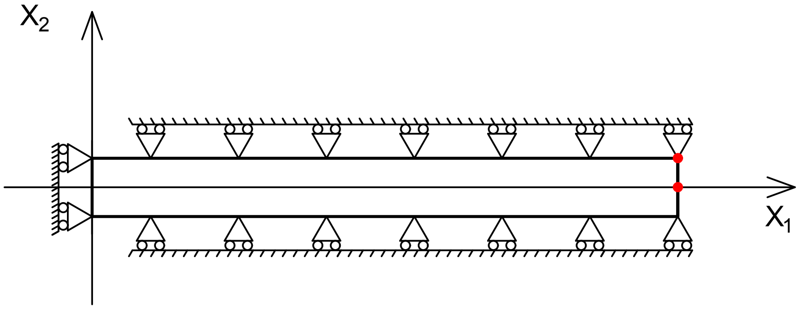

Figure 4.11: Points where the evolution in time of damage $\omega(X_1, X_2, t)$ is computed and shown in Fig. 4.10

In Fig.s 4.9 and 4.10, the damage distribution is more clearly visible than in Fig. 4.7, providing a more plausible explanation for the higher displacements observed at the corners compared to the midpoint.

4.2 Non-linear earthquake

The current paradigm, usually accepted in geophysics, assumes that linear models can be used for describing the wave propagation consequent to tectonic or volcanics energy release, in what is called an earthquake. This paradigm is persistent, albeit more sophisticated non-linear studies in two and three dimensional domains, are widely present in the literature and deal with a wide class of mechanical phenomena (e.g. see [1, 54, 70, 84, 87, 88, 90, 91, 128]) also related to the waves propagation (see [6, 89, 217]). For these types of applications of non-linear continuum mechanics , parameter identification represents a delicate point in the modelling process [2, 49, 65, 96, 97]. In the present paper will will not try to get such an identification in the context of earthquakes modelling: instead we will explore the models potentialities by means of a qualitative and semiquantitative analysis, establishing the conceptual bases for further investigations. While the linearised approach to earthquake dynamics and wave propagation, often linked to the forcing and free vibration of the structures, (see e.g. [38, 100, 129, 133, 214, 215]) has produced very interesting and useful results, we claim that non-linear continuum mechanics gives a logical evidence that, in some specific instances, this approach cannot be accepted and must be modified. In particular we state that when the medium in which the waves are propagating is strongly inhomogeneous, so that the fields of stiffnesses are suffering high gradients, and when the earthquake energy release is sufficiently high, then non-linear behaviour may become not negligible [51, 117, 161, 188], also in the simplest case of purely geometrical non-linearities: to be more precise we remark here that, in the case examined in the numerical simulations of this paper, the released energy is estimated to be equivalent to the energy of an earthquake with a moment magnitude of 6, as described in [66]. As a consequence of our results, we urge for the introduction of more sophisticated non-linear models and numerical techniques, in order to get the required precise predictions of the earthquakes effects, especially when their energy is large. In this paper the analysis is restricted to a two-dimensional case in order to get qualitative and preliminary quantitative information about the properties of considered mechanical systems and in order to prepare the more realistic three-dimensional analysis, which is needed to face the modelling problem arising when dealing with seismic propagation in the Aterno River Valley, where the city of L'Aquila is located. To make clearer the modelling challenges to be confronted we shortly recall, in what follow, the basic phenomenology whose modelling we intend to develop here and in our future planned investigations. The city of L'Aquila is located in the central part of the Apennine chain (central Italy), in a seismic area characterized by normal fault earthquakes [66, 209]. This area (called "aquilano") has been struck in the past by numerous earthquakes such as those of 1315, 1349, 1461, 1703 and the recent one on 6 April 2009 (M_w6.3, [52] which macroseismic intensities up to XI on the Mercalli-Cancani-Sieberg scale (MCS), corresponding to an Ms close to 7 and causing deaths and damage; the Fig. 4.12 shows the macroseismic intensities relating to the city of L'Aquila [179, 180].

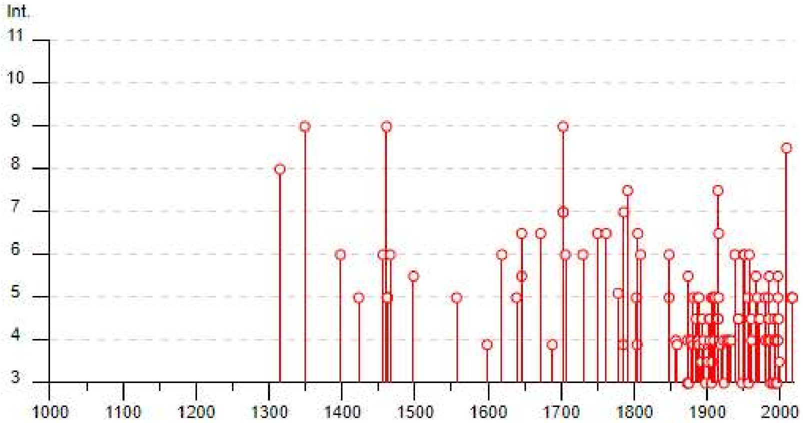

Figure 4.12: Macroseismic intensities relating to the city of L'Aquila plotted as time(years) vs intensity

Before the 2009 event, the presence of seismic amplification in the city of L'Aquila was already known (within its historic walls) [67] and since then numerous work were published on seismic microzonation (see e.g. [31, 42, 81, 98, 99, 172, 189, 206]), on strong motion data (see e.g. [8, 10, 33, 116, 127, 219]), on earthquake engineering (see e.g. [18, 50, 61, 134, 181, 200, 205]), on damage distribution (see e.g. [83, 204, 205, 222]), on geological works (see e.g. [35, 39, 56, 148, 196, 202]), on geotechnical works (see e.g. [127, 145, 207]) and on numerical modeling (see e.g. [82, 102, 130, 149–151, 192, 219]). We remark that in [67] one can find a first attempt aimed to explain the observed seismic wave amplification effect (up to 10) in the 0.4 - 0.8 Hz frequency range . Of course, the 2009 L'Aquila earthquake has been largely discussed in the literature (see e.g.[33, 52, 67, 82, 102, 130, 135]) and it is well-established that this geographic area shows different geological layers, as it was exposed already in [67], some years before of the seismic event that occurred in the city of L'Aquila in 2009. Always in [67]: i) some preliminary 1-D and 2-D linear continuum models for the superficial crust under the city of L'Aquila were introduced and it was proven that, also by using such linear models, it can be forecast that the discontinuity of stiffnesses must greatly affect the ground accelerations, the frequency ratios and the seismic wave propagation velocities; ii) some interesting experimental investigations in the urban area of the city were presented: in particular weak-motion data from earthquakes and ambient noise data were collected and analyzed. This experimental evidence given by weak-motion data share the same characteristics as the strong-motion records and shows clearly the presence of the amplification effect in the city. The geophysical model on which [67] is based proves that *the ground-motion amplification in the city of L'Aquila is related to the presence of a sedimentary basin, filled by lacustrine sediments, with a maximum depth of about* 250 *m.* Such area, situated in central Italy, is formed by NW-SE-dipping normal faults which produced rift valleys features typical to the intermontane basins (see e.g. [19, 44, 45, 60]). Several of these faults are still active and they may be responsible for further future earthquakes (see e.g. [37, 80, 101, 170]) .

In this paper we investigate the wave propagation in a two-dimensional continuous Cauchy medium caused by a forcing excitation, modelling the effects of high energy earthquakes (moment magnitude higher than 6) originated at hypocenters far from the modelled region, where the seismic wave propagation is studied. In fact, the source of the seismic excitation in 2009 L'Aquila Earthquake was located 10km below the modelled region, whose thickness is about 1km: we explicitly remark that cannot use here the expression "deeper hypocenter", as the usual geological meaning of the term "deeper" in this context indicates that the hypocenter is located in the mantel under the crust. We consider, at first, linear models, that are models in which the deformation energy is assumed to be isotropic and quadratic in the linear deformation measure (i.e. the so-called infinitesimal strain tensor). Our aim, in this paper, is to prove that linear models are not fully capable to describe the phenomena occurring when it is necessary to consider continuous models featuring stiffness fields with high spatial gradients: this being the case when strongly-non-homogeneous seismic wave propagation regions are to be considered (see e.g. [14, 27, 132]). In order to consider the simplest non-linear model, we introduce what is usually called a geometric non-linearity, by assuming that the isotropic deformation energy depends quadratically but on the finite strain tensor instead of depending on the linearised deformation measure [113]. We prove, with numerical simulations, that, the predictions of non-linear models dramatically differ from those obtained with linear models. These results seem to indicate, in particular in the case of the earthquakes propagating in the Aterno River Valley, that more sophisticated analyses are needed, if one wants to predict in a reliable way the effects of seismic waves on buildings and infrastructures. In fact, in the Aterno Valley, it is well-established that (see [67] and the references there cited) the ratio between the average stiffnesses observed in the soft alluvial sand or silt deposits layers and in the hard bedrock or calcareous breccia layer is, at least, one to four, so that high gradients of the stiffness fields are concentrated at the interface regions between these different layers or between the bedrock and the soft materials. It has to be remarked that in the literature also different modelling approaches have been attempted when considering linear or non-linear waves propagation. In fact, some discrete models based on lattice dynamics methods could be applied: see e.g. [164, 166, 191] where transmission, refraction and leakage of wave in the vicinity of surface defect were considered. Moreover, some surface-related phenomena in layered structures have been studied recently in [137], where other references could be found. We believe, however, that the numerical implementation of continuum models, also in presence of non-linearities, is so well-established and reliable that, at the moment, the approach which we used must be preferred. Because of the numerical simulations which we have performed, we have observed that the field of deformation (and kinetic) energy density difference between the linear and non-linear predictions, normalised with respect to the average deformation (and kinetic) energy in the non-linear case, starts being concentrated in the hard/soft interfaces at the beginning of the dynamic load (modelling the earthquake) and then propagates in both the soft and hard region: the amplitude of this propagating field may reach the values higher than 100% in a large region of the domain. Because of their applicative importance, the linear and non-linear acceleration field in several points close to the boundaries and their differences are calculated and discussed. The accelerations are normalised with respect to the gravity acceleration g and the difference between these two quantities can reach values around $0.77g$. We can conclude that the numerical evidence, which we have obtained, demands the development of more refined non-linear models for describing, in particular, the phenomenology observed in the city of L'Aquila during large energy earthquakes. Albeit for the numerical simulations we have used the standard package included in COMSOL, some non trivial encoding solutions have been used: i) the same finite elements procedure has been used for solving simultaneously the linear and non-linear problem, ii) a purely variational approach has been implemented, using suitable Hamilton conservative and Rayleigh dissipation functionals in the coding procedure, iii) in order to avoid the reflection back inside the region of interest of the passing wave at its boundaries, we have chosen suitable optimal boundary conditions implementing viscoelastic displacement-force relationships at the lateral boundaries of the considered wave propagating region, while at its bottom a spherical displacement wave, originated in the hypocenter is imposed: the fact that the forcing action is originated by a far hypocenter is modelled by imposing at the basis of the bedrock a displacement calculated with a spherical wave transporting the required earthquake energy [16, 119]. The very preliminary results, which we announce here, require the development of a more sophisticated analysis in which: i) isotropy hypothesis is relaxed; ii) the material elastic non-linearities are included in the modelling scheme; iii) the creep, damage and plasticity effects are suitably accounted for; iv) the second gradient deformation energy is postulated, for giving a better description of the boundary layers formed at the interfaces (see e.g. [11, 59, 64, 77, 169, 171, 177, 194, 227]), also accounting for the change of the microstructure [109, 110, 152, 203] and of the granular (and porous) nature of the soils ([24, 139, 155, 186, 210, 218]) due to which strong local and macro-to-micro scale differences can be highlighted; v) the complete three-dimensional problem for the Aterno Valley is considered, in order to fully account for the peculiar behaviour experimentally observed in [67].

4.2.1 Geological setting of L'Aquila basin

In this section we motivate our modelling assumptions on the basis of what we know about the geological structure of the crust immediately under the city of of L'Aquila. It is located in a tectonic basin (Aterno river) bounded by a northwest-southeast-active normal fault ($https : //diss.ingv.it/new - in - diss - 3 - 3 - 0$) and it was founded in 1245, so that we have somehow detailed records about the seismic activity in its basic since then. The current tectonic setting of central Italy is due to the superposition of a previous a compressive phase (middle Oligocene - lower Pliocene, 28-3.6 Myr) during which the Apennine chain was created and the subsequent the post-orogenic extensional phase characterized by the origin of intermontane basins scattered in the central Apennine chain (such as L'Aquila basin - henceforth LAB in which is placed L'Aquila city) in the Messinian-Quaternary (7 Myr till now) [35, 44, 45, 60]. LAB is placed in a NW-SE trending Plio-Quaternary intermontane tectonic basin bounded by SW dipping active normal fault accountable for the current and historical seismicity. [101, 179]. LAB is filled up by lacustrine, slope and alluvial deposits dated back from the upper Pliocene to the present (3.6 Myr till now) and laying via an unconformity surface onto the Messinian (7.2-5.3 Myr) terrigenous units and Meso-Cenozoic (100-70 and 20-12 Myr) carbonate units. LAB oldest post-orogenic deposits, made up by slope breccias and alluvial conglomerates, belong to the Colle Cantaro-Cave Formation (CCF) (upper Piacenzian-Gelasian 3.0-1.8 Myr) [60, 147, 148]. The Madonna della Strada Synthem (MDS), (in this study the soft layer) which is separated from the underlying CCF by an unconformity boundary, is made up by clayey-sandy silts and sands of Calabrian age (1.8-0.8 Myr) and referred to an alluvial meandering system within a wide and swampy floodplain [60]. Above MDS, separated by an unconformity boundary, the Middle Pleistocene (0.8-0.12 Myr) Fosso Genzano Synthem (FGS) is placed. It consists of gravels and sands referred to alluvial fans and plains [202]. The hill, where the L'Aquila historic downtown stands, is mainly made up by late Middle Pleistocene (0.3-0.12 Myr) calcareous breccias (in this study the hard layer) which, via an erosive boundary, are superimposed on the underlying MDS and FGS deposits and the Meso-Cenozoic bedrock [13]. In fact, the historical part of the city (within the ancient walls) is placed on a fluvial terrace in the left bank of the Aterno River. The elevation of the terrace reaches 900 m a.s.l. (above mean sea level) in the NE part of the city and slopes down to 675 m in the SW direction. The terrace ends at the Aterno River which flows 50 m below yet. The terrace is made up of alluvial deposits created in the lower Quaternary age and is composed of breccias with limestone boulders and clasts in a marly matrix. The dimensions of these clasts can range from centimeters to some meters. This deposit is common in the Abruzzo region and may be related to catastrophic alluvial events associated with landslides (see e.g. [36]). These terrace were studied by Demageout [40], who named them "megabrecce". The "megabrecce" (called "mega breaches" in English) represents a well-defined geological unit with a thickness of some tens of meters. These deposits (megabrecce) are placed on the lacustrine sediments composed mainly of silty and sandy layers and minor gravel beds that can generate earthquakes with maximum expected magnitudes up to 6.5-7 [101]. The lacustrine sediments have their maximum thickness (around 300 m) in the center of the city of L'Aquila. In contrast, in the Aterno River valley, at north of L'Aquila, the thickness of the sediments is never greater than 100 m.

Further information about geological setting of L'Aquila basin will be exploited in future modelling efforts: in particular when 3D models will be used for getting the required predictions.

4.2.2 Modelling and coding assumption

In this section we define univocally both the linear and non-linear models on the basis of which the analyses will be performed. The soil is modelled as a 2-dimensional domain and each of its material particles will be characterised with the coordinate $\mathbf{X} = X_i \hat{\mathbf{e}}_i$ (where $\|\hat{\mathbf{e}}_i\| = 1$ and $i = 1, 2$) in a given reference configuration. The set of the kinematical descriptors, which depend upon the coordinates $\mathbf{X}$ and the time t, is composed of (i) the horizontal displacement $u_1(X_1, X_2, t)$ and (ii) the vertical displacement $u_2(X_1, X_2, t)$. Let $\mathbf{u}(\mathbf{X}, t) = u_i \hat{\mathbf{e}}_i$ be the displacement vector of the generic point with X_i coordinates, $\mathbf{\Phi}(\mathbf{X}, t)$ be the placement function, $\mathbb{F}$ be the deformation gradient tensor and $\mathbb{G}$ be the finite strain tensor. We will indicate with $\mathbf{x} = x_i \hat{\mathbf{e}}_i$ the coordinates in the current configuration, of the material point having coordinates $\mathbf{X}$ in the reference configuration. In formulae,

$$\mathbf{x} = \mathbf{\Phi}(\mathbf{X}, t) = \mathbf{X} + \mathbf{u}, \qquad \mathbb{F} = \nabla \mathbf{\Phi}, \qquad \mathbb{G} = \frac{1}{2}\left(\mathbb{F}^T \mathbb{F} - \mathbb{I}\right) \tag{4.7}$$

or, in index notation:

$$\Phi_i = X_i + u_i, \qquad F_{ij} = \frac{\partial \Phi_i}{\partial X_j} = u_{i,j} + \delta_{ij}, \qquad G_{ij} = \frac{1}{2}\left(F_{ki} F_{kj} - \delta_{ij}\right) \tag{4.8}$$

where

$$u_{i,j} = \frac{\partial u_i}{\partial X_j} \qquad \text{and} \qquad \delta_{ij} = \begin{cases} 1 & i = j \\ 0 & i \neq j \end{cases} \tag{4.9}$$

4.2.2.1 Deformation and kinetic energies and Rayleigh functional

Let $\mathcal{W}^{el}$ and $\mathcal{K}$ be, respectively, the elastic internal deformation and the kinetic energies, respectively, and let $\partial_f \mathcal{B}$ be a subdomain of the boundary $\partial \mathcal{B}$ of the body $\mathcal{B}$ (see the Fig. 4.14)

$$\mathcal{W}^{el} = \int_{\mathcal{B}} \left[\frac{1}{2}\lambda \left(\text{tr}\mathbb{G}\right)^2 + \mu \text{tr}\left(\mathbb{G}^2\right)\right] dA + \int_{\partial_f \mathcal{B}} \frac{1}{2} K \mathbf{u} \cdot \mathbf{u} ds \tag{4.10}$$

$$\mathcal{K} = \int_{\mathcal{B}} \frac{1}{2} \rho \dot{\mathbf{u}} \cdot \dot{\mathbf{u}} dA \tag{4.11}$$

where λ and μ are the 2-D Lamè coefficients and ρ is the mass density (per unit area) of the 2D domain, listed in Tab. 4.2, and K is the elastic stiffness per unit line of the bed of springs applied at the vertical boundaries $\partial_f B$, also listed in Tab. 4.2 (and shown in Fig. 4.14). The dot between two vectors $\mathbf{a}$ and $\mathbf{b}$, denoted by $\mathbf{a} \cdot \mathbf{b}$, is their scalar product. Let the dissipation energy be:

$$\mathcal{W}^{dis} = \int_{\mathcal{B}} \mathcal{R}_{\mathcal{B}} dA + \int_{\partial_f \mathcal{B}} \mathcal{R}_f ds \tag{4.12}$$

and the two integrands have the following expression,

$$\mathcal{R}_{\mathcal{B}} = \frac{1}{2}\lambda_v \left(\text{tr}\dot{\mathbb{G}}\right)^2 + \mu_v \text{tr}\left(\dot{\mathbb{G}}^2\right) \tag{4.13}$$

$$\mathcal{R}_f = \frac{1}{2} c \dot{\mathbf{u}} \cdot \dot{\mathbf{u}} \tag{4.14}$$

here, λ_v is a coefficient of viscosity and μ_v is the shear viscosity of the 2D domain, listed in Tab. 4.2 and c is the damping coefficient per unit line of the bed of dashpots applied at the vertical boundaries $\partial_f B$, also listed in Tab. 4.2. The linear approximation the non-linear deformation defined at the third place of (4.7) is given by

$$\mathbb{G} = \frac{1}{2}\left(\nabla \mathbf{u} + \nabla \mathbf{u}^T + \nabla \mathbf{u}^T \nabla \mathbf{u}\right) \quad \longrightarrow \quad \mathbb{E} = \frac{1}{2}\left(\nabla \mathbf{u} + \nabla \mathbf{u}^T\right). \tag{4.15}$$

So that in index notation we have

$$E_{ij} = \frac{1}{2}\left(u_{i,j} + u_{j,i}\right) \tag{4.16}$$

From the virtual work principle [103], indicating with t_1 and t_2 two different instants of time where the displacements $\mathbf{u}(\mathbf{X}, t_1)$ and $\mathbf{u}(\mathbf{X}, t_2)$ are known, the action is defined as a functional of the displacement function $\mathbf{u}(\mathbf{X}, t)$ as follows:

$$\mathcal{A}\left(u_1, u_2\right) = \int_{t_1}^{t_2} \left[\mathcal{W}^{el} - \mathcal{K}\right] dt \tag{4.17}$$

its first variation is:

$$\delta \mathcal{A} = \mathcal{A}\left(u_1 + \delta u_1, u_2 + \delta u_2\right) - \mathcal{A}\left(u_1, u_2\right) \tag{4.18}$$

The variation (4.18), by separately analyzing the two terms of (4.17) can be thought of as the sum of the following quantities

$$\int_{t_1}^{t_2} \delta \mathcal{W}^{el} = \int_{t_1}^{t_2} \frac{\partial \mathcal{W}^{el}}{\partial G_{ij}} \delta G_{ij} dt = \int_{t_1}^{t_2} \int_{\mathcal{B}} \left[\lambda G_{ii} \delta G_{jj} + 2\mu G_{ij} \delta G_{ij}\right] dA dt + \int_{t_1}^{t_2} \int_{\partial_f \mathcal{B}} K u_i \delta u_i ds dt \tag{4.19}$$

and

$$\int_{t_1}^{t_2} \delta\mathcal{K}dt = \int_{t_1}^{t_2}\int_{\mathcal{B}} \rho\dot{\mathbf{u}}\cdot\delta\dot{\mathbf{u}}dAdt \tag{4.20}$$

Integrating (4.19) by parts, some spatial boundary terms are naturally obtained as a consequence one obtains an equivalent representation for (4.19). It is important to note that, following integration by parts, only on the boundary denoted by $\partial_f\mathcal{B}$ (see Fig. 4.14) natural boundary conditions need to be added. This is because on the bottom blue boundary (also Fig. 4.14), displacements (i.e. essential boundary conditions) are imposed, and therefore their variation is zero. Instead, integrating (4.20) by parts in time, we obtain

$$\begin{aligned}\int_{t_1}^{t_2} \delta\mathcal{K}dt &= \int_{t_1}^{t_2}\int_{\mathcal{B}} \frac{\partial}{\partial t}\left[\rho\dot{\mathbf{u}}\cdot\delta\mathbf{u}\right]dAdt - \int_{t_1}^{t_2}\int_{\mathcal{B}} \rho\ddot{\mathbf{u}}\cdot\delta\mathbf{u}dAdt \\ &= \int_{\mathcal{B}}\left[\rho\dot{\mathbf{u}}\cdot\delta\mathbf{u}\right]_{t_1}^{t_2}dA - \int_{t_1}^{t_2}\int_{\mathcal{B}} \rho\ddot{\mathbf{u}}\cdot\delta\mathbf{u}dAdt\end{aligned} \tag{4.21}$$

If the displacement at the times t_1 and t_2 are known and their variation $\delta\mathbf{u}$, for those instants of time, are equal to 0, then from (4.21) we have,

$$\int_{t_1}^{t_2} \delta\mathcal{K}dt = -\int_{t_1}^{t_2}\int_{\mathcal{B}} \left[\rho\ddot{\mathbf{u}}\cdot\delta\mathbf{u}\right]dAdt \tag{4.22}$$

The variation of the dissipative term $\mathcal{W}^{dis}$ in the (4.12) is defined as $\tilde{\delta}\mathcal{W}^{dis}$. The symbol of the variation operator we used for this quantity is different with respect total one present in (4.18) because such term is not a classic variation. The variation of the dissipative term is defined by the following expression:

$$\tilde{\delta}\mathcal{W}^{dis} = \int_{t_1}^{t_2}\left[\int_{\mathcal{B}} \frac{\partial\mathcal{R}_{\mathcal{B}}}{\partial\dot{G}_{ij}}\delta G_{ij}dA + \int_{\partial_f\mathcal{B}} \frac{\partial\mathcal{R}_f}{\partial\dot{u}_i}\delta u_i ds\right]dt \tag{4.23}$$

Also for (4.23) the integration by parts provides naturally the boundaries terms on $\partial_f\mathcal{B}$, where no kinematical restrictions are imposed. Finally, the variational principle is formulated as follows:

$$\delta\mathcal{A} + \tilde{\delta}\mathcal{W}^{dis} = 0 \tag{4.24}$$

for any admissible variation of the kinematic descriptors. On the red lateral boundaries (Fig. 4.14) two different conditions are imposed: (i) a boundary damping constrain (as it is prescribed in the (4.14)) modeled as a bed of dashpots to avoid non-realistic reflections of the wave at the boundaries of the model. Some dissipation phenomena [32] may essentially change the wave propagation, see e.g. [85]. Insertion of (4.14) into (4.23) yields from (4.24) a standard dissipative force at the vertical boundary,

$$\int_{\partial\mathcal{B}} c\dot{\mathbf{u}}\cdot\delta\mathbf{u}ds. \tag{4.25}$$

and (ii) a distributed force, modeled by means a bed of springs with stiffness equal to K and prescribed in the last boundary term of (4.10), to simulate the reaction of the lateral ground. Insertion of the last term of (4.10) into (4.17) yields from (4.24) a standard elastic force at the vertical boundary,

$$\int_{\partial\mathcal{B}} K\mathbf{u}\cdot\delta\mathbf{u}ds \tag{4.26}$$

4.2.2.2 The stiffness fields in the soft and hard region and kinematic boundary conditions

Based on the evidence made available e.g. by [67], the region where seismic waves propagate is supposed to be constituted by two different materials, characterised by two different stiffnesses (the Young's moduli of the softest and the stiffest layers exhibit a 1/4 ratio as shown in the Tab. 4.2) and the 2-D Lamè parameters were determined (the justification of the whole modelling procedure is similar to what done in [23], to which we refer) using the following relationships for the plane stress case:

$$\lambda = \frac{Y\nu}{(1+\nu)(1-2\nu)},\ \mu = \frac{Y}{2(1+\nu)} \tag{4.27}$$

where Y represents the 2-D Young's modulus and ν is the 2-D Poisson coefficient. In the Tab. 4.2 we use the index s and h to denote that the parameter is linked either to the softer or to harder layers. The softer layer is located between the two harder layers as it is shown in the Fig. 4.14.

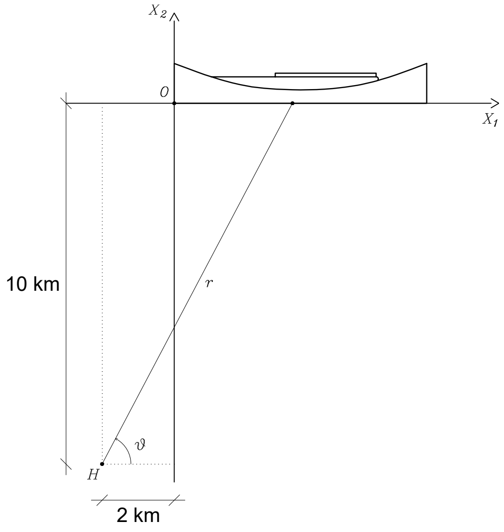

Figure 4.13: 2-D model: the body is modeled as a domain that consists of three main parts, in which two of these are harder then the other one. The seismic excitation starts at the hypocenter having coordinates $H \equiv (X_{H1}, X_{H2}) = (-2\text{km}, -10\text{km})$.

Clearly the distance r of the generic point of the bottom boundary (blue part of the boundary in Fig. 4.14), with coordinates $(X_1, 0)$ (with $X_1 \in [0, 7]$ km), from the hypocenter is:

$$r = \sqrt{(X_1 - X_{H1})^2 + (X_2 - X_{H2})^2} = \sqrt{(X_1 - X_{H1})^2 + X_{H2}^2} \tag{4.28}$$

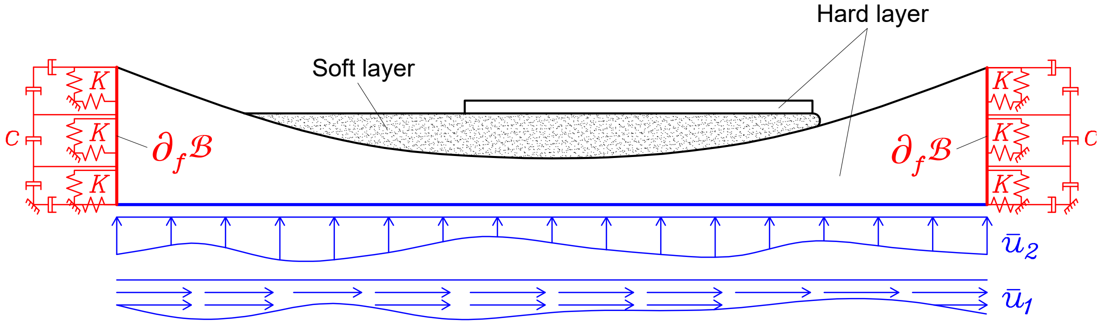

Figure 4.14: Boundary conditions: three boundary conditions were taken into account. On the two red lateral boundaries, indicating as $\partial_f \mathcal{B}$, are imposed a damping condition, derived from (4.25), and an elastic one, derived from (4.26). On the blue bottom boundary one has a boundary condition in terms of the displacements, see (4.38) and (4.39).

In the Fig. 4.14 one can see how on the blu boundary at the bottom, the displacement $\bar{\mathbf{u}}$ is imposed for modelling the seismic action. The excitation originates from the hypocenter (point H in Fig. 4.13), spreads into the ground until it reaches the "inhomogeneous superficial region" where wave propagation is analysed. The seismic excitation is assumed to last 3 seconds. Roughly speaking the imposed displacement is the result of the compositions of several waves (3 longitudinal and 3 shear ones). To be more precise, the seismic excitation is modelled by means of the following simplifying assumptions: i) it propagates as a spheric wave that diffuses, under the studied region of propagation, from an hypocenter H (see Fig. 4.13), with coordinates $(X_{H1}, X_{H2}) = (-2\text{km}, -10\text{km})$, situated below the region bottom boundary (the blu boundary in the Fig. 4.14); ii) it interacts with the inhomogeneous superficial region through the blu boundary by "imposing" its displacement; iii) it does not affect the lateral boundary of the inhomogeneous superficial region, where only linear elastic conservative and dissipative interactions occur between the neighboring parts of crust. This last modelling choice, of course, limits the quantitative predictability of the introduced model, but we believe that it does not affect the qualitative features of the calculated solutions and makes reasonable the computing burden: it will be improved in future investigations, where more powerful computing tools will be used.

Starting from the meaning of the symbol used in Fig. 4.13 the unit vector $\hat{\mathbf{r}}$ indicates the direction of the vector r and its orthogonal unit vector $\hat{\mathbf{t}}$ (they are needed to determine, respectively, the longitudinal and the shear waves oscillation direction) can be written as:

$$\hat{\mathbf{r}} = \cos\vartheta \hat{\mathbf{e}}_1 + \sin\vartheta \hat{\mathbf{e}}_2 \tag{4.29}$$

$$\hat{\mathbf{t}} = -\sin\vartheta \hat{\mathbf{e}}_1 + \cos\vartheta \hat{\mathbf{e}}_2 \tag{4.30}$$

The vector displacement (see e.g. [133] for a similar analysis), assuming that the discrete spectrum includes 3 different frequencies, is the real part of:

$$\bar{\mathbf{u}} = \Sigma_{j=1}^{3} \left[\frac{A_{jl}}{r} \hat{\mathbf{r}} e^{i\left(\omega_{jl} t - k_{jl} r\right)} + \frac{A_{js}}{r} \hat{\mathbf{t}} e^{i\left(\omega_{js} t - k_{js} r\right)} \right] \tag{4.31}$$

where

$$\omega_j = \omega_{jl} = \omega_{js} \qquad \text{for } j = 1, 2, 3 \tag{4.32}$$

$$A_j = A_{jl} = A_{js} \qquad \text{for } j = 1, 2, 3 \tag{4.33}$$

where (i) ω_{jl} and ω_{js} are the frequencies of the longitudinal (index l) and shear (index s) waves which are equal to each other in the analysed example (4.32), (ii) A_{jl} and A_{js} represented the source of the longitudinal and the shear waves respectively, (iii) k_{jl} and k_{js} are the wavenumber of the longitudinal and the shear waves respectively and the ratios between those terms and the frequency ω_j represent the velocities of the waves (principal and shear waves), so that

$$k_{jl} = \frac{\omega_j}{v_{wl}} \qquad \text{for } j = 1, 2, 3 \qquad \text{(for the longitudinal waves)} \tag{4.34}$$

$$k_{js} = \frac{\omega_j}{v_{ws}} \qquad \text{for } j = 1, 2, 3 \qquad \text{(for the shear waves)} \tag{4.35}$$

It is possible to prove that the velocities are related to the Lamè constants as follows,

$$v_{wl} = \sqrt{\frac{\lambda + 2\mu}{\rho}} \tag{4.36}$$

$$v_{ws} = \sqrt{\frac{\mu}{\rho}} \tag{4.37}$$

Manipulating (4.29) and (4.30) by means the (4.28), the displacements imposed at the bottom boundary, by the (4.31), are:

$$\bar{u}_1\left(X_1\right) = a_{n1}(t) \Sigma_{h=1}^{3} \left[\frac{X_1 - X_{H1}}{r^2} A_h \sin\left(\omega_h t - k_{hl} r\right) - \frac{X_{H2}}{r^2} A_h \sin\left(\omega_h t - k_{hs} r\right) \right] \tag{4.38}$$

$$\bar{u}_2\left(X_1\right) = a_{n1}(t) \Sigma_{h=1}^{3} \left[\frac{-X_{H2}}{r^2} A_h \sin\left(\omega_h t - k_{hl} r\right) - \frac{X_1 - X_{H1}}{r^2} A_h \sin\left(\omega_h t - k_{hs} r\right) \right] \tag{4.39}$$

where we have pre-multiplied the (4.38) and the (4.39) with a_{n1} that is a window function that allow to consider only the signals into a specific time interval. Note that the amplitude of the imposed waves near the lower blue boundary (which is farther from the hypocenter where the waves originate and propagate through the ground) is on the order of millimeters.

Soft domain	Hard domains	Boundary
$Y_s = 10\text{GPa}$	$Y_h = 40\text{GPa}$	$c = 10^8 \frac{\text{Ns}^2}{\text{m}^2}$
$\nu_s = 0.1$	$\nu_h = 0.25$	$K = 4.5 \frac{\text{N}}{\text{m}^2}$
$\lambda_{vs} = 5.2 \cdot 10^7 \text{Nms}^2$	$\lambda_{vh} = 2 \cdot 10^5 \text{Nms}^2$	
$\mu_{vs} = 1.44 \cdot 10^8 \text{Nms}^2$	$\mu_{vh} = 4 \cdot 10^5 \text{Nms}^2$	
$\rho_s = 1500 \frac{\text{kg}}{\text{m}^3}$	$\rho_h = 2700 \frac{\text{kg}}{\text{m}^3}$	

Table 4.2: Material parameters that are used on the simulations. The indices s and h are linked with the layer in which the parameter is defined, respectively *softer* and *harder* one in Fig. 4.14. Boundary parameters are also defined

The three-dimensional Young's moduli Y_s, Y_h, presented in Tab. 4.2, are multiplied by an assumed out of plane depth of $d = 1\text{m}$ to derive the analogous quantities for the bi-dimensional domain, $Y_s^{2D} = Y_s d$ and $Y_h^{2D} = Y_h d$. Then, the Lamè coefficients employed in Eq. (4.10) for both the softer and harder layers are determined by Eq. (4.27), under the following assumptions:

$$Y = Y_s^{2D}, \quad \nu = \nu_s \qquad \text{for the softer layer} \tag{4.40}$$

$$Y = Y_h^{2D}, \quad \nu = \nu_h \qquad \text{for the harder layers} \tag{4.41}$$

Also the mass densities ρ_s and ρ_h are multiplied for the same assumed out of plane depth $d = 1\text{m}$ to yield the density for the two-dimensional domain under investigation to insert into the (4.11) under the following assumption:

$$\rho = \rho_s^{2D} \qquad \text{for the softer layer} \tag{4.42}$$

$$\rho = \rho_h^{2D} \qquad \text{for the harder layers} \tag{4.43}$$

The waves' parameters are shown in Tab. 4.3

Wave 1	Wave 2	Wave 3
$\omega_1 = 1.571 \frac{\text{rad}}{\text{s}}$	$\omega_2 = 3.142 \frac{\text{rad}}{\text{s}}$	$\omega_3 = 15.708 \frac{\text{rad}}{\text{s}}$
$v_{wl} = 4216.4 \frac{\text{m}}{\text{s}}$	$v_{wl} = 4216.4 \frac{\text{m}}{\text{s}}$	$v_{wl} = 4216.4 \frac{\text{m}}{\text{s}}$
$v_{ws} = 2434.3 \frac{\text{m}}{\text{s}}$	$v_{ws} = 2434.3 \frac{\text{m}}{\text{s}}$	$v_{ws} = 2434.3 \frac{\text{m}}{\text{s}}$
$k_{1l} = 3.726 \cdot 10^{-4} \frac{1}{\text{m}}$	$k_{2l} = 7.451 \cdot 10^{-4} \frac{1}{\text{m}}$	$k_{3l} = 3.726 \cdot 10^{-3} \frac{1}{\text{m}}$
$k_{1s} = 6.453 \cdot 10^{-4} \frac{1}{\text{m}}$	$k_{2s} = 7.451 \cdot 10^{-4} \frac{1}{\text{m}}$	$k_{3s} = 6.453 \cdot 10^{-3} \frac{1}{\text{m}}$
$A_1 = 320\text{m}^2$	$A_2 = 240\text{m}^2$	$A_3 = 160\text{m}^2$

Table 4.3: Waves paramters we used on the simulations. The indices l and s refer to the longitudinal and shear waves, respectively.

4.2.2.3 Description of the COMSOL code

The analysis described in this work was conducted using COMSOL, a multiphysics finite element software; by means this software we were able to carry out a more refined analysis with respect that one in [67]. The model has 30456 degrees of freedom and 3690 triangular elements, into which it has been divided. The size of the elements varies depending on the area of the model: it is reduced near the boundary sharing two subregion with different stiffnesses. The used shape functions are Lagrangian of quadratic order. The implicit methods are more complicated than the explicit ones, in which it is possible to find the solution at the next step by means the only that at the current step, because it is necessary to solve an equation for each time step that depend for both the states of the system (the current one and the next one). So, mathematically, if $s(t)$ is the state of the system at the current time t and $s(t+\Delta t)$ is the state of the system at the later instant $t+\Delta t$, one has:

$$\begin{aligned} s(t+\Delta t) &= F\left(s(t)\right) && \text{for the explicit methods} \\ H\left(s(t), s(t+\Delta t)\right) &= 0 && \text{for the implicit methods} \end{aligned} \tag{4.44}$$

The solver we used for calculate the results is based on the implicit method called *generalized-*α method. Those methods are similar to the second-order BDF (backward differentiation formulas) solver, also based on an implicit method. Unlike this latter method, the generalized-α is a method that allows to control better the degree of damping of high frequencies in the solution and it is more accurate. So that if a solution with sharp gradients is expected, one does not get a very smooth solution due to the damping in the backward method. It is worth to note that, for those same reasons it is also less stable. We used a dynamic load characterised by a discrete spectrum and a time step $t = (800Hz)^{-1}$.

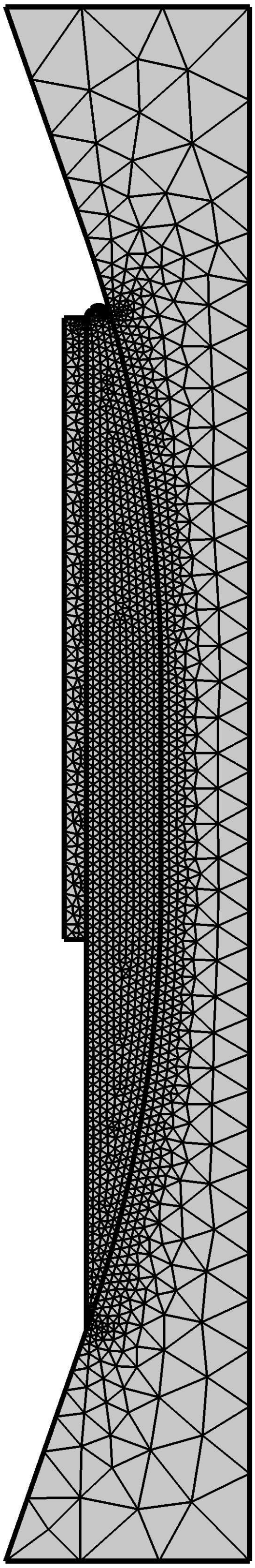

Figure 4.15: Triangular finite elements

4.2.3 Analysis of results

In this section the comparison between the deformation and the kinetic energy fields and the horizontal and vertical components of the acceleration vector, for the linear and non-linear cases, is shown to emphasyse how the non-linear contribution should be taken into consideration when a seismic analysis is carried out. As it is shown in the following subsections the differences, in suitable relative terms, are very large. In the following the superscript nl indicates that the corresponding quantity is calculated with the non-linear finite strain tensor $\mathbb{G}$, the third quantity in (4.7) and with the general non-linear evolution equations. Moreover, the superscript l indicates that the corresponding quantity is calculated with the linearised version of the strain tensor: i.e. (4.16) and with the linearised evolution equations. Hence, the deformation energies for non-linear and linear cases are denoted as follows,

$$\mathcal{W}^{nl} \qquad \text{for the non-linear case} \tag{4.45}$$

$$\mathcal{W}^{l} \qquad \text{for the linear case} \tag{4.46}$$

In the same way, the kinetic energies for non-linear and linear cases are denoted as follows,

$$\mathcal{K}^{nl} \qquad \text{for the non-linear case} \tag{4.47}$$

$$\mathcal{K}^{l} \qquad \text{for the linear case} \tag{4.48}$$

Hence, the relative non-linear/linear energies are calculated in the following way:

$$\tilde{\mathcal{W}} = \frac{\mathcal{W}^{nl} - \mathcal{W}^{l}}{\bar{\mathcal{W}}^{nl}} \tag{4.49}$$

$$\tilde{\mathcal{K}} = \frac{\mathcal{K}^{nl} - \mathcal{K}^{l}}{\bar{\mathcal{K}}^{nl}} \tag{4.50}$$

where the symbols $\bar{\mathcal{W}}^{nl}$ and $\bar{\mathcal{K}}^{nl}$ represent the average, on the domain, of the non-linear deformation and kinetic energy respectively. The accelerations (and their difference between the non-linear and linear case) are normalized by the gravity acceleration g. Taking into account that the displacements are denoted as u_i for the linear case and as v_i for the non-linear case, the horizontal and vertical accelerations for each point for the linear and for the non-linear cases are denoted, respectively, as follows,

$$\tilde{\ddot{u}}_i = \frac{\ddot{u}_i}{g} \qquad \text{for the linear case} \tag{4.51}$$

$$\tilde{\ddot{v}}_i = \frac{\ddot{v}_i}{g} \qquad \text{for the non-linear case} \tag{4.52}$$

and the comparison has been obtained by the difference:

$$\tilde{a}_i = \tilde{\ddot{v}}_i - \tilde{\ddot{u}}_i \tag{4.53}$$

Clearly the index i takes on values equal to 1 (horizontal acceleration) or 2 (vertical acceleration).

4.2.3.1 Comparison of the deformation energy fields in linear and non-linear cases and formation of energy difference boundary layers

The deformation energy represents an important measure of the deformations during the seismic action that it is worth to be investigated. In the Fig. 4.16, it is shown the highest (or lowest) amount of energy (4.49) reached on the domain for each time instant.

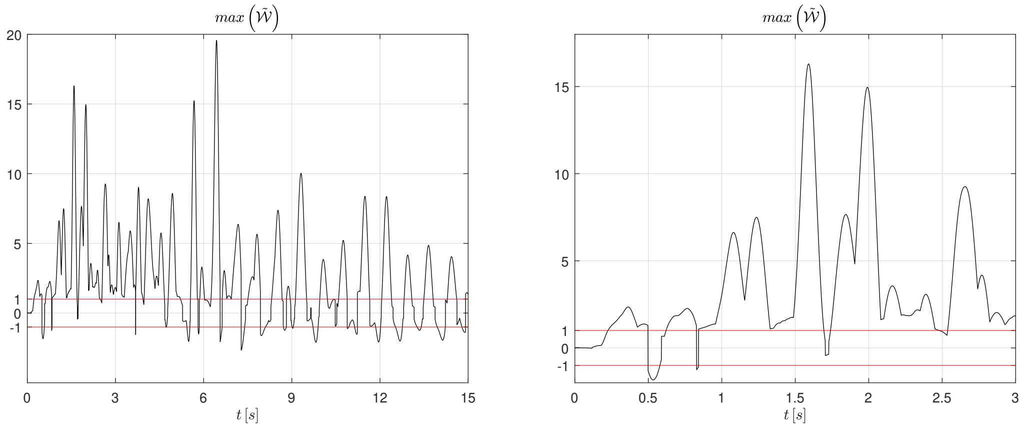

(a) (b)

Figure 4.16: Maximum value of $\tilde{\mathcal{W}}$, defined in (4.49), for (a)the whole analyses and (b) a zooming of the first 3 seconds

It is worth to notice that some extreme values are due clearly to numerical errors that are concentrated only in isolated elements. In Fig. 4.16 the lines corresponding to $y = \pm 1$ are highlighted to show how large are the relative errors between the two methods (clearly the value 1 means differences equal to 100%). Future numerical simulations, with more powerful computing tools, will eliminate these spurious values: we will use finer finite elements and some regularising techniques, as, for instance, the introduction of higher gradient models, which are more suitable to deal with the discontinuity of stiffnesses fields. To cut off the aforementioned numerical errors [193], in the following contour plots, the color legend is restricted to represent values within the range [-1, 1]. However, for some plots (e.g., Fig. 4.17-b), a different range might seem more appropriate. These choices were made to improve the readability of the plots when the actual range of values is too small to be effectively represented within the wider range [-1, 1]. The contour plots of the deformation energy in the non-linear case $\mathcal{W}^{nl}$ and its comparison $\tilde{\mathcal{W}}$ with respect the linear one are shown for some time instants in Fig. 4.17, 4.18, 4.19 and 4.20. In the Fig. 4.16-a (and clearer in Fig. 4.16-b) notice that, already during the first seconds when the seismic action excites the ground, the relative difference $\tilde{\mathcal{W}}$ is not negligible (having value much higher then 100%).

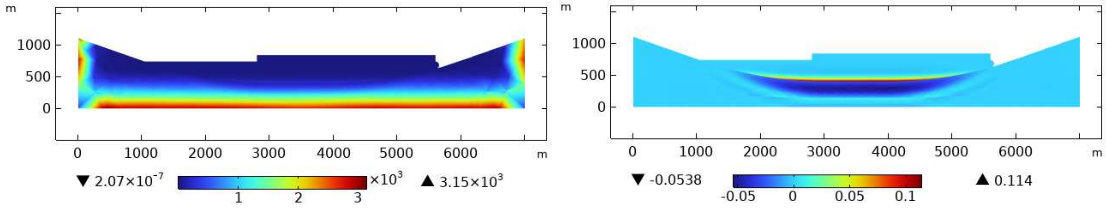

(a) Deformation energy $\mathcal{W}^{nl}$, (4.45) (b) Percentage difference $\tilde{\mathcal{W}}$, (4.49)

Figure 4.17: (a) Deformation energy $\mathcal{W}^{nl}$ (expressed in units Pa) and (b) percentage difference $\tilde{\mathcal{W}}$ of the deformation energies, between the non-linear and linear cases, at the instant $t = 0.15$s

Note that from the very beginning, the (albeit small) differences are concentrated at the material transition, from the bedrock to the softer intermediate layer. In addiction, the deformation energy (at the Fig. 4.17-a) appears almost uniform and it is the result of the composition of several spherical waves with different velocities and wave lengths.

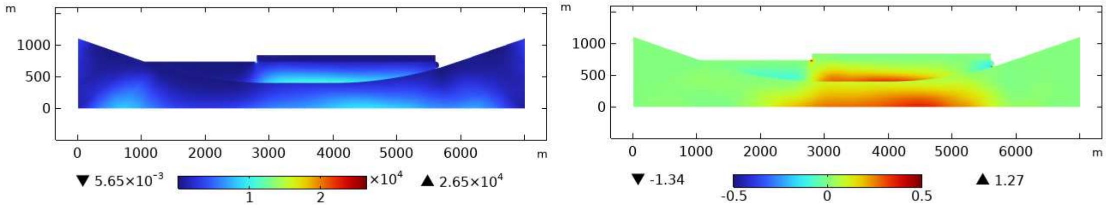

(a) Deformation energy $\mathcal{W}^{nl}$, (4.45) (b) Percentage difference $\tilde{\mathcal{W}}$, (4.49)

Figure 4.18: (a) Deformation energy $\mathcal{W}^{nl}$ (expressed in units Pa) and (b) percentage difference $\tilde{\mathcal{W}}$ of the deformation energies, between the non-linear and linear cases, at the instant $t = 0.5$s

It has to be observed that from the very outset of the simulation, the relative difference is substantial (Fig.4.18-b). However, while the extreme values (127% and -134%) in Fig. 4.18-b) may not be representative of any phenomenon as they are concentrated, each one, in a single element, the extensive region where the difference $\tilde{\mathcal{W}}$ exceeds 20% warrants attention.

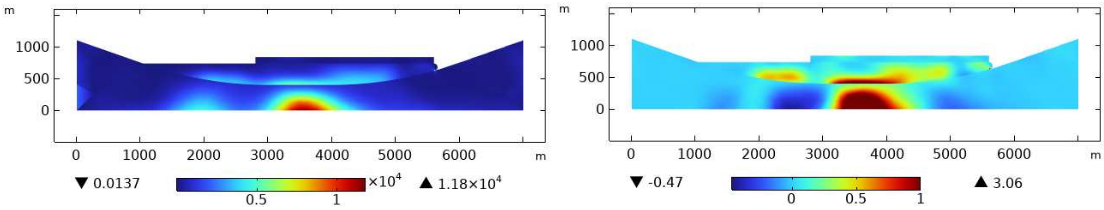

(a) Deformation energy $\mathcal{W}^{nl}$, (4.45)

(b) Percentage difference $\tilde{\mathcal{W}}$, (4.49)

Figure 4.19: (a) Deformation energy $\mathcal{W}^{nl}$ (expressed in units Pa) and (b) relative difference $\tilde{\mathcal{W}}$ of the deformation energies, between the non-linear and linear cases, at the instant $t = 1.5$s

Figure 4.19-b reveals significantly larger differences. Notably, even after excluding the extreme values, the energy relative difference exceeds 100% close to the boundary layer.

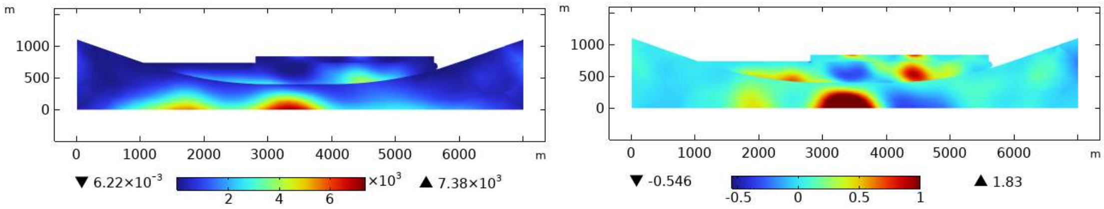

(a) Deformation energy $\mathcal{W}^{nl}$, (4.45)

(b) Relative difference $\tilde{\mathcal{W}}$, (4.49)

Figure 4.20: (a) Deformation energy $\mathcal{W}^{nl}$ (expressed in units Pa) and (b) relative difference $\tilde{\mathcal{W}}$ of the deformation energies, between the non-linear and linear cases, at the instant $t = 3$s

The whole evolution in time of the deformation energy $\mathcal{W}^{nl}$ (4.45) and its difference $\tilde{\mathcal{W}}$ with respect the linear case (4.49), is shown in a video, which is included in the form of supplementary materials.

4.2.3.2 Comparison of the kinetic energy fields in linear and non-linear cases and the formation of energy difference boundary layers

Kinetic energy fields serve as key indicators of velocities within a system under consideration and deserve thorough investigation. Following Sec. 4.2.3.1, it is shown the highest (or lowest) value of the difference of the kinetic energy, denoted by $\tilde{\mathcal{K}}$ (defined in (4.50)), reached in the domain for each instant of time. Then, the contour plots of both the kinetic energy $\mathcal{K}^{nl}$ calculated with our non-linear model and the difference $\tilde{\mathcal{K}}$ are presented in 4.22, 4.23, 4.24, 4.25, 4.26 and 4.27.

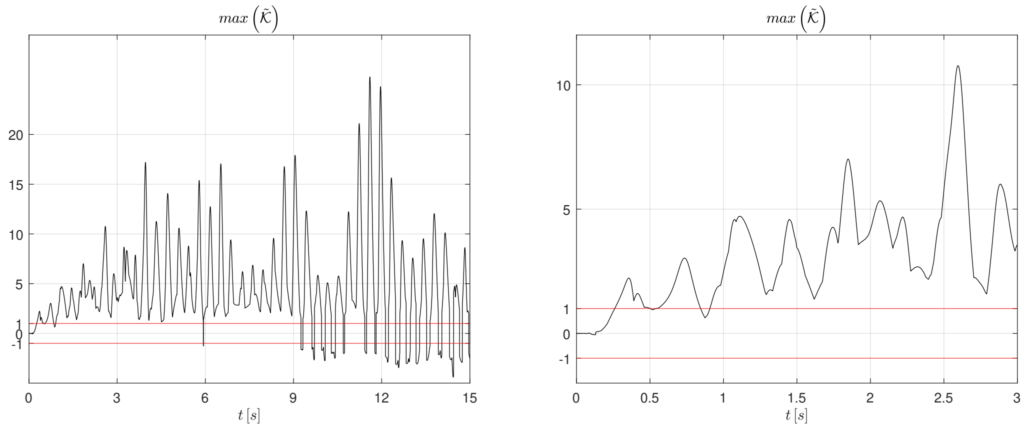

(a)

(b)

Figure 4.21: Maximum value of differences $\tilde{\mathcal{K}}$ with respect the time between the two cases (linear and non-linear) for (a) the whole time interval of the performed analyses and (b) a zooming of the first 3 seconds

It can be seen how the two considered models, that is linear and non-linear, give us a remarkable difference near the boundary (Fig. 4.22) where there is the transition from an harder layer to a softer one, i.e. where the strong material inhomogeneity occurs. It is worth noting that, just as in the Sec. 4.2.3.1, also for the kinetic energy we focus on the first 3 seconds, i.e. in the time interval when the seismic waves acts on the domain. As one can see, the difference continues to be not negligible also after the third second.

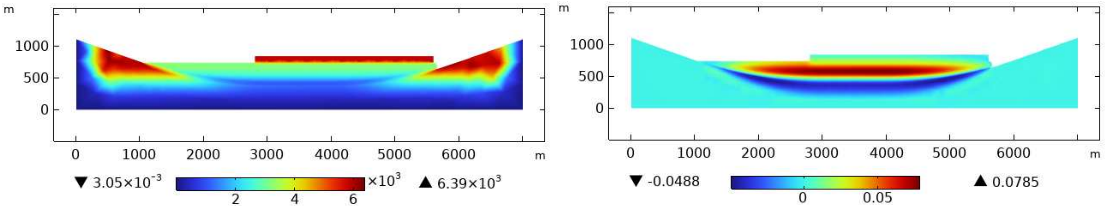

(a) Kinetic energy $\mathcal{K}^{nl}$, (4.47)

(b) Percentage difference $\tilde{\mathcal{K}}$, (4.50)

Figure 4.22: (a) Kinetic energy $\mathcal{K}^{nl}$ (expressed in units Pa) and (b) percentage difference $\tilde{\mathcal{K}}$ of the kinetic energies, between the non-linear and linear cases, at the instant $t = 0.15$s

Figures 4.22-b and 4.23-b reveal that the largest differences in kinetic energy are initially concentrated near the boundary between the bedrock and the softer layer. Subsequently, these differences propagate through the softer material towards the rigid top layer. Notably, even during the initial stages of ground excitation by the seismic action, the relative difference is substantial. For example, Figure 4.23-b shows that the difference between the non-linear and linear analyses can exceed 100

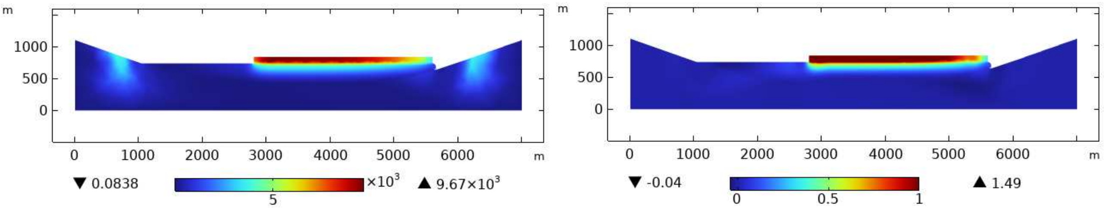

(a) Kinetic energy $\mathcal{K}^{nl}$, (4.47) (b) Relative difference $\tilde{\mathcal{K}}$, (4.50)

Figure 4.23: (a) Kinetic energy $\mathcal{K}^{nl}$ (expressed in units Pa) and (b) percentage difference $\tilde{\mathcal{K}}$ of the kinetic energies, between the non-linear and linear cases, at the instant $t = 0.3$s

During the first fractions of second, period in which the seismic wave acts on the considered propagation region (remember that the seismic action goes on for 3 s) the higher differences are concentrated at the top of the propagation region, and exactly where the stiffness changes and a material non-linearity is activated. The difference propagates from the harder layer, at the top, to the softer one and vice versa because the reflection of the seismic wave (Fig. 4.23-b and Fig. 4.24-b).

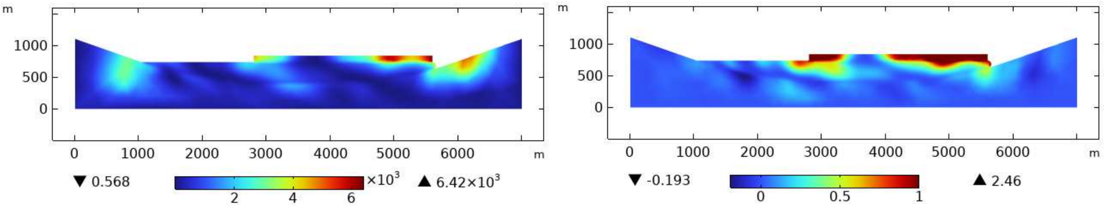

(a) Kinetic energy $\mathcal{K}^{nl}$, (4.47) (b) Percentage difference $\tilde{\mathcal{K}}$, (4.50)

Figure 4.24: (a) Kinetic energy $\mathcal{K}^{nl}$ (expressed in units Pa) and (b) relative difference $\tilde{\mathcal{K}}$ of the kinetic energies, between the non-linear and linear cases, at the instant $t = 1$s

During the seismic excitation big differences between linear and non-linear models are calculated. For example at $t = 2$ s (in Fig. 4.25) one can observe that the main differences are mostly concentrated in the top harder layer and its value increases noticeably reaching very relevant values as it is shown, for example, at the Fig. 4.25-b.

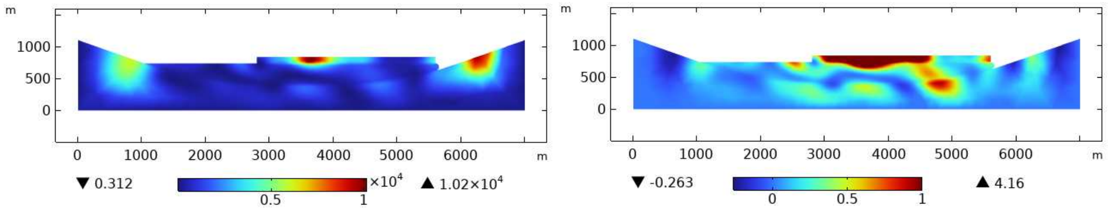

(a) Kinetic energy $\mathcal{K}^{nl}$, (4.47) (b) Percentage difference $\tilde{\mathcal{K}}$, (4.50)

Figure 4.25: (a) Kinetic energy $\mathcal{K}^{nl}$ (expressed in units Pa) and (b) relative difference $\tilde{\mathcal{K}}$ of the kinetic energies, between the non-linear and linear cases, at the instant $t = 2$s

In Fig. 4.21-b a big peak of relative difference is clearly evident. In order to avoid to comment some values which may be simply due to numerical errors, the contour plot in the neighboring of that instant of time (specifically at $t = 2.6$ s), is shown in Fig. 4.26. At this instant the value of the difference is very high affecting. Moreover, on the harder top layer a region is clearly visible where the kinetic energy reaches a high value. This makes the difference $\tilde{\mathcal{K}}$ (see the Fig.4.26-b) absolutely non-negligible.

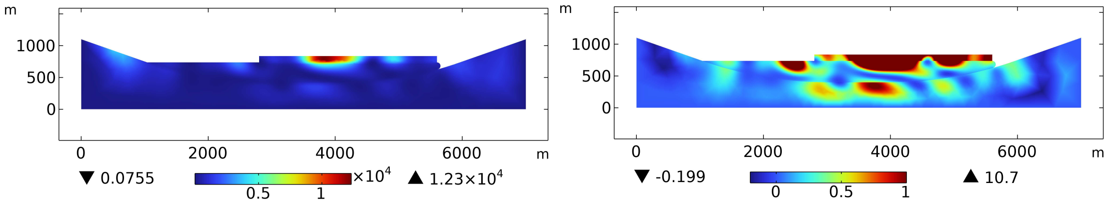

(a) Kinetic energy $\mathcal{K}^{nl}$, (4.47) (b) Percentage difference $\tilde{\mathcal{K}}$, (4.50)

Figure 4.26: (a) Kinetic energy $\mathcal{K}^{nl}$ (expressed in units Pa) and (b) relative difference $\tilde{\mathcal{K}}$ of the kinetic energies, between the non-linear and linear cases, at the instant $t = 2.6$s

Also after the instant $t = 3$ s (Fig. 4.27), when the seismic excitation ends, its effects continue to be observable for a long time interval, in the region where the wave propagation is studied. It is exactly after the instant $t = 3$ that the differences between the predictions of non-linear and linear models increase considerably as it is shown by the Fig. 4.21. This implies that the kinetic energy (and therefore the velocities of each material point) calculated by means of a linear model does not seem to give reliable predictions. It is clear that such differences cannot be overlooked and that more careful modelling assumptions are required.

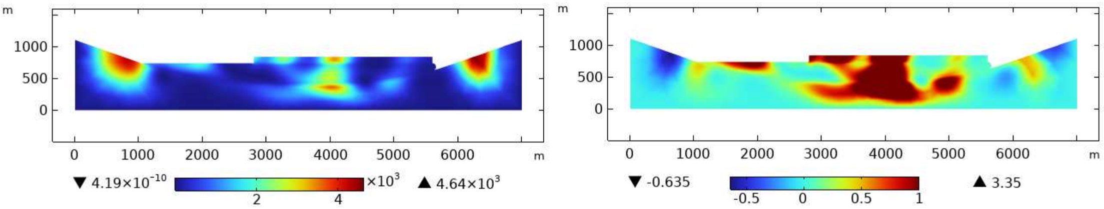

(a) Kinetic energy $\mathcal{K}^{nl}$, (4.47) (b) Relative difference $\tilde{\mathcal{K}}$, (4.50)

Figure 4.27: (a) Kinetic energy $\mathcal{K}^{nl}$ (expressed in units Pa) and (b) Relative difference $\tilde{\mathcal{K}}$ of the kinetic energies, between the non-linear and linear cases, at the instant $t = 3$s

The whole evolution in time of the kinetic energy $\mathcal{K}^{nl}$ (4.47) and its relative difference $\tilde{\mathcal{K}}$ with respect to the kinetic energy calculated using the linear model (4.50), is shown with a video included in the form of supplementary materials.

4.2.3.3 Comparison of acceleration fields

The accelerations (4.51) and (4.52) (either horizontal and vertical) in certain points have been calculated and their differences (4.53) (between the non-linear and linear models) are seen to be substantial. These results must determine a chenge in the used approaches used to predict seismic phenomena. The Fig. 4.28 shows the points which we have chosen, on the basis of the evidence gathered in [67], in order to compare the predictions of linear and non-linear models: recall that the accelerations difference used for getting the presented comparisons is defined in (4.53).

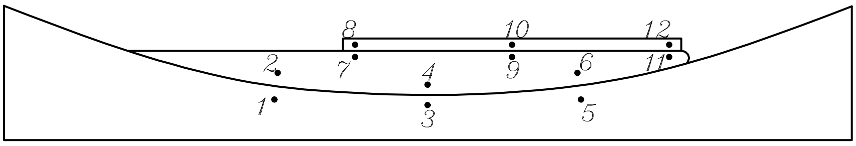

Figure 4.28: Analyzed points

The first 6 point are chosen near the boundary between the bedrock layer and the softer one, while the next 6 ones are taken close to the boundary between the softer and the top rigid layer. Either the horizontal and vertical accelerations ($\tilde{\ddot{u}}_i$ and $\tilde{\ddot{v}}_i$ respectively for the linear and non-linear cases) and the difference $\tilde{a}_i$ (calculated as in (4.51), (4.52) and (4.53)) are plotted in Fig. 4.29, 4.30, 4.31, 4.32, 4.33, 4.34, 4.35, 4.36, 4.37, 4.38, 4.39 and 4.40 for all the points defined in Fig. 4.28. The figures below (namely 4.29, 4.30, 4.31, 4.32, 4.33, 4.34, 4.35, 4.36, 4.37, 4.38, 4.39 and 4.40) are structured with the following scheme:

- on the left hand side the evolution in time of the accelerations, defined as in (4.51) and (4.52) and scaled by the gravity acceleration g, of the considered point (for the linear $\tilde{\ddot{u}}_i$ and non-linear $\tilde{\ddot{v}}_i$ case) are shown for each direction (i.e. for $i = 1, 2$).

- on the right hand side the differences $\tilde{a}_i$, denoted as in (4.53), are shown. Notably, these differences are plotted as a fraction of the gravitational acceleration g.

In the Fig. 4.29, 4.30, 4.31, 4.32, 4.33 and 4.34 the accelerations of the points close to the boundary between the bedrock and the softer layer are shown.

Point 1

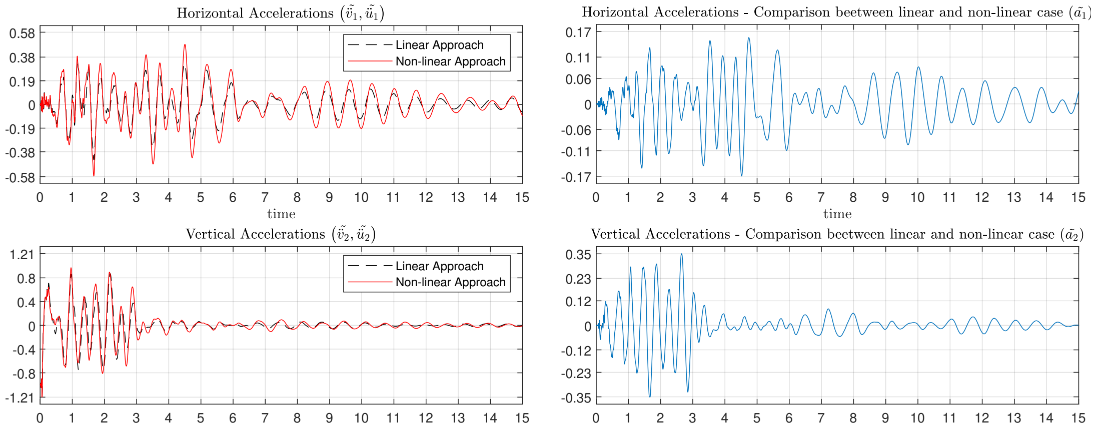

Figure 4.29: Comparison of the horizontal and vertical accelerations, between the non-linear $\tilde{\ddot{v}}_i$ and linear $\tilde{\ddot{u}}_i$ cases (pictures on the left) and their differences $\tilde{a}_i$ (pictures on the right), gotten by the (4.51), (4.52) and (4.53) for the Point 1

In the Fig. 4.29 and 4.30 the first couple of points is considered (Point 1 and Point 2). Although, for this couple of points, the differences $\tilde{a}_i$ in (4.53) do not reach their highest values, they are also higher then $0.2g$ that means an approximative difference of $2\frac{\mathrm{m}}{\mathrm{s}^2}$.

Point 2

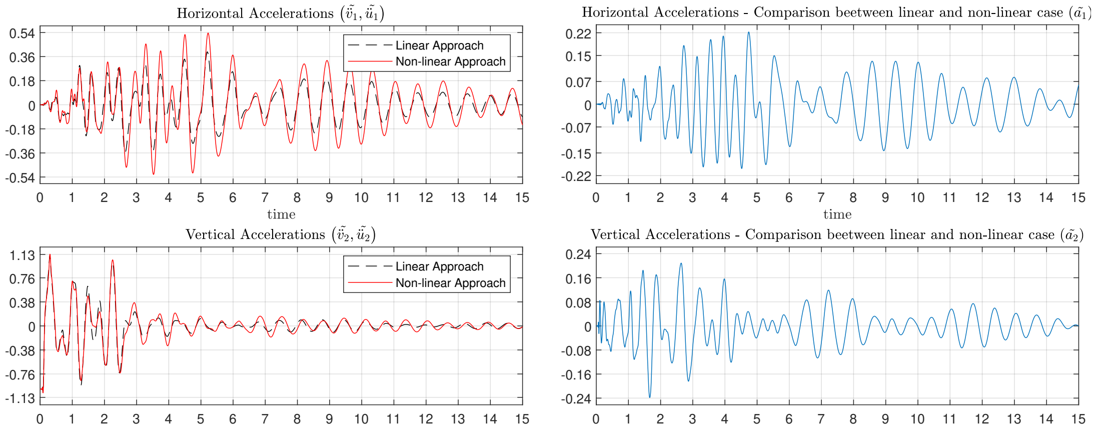

Figure 4.30: Comparison of the horizontal and vertical accelerations, between the non-linear $\tilde{\ddot{v}}_i$ and linear $\tilde{\ddot{u}}_i$ case, (pictures on the left) and their differences $\tilde{a}_i$ (picture on the right) gotten by the (4.51), (4.52) and (4.53) for the Point 2

Analyzing the couple of point that follows (i.e. Point 3 (Fig. 4.31) and 4 (Fig. 4.32)) the difference increases a lot (see the differences of the vertical accelerations), reaching the important value of about $0.7g$. Those clearly are quantities that must warn the modellers and all those whose decisions depend on their predictions.

Point 3

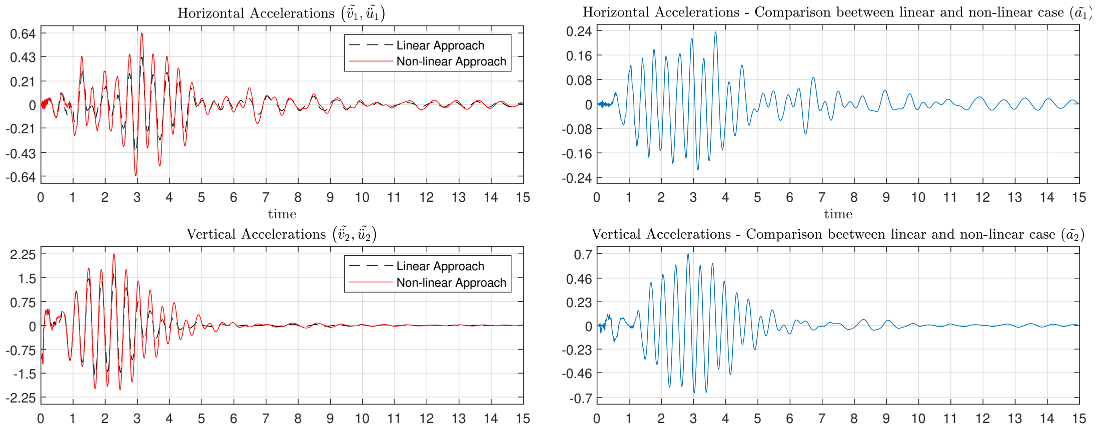

Figure 4.31: Comparison of the horizontal and vertical accelerations, between the non-linear $\tilde{\ddot{v}}_i$ and linear $\tilde{\ddot{u}}_i$ case, (pictures on the left) and their differences $\tilde{a}_i$ (picture on the right) gotten by the (4.51), (4.52) and (4.53) for the Point 3

Point 4

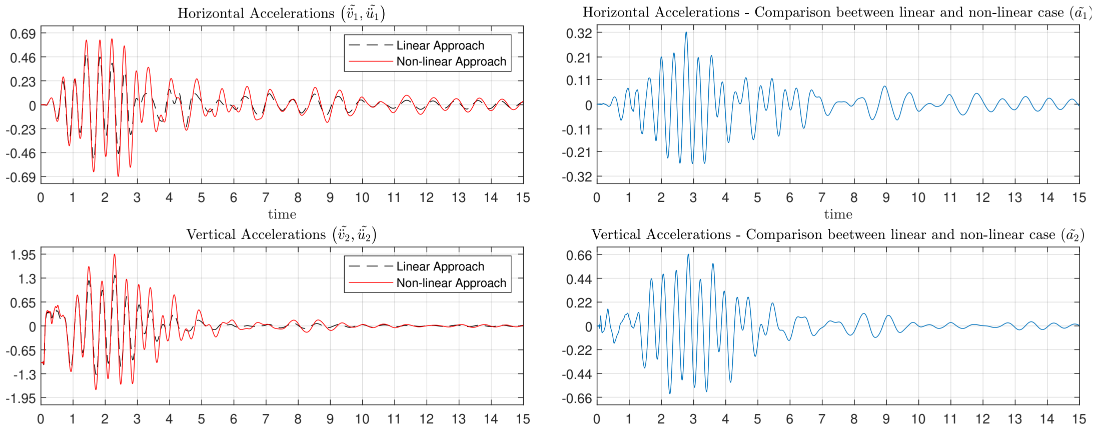

Figure 4.32: Comparison of the horizontal and vertical accelerations, between the non-linear $\tilde{\ddot{v}}_i$ and linear $\tilde{\ddot{u}}_i$ case, (pictures on the left) and their differences $\tilde{a}_i$ (picture on the right) gotten by the (4.51), (4.52) and (4.53) for the Point 4

Point 5

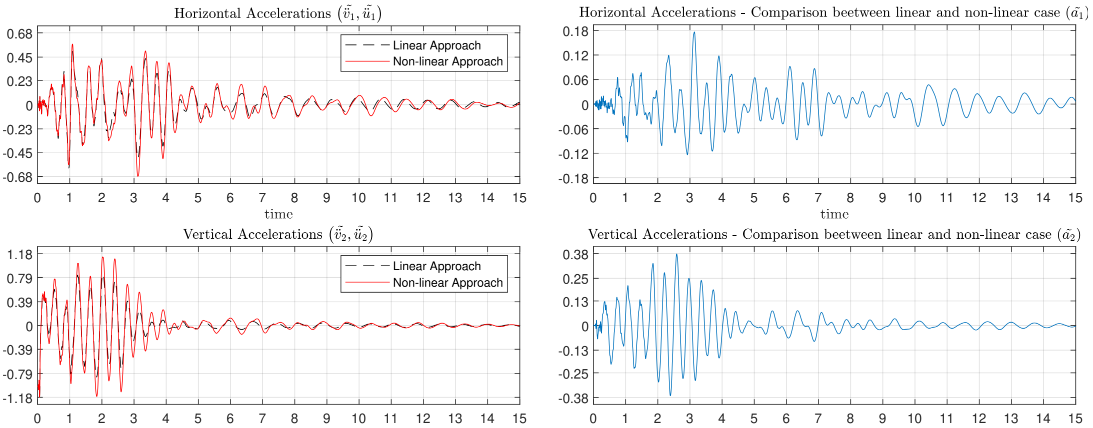

Figure 4.33: Comparison of the horizontal and vertical accelerations, between the non-linear $\tilde{\ddot{v}}_i$ and linear $\tilde{\ddot{u}}_i$ case, (pictures on the left) and their differences $\tilde{a}_i$ (picture on the right) gotten by the (4.51), (4.52) and (4.53) for the Point 5

Point 6

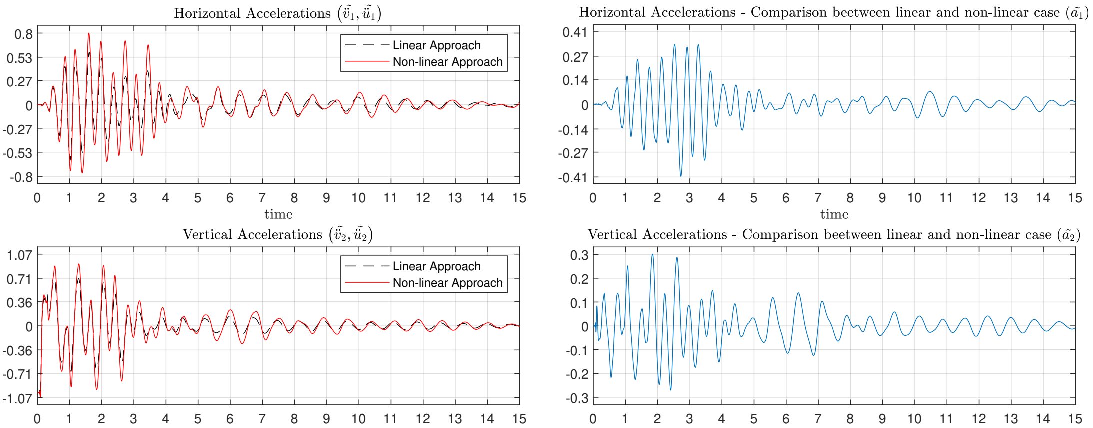

Figure 4.34: Comparison of the horizontal and vertical accelerations, between the non-linear $\tilde{\ddot{v}}_i$ and linear $\tilde{\ddot{u}}_i$ case, (pictures on the left) and their differences $\tilde{a}_i$ (picture on the right) gotten by the (4.51), (4.52) and (4.53) for the Point 6

At the upper boundary, between the softer layer and the harder block, on which the downtown of L'Aquila is located, the values of the differences continue to be very high, having values higher than 20% of g and, in same case, reaching error around 70% of g (as in the Fig. 4.38 and 4.40). In the following figures these strongly high values of the errors are shown.

Point 7

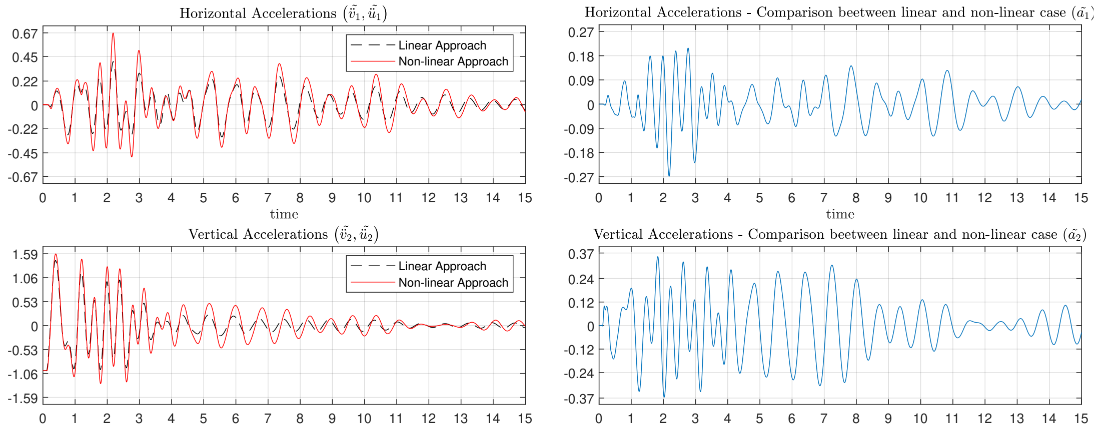

Figure 4.35: Comparison of the horizontal and vertical accelerations, between the non-linear $\tilde{\ddot{v}}_i$ and linear $\tilde{\ddot{u}}_i$ case, (pictures on the left) and their differences $\tilde{a}_i$ (picture on the right) gotten by the (4.51), (4.52) and (4.53) for the Point 7

Point 8

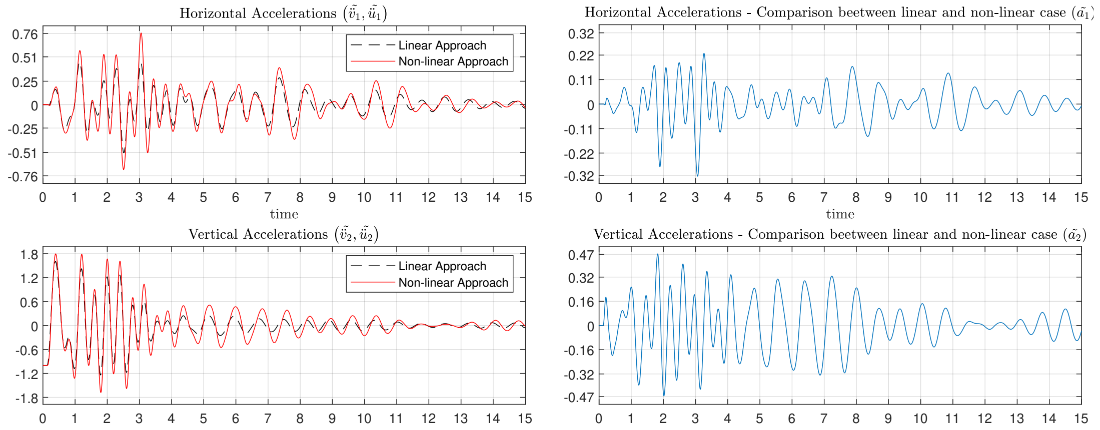

Figure 4.36: Comparison of the horizontal and vertical accelerations, ween the non-linear $\tilde{\ddot{v}}_i$ and linear $\tilde{\ddot{u}}_i$ case, (pictures on the left) and their differences $\tilde{a}_i$ (picture on the right) gotten by the (4.51), (4.52) and (4.53) for the Point 8

Point 9

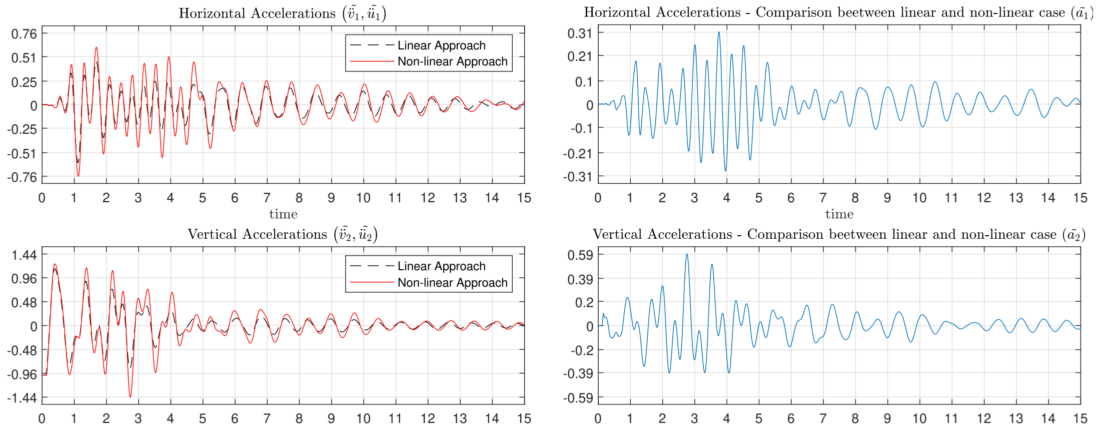
Horizontal Accelerations $(\tilde{\ddot{v}}_1, \tilde{\ddot{u}}_1)$

Horizontal Accelerations - Comparison beetween linear and non-linear case $(\tilde{a}_1)$

Vertical Accelerations $(\tilde{\ddot{v}}_2, \tilde{\ddot{u}}_2)$

Vertical Accelerations - Comparison beetween linear and non-linear case $(\tilde{a}_2)$

Figure 4.37: Comparison of the horizontal and vertical accelerations, between the non-linear $\tilde{\ddot{v}}_i$ and linear $\tilde{\ddot{u}}_i$ case, (pictures on the left) and their differences $\tilde{a}_i$ (picture on the right) gotten by the (4.51), (4.52) and (4.53) for the Point 9

Point 10

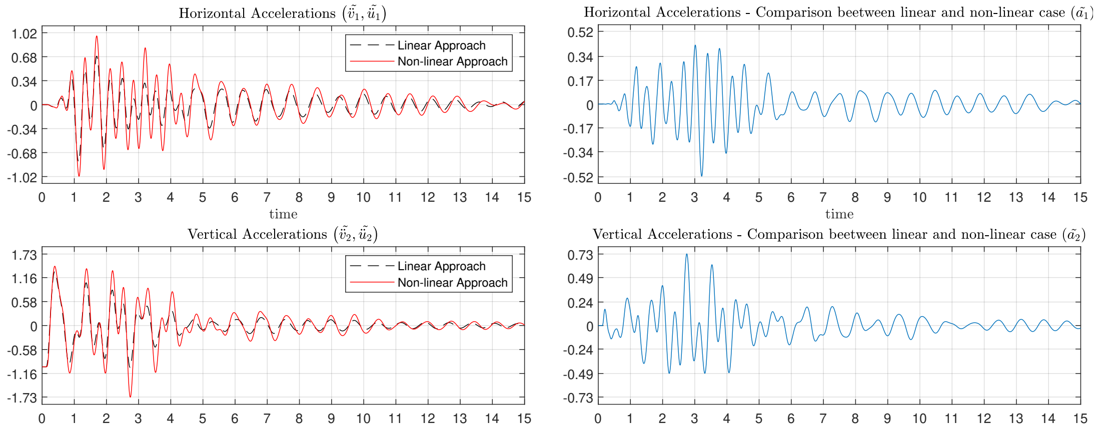
Horizontal Accelerations $(\tilde{\ddot{v}}_1, \tilde{\ddot{u}}_1)$

Horizontal Accelerations - Comparison beetween linear and non-linear case $(\tilde{a}_1)$

Vertical Accelerations $(\tilde{\ddot{v}}_2, \tilde{\ddot{u}}_2)$

Vertical Accelerations - Comparison beetween linear and non-linear case $(\tilde{a}_2)$

Figure 4.38: Comparison of the horizontal and vertical accelerations, between the non-linear $\tilde{\ddot{v}}_i$ and linear $\tilde{\ddot{u}}_i$ case, (pictures on the left) and their differences $\tilde{a}_i$ (picture on the right) gotten by the (4.51), (4.52) and (4.53) for the Point 10

Point 11

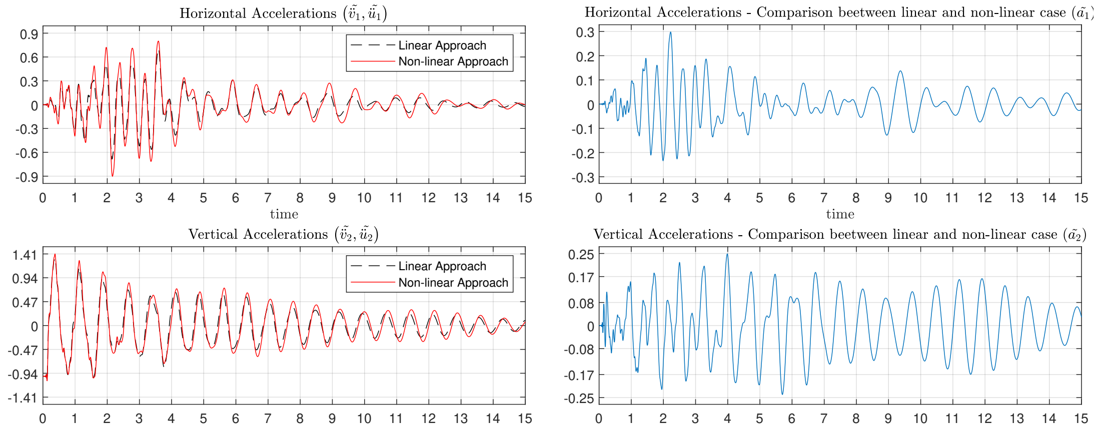

Figure 4.39: Comparison of the horizontal and vertical accelerations, between the non-linear $\ddot{\tilde{v}}_i$ and linear $\ddot{\tilde{u}}_i$ case, (pictures on the left) and their differences $\tilde{a}_i$ (picture on the right) gotten by the (4.51), (4.52) and (4.53) for the Point 11

Point 12

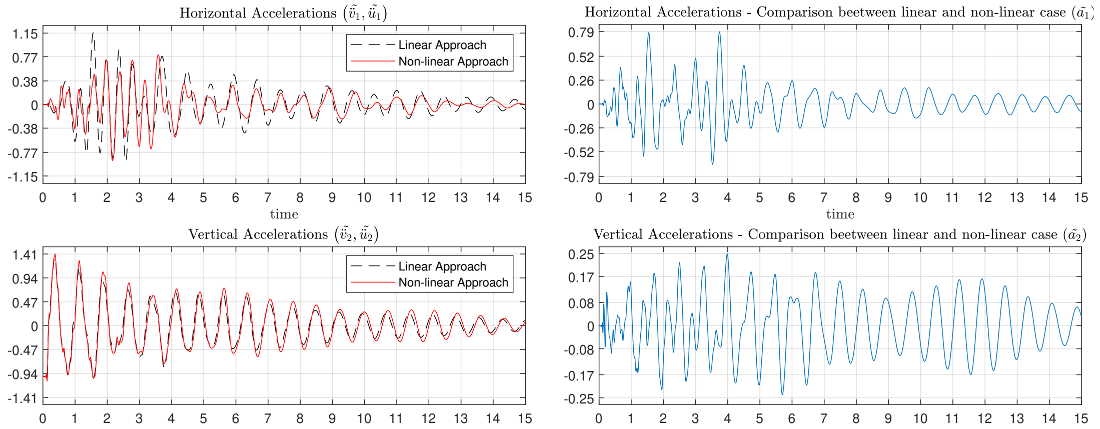

Figure 4.40: Comparison of the horizontal and vertical accelerations, between the non-linear $\ddot{\tilde{v}}_i$ and linear $\ddot{\tilde{u}}_i$ case, (pictures on the left) and their differences $\tilde{a}_i$ (picture on the right) gotten by the (4.51), (4.52) and (4.53) for the Point 12

The observed substantial discrepancies in the acceleration field impose a paradigm change in the choices to be accepted when modelling seismic wave propagation. The non-linear phenomena require a careful consideration due to their proven potential for significant impact. This emphasis is particularly relevant in the light of the findings presented in this work: moreover, by now, modern theoretical and numerical tools allow for the development of predictive analyses based on sophisticated non-linear models.

4.2.4 Final discussions

Having obtained the prediction for seismic accelerations one can calculate, by means of the fast Fourier transform (using a strong smoothing in order to avoid the peaks generated by numerical errors), the spectrum ratios between the horizontal and vertical accelerations spectrum of some specifically chosen points in the considered region (Point 8 and Point 12 in Fig. 4.28) and the horizontal and vertical accelerations spectrum of a reference point (Point 1 in Fig. 4.28); The chosen reference point for spectral ratios is the Point 1 because it stays into the bedrock. These plots are shown at the Fig.s 4.42 and 4.43. Then these ratios have been compared with the Fig. 4.41 that shows the Fig. 10 (reproduced here without any change) from [67]. In particular the comparison is carried out with the Fig. 10-a (for the Point 8 in Fig. 4.42) and the Fig. 10-b (for the Point 12 in Fig. 4.43). The station named *AQPK* in Fig. 4.41 is located not far from the Point 8 whereas the station named *GDIF* in Fig. 4.41 is located not far from the Point 12.

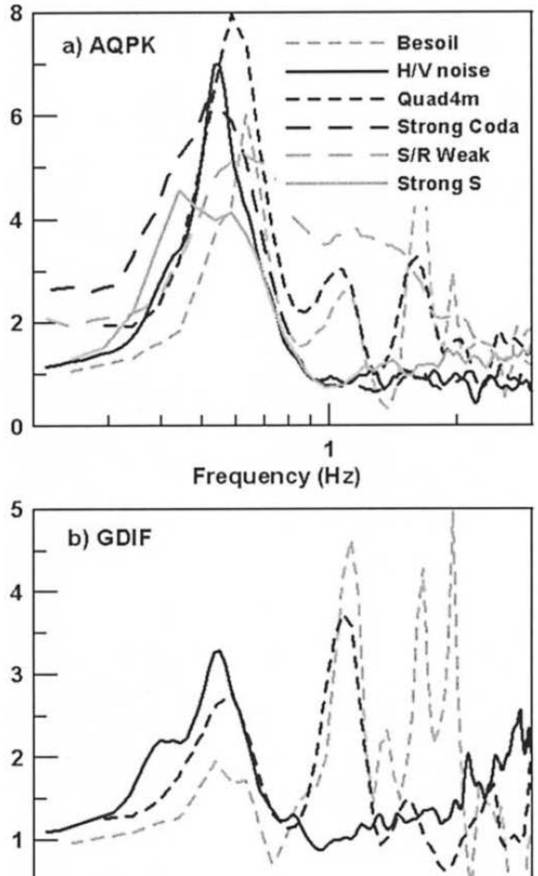

Figure 4.41: Fig. 10 from [67] (figure and caption are not modified): *"(a) QUAD4M and BESOIL solutions compared with H/V applied to strong-motion and microtremor data and S/R applied to weak-motion data at the AQPK site. (b) QUAD4M and BESOIL solutions compared with H/V applied to microtremor data at the GDIF site. The line symbol are the same in both (a) and (b)"*

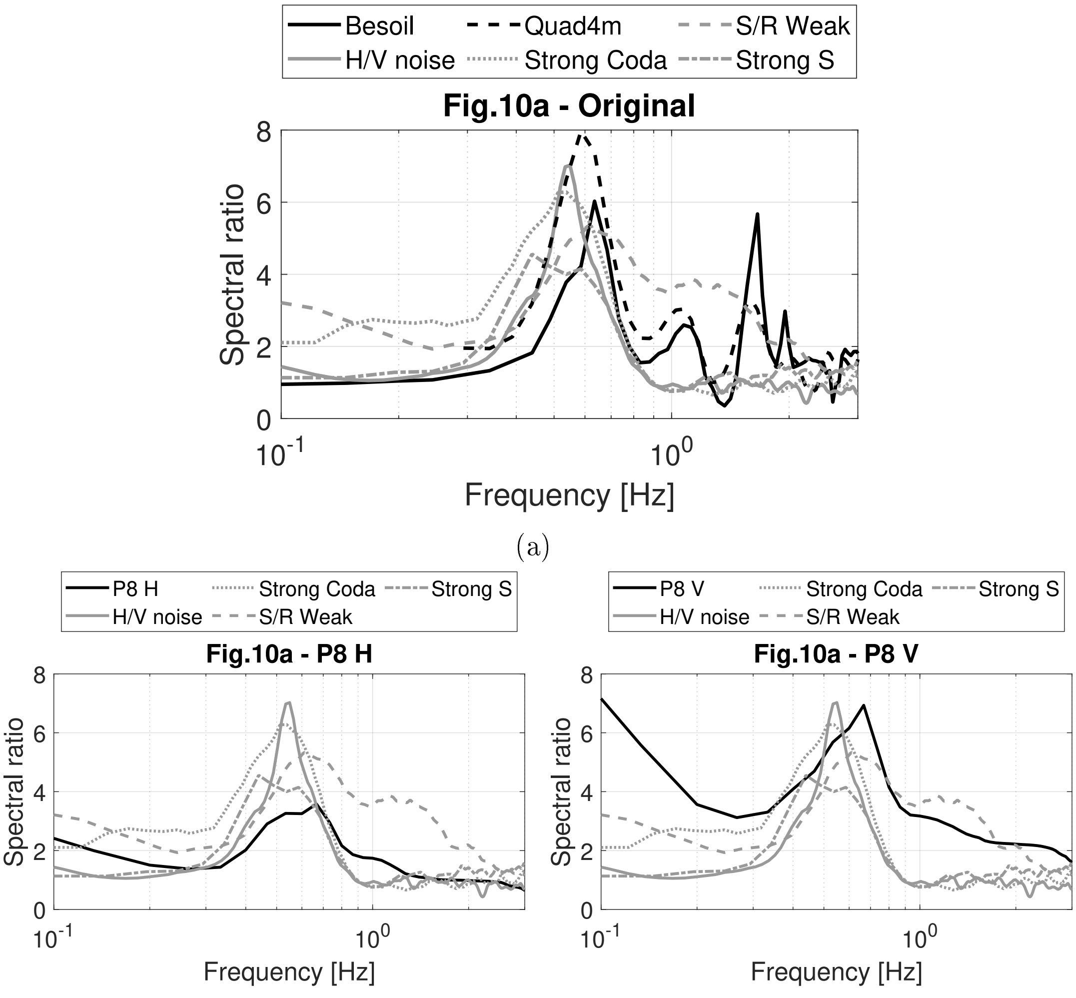

(a)

(b)

(c)

Figure 4.42: The spectral ratio between the horizontal (a) and vertical (b) non-linear accelerations of the Point 8 and the Point 1 (that is situated into the bedrock, see Fig. 4.28) compared with the Fig. 10-a from [67]. The spectral are smoothed with a 50 points moving window.

Comparing the Fig. 4.42 with the Fig. 10-a in [67] it is clear that the non-linear analysis fits better with the experimental data than the linear analysis. In fact, non-linear analysis removes the non-experimentally-observed peaks in the frequency range higher than 1Hz that were found in [67], which used the linear codes *Besoil* and *Quad4m*. The non-linear approach naturally cuts off these peaks. Future analysis will detail the reasons for which this qualitative property of non-linear models holds and will give stronger motivations for the use of spectral ratios to validate continuum models for the "seismic wave propagation" zone studied in the present paper.

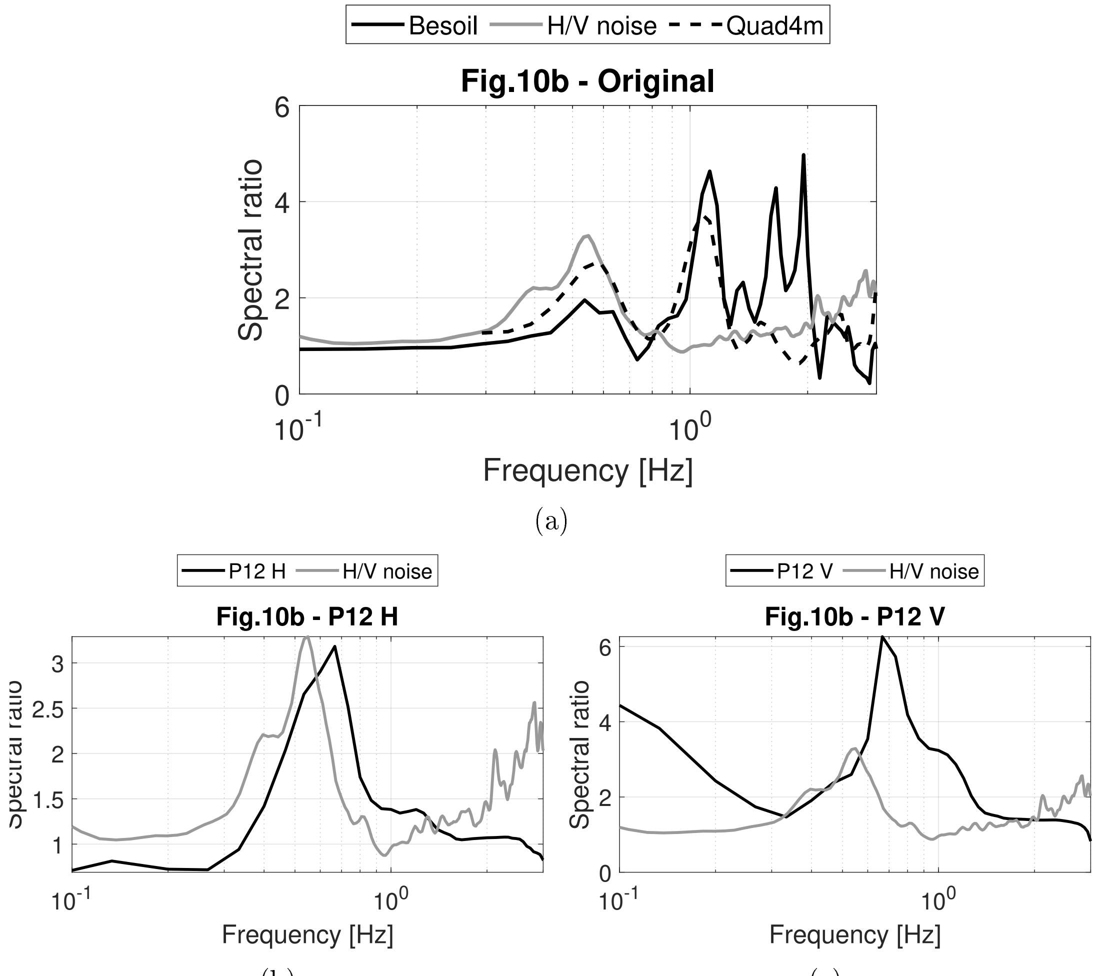

(a)

(b)

(c)

Figure 4.43: The spectral ratio between the horizontal (a) and vertical (b) non-linear accelerations of the Point 12 and the Point 1 (that is situated into the bedrock, see Fig. 4.28) compared with the Fig. 10-b from [67]. The spectral are smoothed with a 50 points moving window.

Future investigations will need to refine the just mentioned analysis, by introducing a careful and more realistic 3D modelling, developing appropriate numerical method for non-linear system [183, 184], enlarging the region where wave propagation is studied, in order to include the sites where other accelerometer stations of National Survey Network of Civil Protection were localised. These stations have been active since the middle of 90ties and have recorded a large number of earthquakes having different magnitude and hypocenters.

Chapter 5

Conclusion

Timoshenko Beam

In the above proposed formulation the evolution of the diffusion of the aging fluid, of damage and the mechanical behavior are described by the energy functional in (2.2) and by the hemivariational principle. Specifically, using the considered hemivariational principle, it was possible to include damage as a monotonically increasing function, that goes from 0 (non damaged case) to 1 (complete failure), which causes the stiffnesses to fall as shown in the Section 2.5. By means of the term $K_{c\omega}$, which appear in the last row of the (2.2), the damage and the diffusion of the fluid are coupled; in this way the spreading of the fluid into the beam causes increasing of the damage and it contributes to the progress to failure. In the Section 2.5.3 the role of the diffusity term K_{DIF} is shown. The diffusivity represents a parameter of the material that influences the spread, and the spread rate, of the fluid within the beam. The fluid distributes along the beam and it is not localized in a small area inducing the decrease of the rate of damage and delaying the failure of the structure. Clearly, as shown in the Section 2.5.4, the damage is affected not only by the changes of K_{DIF} but also by small changes of the coupling term $K_{c\omega}$. Increasing $K_{c\omega}$ (decrease in the value of its modulus), the failure of the structure is delayed. The work presented here is a preliminary step which in the future will be used to develop the hemivariational method for the study of a 2-D case [168]. It will also take into account the granular micromechanics approach [12, 163, 210] so as to properly analyze the material of which the dam is composed, e.g. the concrete. Another future purpose will be to carry out experimental tests in order to obtain more reasonable values of the parameters K_{DIF}, $K_{c\omega}$ and K_F and, then, establish a more realistic distribution of b_c^{ext}. It is worth to notice that the study of the diffusion of an aging agent whithin an human made construct is not limited at the case of the dams. That formulation can have several different fields of application, for example all those problems that involve diffusion in pores material [104]. It could help, for example, in the monitoring and safeguarding of the objects of artistic-cultural heritage and having, for the future structures, more careful design that tend to protect the artifacts from the diffusion of slag [111, 208] or pollutants that are abundant nowadays in our cities.

2-D case

Several approaches have been used in litterature in order to study the diffusion of ions into a body as in [93, 94]. In the above proposed formulation the evolution of the diffusion of the aging fluid, of damage and the mechanical behavior are described by the energy functional in (2.2) and by the hemivariational principle. Specifically, using the considered hemivariational principle, it was possible to include damage as a monotonically increasing function, that goes from 0 (non damaged case) to 1 (complete failure), which causes the stiffnesses to fall as shown in the Section 3.5. The second gradient terms contribution is been taken into account. This contribution enriches either the energy functional and the Karush-Kuhn-Tucker condiction, allowing a more refined model (like the model investigate in [188] for the 1-D case). By means of the term $K_{c\omega}$, which appear in the last row of the (2.2), the damage and the diffusion of the fluid (within the body $\mathcal{B}$) are coupled; in this way the spreading of the fluid into the structure causes increasing of the damage and it contributes to the progress to failure. In the Sections 3.5.1.1, 3.5.1.2, 3.5.2.1 and 3.5.2.2 the role of the diffusity terms K^{DIFF} and the coupling term $K_{c\omega}$ are shown. The diffusivity, in particular, represents a parameter of the material that influences the spreading (and the spread rate) of the fluid within the body. As shown in this paper, the damage is affected not only by the changes of K^{DIFF} but also by small changes of the coupling term $K_{c\omega}$. Increasing $K_{c\omega}$ (decrease in the value of its modulus), the failure of the structure is delayed. The work here presented is the following step of the monodimensional case and represents the developing of the hemivariational method used in [168]. A future goal will be to take into account this diffusion theory for the granular micromechanics approach [12, 163, 210] so as to properly analyze the material of which the dams are composed, e.g. the concrete. More specifically, the present work is part of a research project regarding the modeling of elastic, plastic and damaging phenomena in granular materials through hemivariational inequalities. This project started from thermomechanical analyses of granular interactions [141–144], before being reformulated through a hemivariational principle accounting for elastic, plastic and damaging phenomena [161, 168, 210]. This approach has been applied to many types of systems which can be modeled as having granular interactions at a local scale, such as reinforced concrete [176] or masonry structures [211–213], among others. It is worth to notice that the study of the diffusion of an aging agent whithin an human made construct is not limited at the case of the dams but it can find many application in each field of the civil engineering (for example the major infrastructures and geotechnical works). That formulation can have several different fields of application, for example all those problems that involve diffusion in pores material [104]. It could help, for example, in the monitoring and safeguarding of the objects of artistic-cultural heritage and having, for the future structures, more careful design that tend to protect the artifacts from the diffusion of slag [111, 208] or pollutants that are abundant nowadays in our cities. Another future purpose will be to carry out experimental tests in order to obtain more reasonable values of the parameters K^{DIFF}, $K_{c\omega}$ and K_F.

Apparent creep

The theory described in this thesis, used to model the aging phenomenon in concrete dams, allows for the simulation of increasing deformations under constant loads, a characteristic of creep behaviour. In Sec. 4.1, a specific type of creep, defined as *apparent* creep, has been demonstrated. By utilizing the aforementioned theory, which associates fluid diffusion within a body, a polymeric beam has been modelled. This beam undergoes increasing deformations under a constant load due to the diffusion of a fluid within its material. This case study proves the versatility of the theory presented in this thesis and the wide range of applications it enables. The interesting results shown in Sec. 4.1 provide a very accurate description of the phenomenon, opening up future perspectives for improving this model. In the future, the model could be refined by incorporating plasticity. Furthermore, experimental tests would allow for a better selection of parameters and provide a model capable of studying creep phenomena (in the strict sense) more thoroughly. This would enable the prediction of long-term mechanical responses for engineering structures subjected to this phenomenon, thus allowing for a better estimation of their deterioration through the study of damage evolution.

Earthquake

The results of the numerical simulations presented in this work demonstrate that the thesis on which we have based our investigation is correct: linear continuous models are not suitable to describe the effects at ground of large energy earthquakes (Magnitude larger than 6 Mw), in particular when the superficial crust is constituted by inhomogeneous materials. We therefore claim that it is worth considering non-linearities when conducting the analysis of seismic effects on structures and infrastructures. As it shown at the Section 4.2.3 large differences in the predicted values of deformations, velocities and accelerations are found when using linear or nonlinear models. Moreover, using the non-linear inhomogeneous model presented here we can predict where the highest values of accelerations must be expected, and therefore we believe to have supplied an important guide to future experimental and surveying activities. Moreover the supplied predictions could change the seismic hazard evaluation, to be incorporated in the design prescriptions. Aforementioned differences can make the linear seismic study useless, as not only the predicted values of most relevant quantities are quantitatively different, but also the qualitative features of predicted phenomena may differ drastically. Albeit a careful description of the phenomenology observed during the 2009 L'Aquila Earthquake requires a really drastic improvement of the model presented preliminarily here, we must observe that the simplistic nonlinear model we present, seems to fit much better than linear models all the available experimental evidence. In particular, we remark that with our 2D geometrically nonlinear isotropic model, in which stiffnesses are piecewise constant, we can predict more carefully, both quantitatively and qualitatively, some experimental evidence concerning the measured spectral ratios: while this subject will be carefully described in a future paper, in the present conclusion we will start reporting about preliminary, but very suggestive, results concerning these ratios (as shown in the Fig. 4.42 and Fig. 4.43). Some discrepancies of nonlinear models with experimental evidence are clearly caused by the chosen boundary conditions on the lateral sides of the region modelled for non-linear wave propagation. In fact, while at the bottom of this region the imposed displacement boundary conditions are realistic, those imposed at the lateral sides were chosen to render the numerical burden less heavy: this choice did reduce the predicted values of horizontal accelerations, exactly as expected. In the future development of the nonlinear model this limiting assumption will be removed. We expect that a predictive modelling for the seismic wave propagation in the Aterno River Valley must include novel and relevant material non-linearity assumptions, considered the proven expected high concentration of deformation energy at the discontinuity interfaces and the present knowledge about the mechanical properties of geo–materials. In fact, only by assuming the simplest geometric nonlinearity behaviour, exposed in this work at the Sec. 4.2.2 (particularly at the Sec. 4.2.2.1), one has shown the highlighted remarkable differences in the obtained predictions, when comparing them with those given by linear models. The results in Sec. 4.2.3.1, relating to the deformation energy, give us important informations about the evolution of the deformative state of the domain $\mathcal{B}$ for each case (either linear and non-linear) showing as the analysis by a nonlinear approach implies the possibility to describe relevant and expected phenomena. Also the results show in the Sec. 4.2.3.2 provides an idea of how much more realistic it is to approach the seismic problem with a non-linear modelling. Clearly, the most significative and impactful results for applications are those relating to the accelerations (Sec. 4.2.3.3). These results deserve close attention because high differences are visible and, even more importantly, it clearly shows that the linear approach, almost always, underestimates this quantity. A quantity is the acceleration that represent the most important parameter to consider not only during the study of seismic events but also in anti-seismic structural design. It has to be remarked that a relevant underestimation of experimentally observed accelerations, in the framework of linear theories, seems to have been already underlined in the literature (see EarthQuake Spectra in [67]).

Moreover in order to get a careful prediction of origins and onset of the seismic actions, from a geological and mechanical point of view, models of tectonic dynamic crack propagation must be considered, generalising and adapting the methods presented in [20, 95, 160, 167, 216]. In this way it will be possible to extend the regions where wave propagation is predicted, to include also hypocenters. We also expect that the presented results will allow for a more effective design for the new structures (and for the restoration of the damaged one) by exploiting the also knowledge and the conceptual tools which are already available and were used, e.g., in [136, 182, 185].

Bibliography

[1] B Emek Abali, Wolfgang H Müller, and Victor A Eremeyev. "Strain gradient elasticity with geometric nonlinearities and its computational evaluation". In: *Mechanics of Advanced Materials and Modern Processes* 1.1 (2015), pp. 1–11. ISSN: 2198-7874. DOI: `10.1186/s40759-015-0004-3`.

[2] Bilen Emek Abali and Emilio Barchiesi. "Additive manufacturing introduced substructure and computational determination of metamaterials parameters by means of the asymptotic homogenization". In: *Continuum Mechanics and Thermodynamics* 33.4 (2021), pp. 993–1009. DOI: `10.1007/s00161-020-00941-w`.

[3] Bilen Emek Abali, Andre Klunker, Emilio Barchiesi, and Luca Placidi. *A novel phase-field approach to brittle damage mechanics of gradient metamaterials combining action formalism and history variable.* 2021.

[4] Bilen Emek Abali, Andre Klunker, Emilio Barchiesi, and Luca Placidi. "A novel phase-field approach to brittle damage mechanics of gradient metamaterials combining action formalism and history variable". In: *ZAMM - Journal of Applied Mathematics and Mechanics / Zeitschrift für Angewandte Mathematik und Mechanik* 101.9 (Sept. 2021), pp. 1–21. ISSN: 0044-2267. DOI: `10.1002/zamm.202000289`.

[5] Mohamed Farid Abbas, Abdullah Ali Shaker, and Mosleh A. Al-Shamrani. "Hydraulic and volume change behaviors of compacted highly expansive soil under cyclic wetting and drying". In: *Journal of Rock Mechanics and Geotechnical Engineering* 15.2 (2023), pp. 486–499. ISSN: 1674-7755. DOI: `https://doi.org/10.1016/j.jrmge.2022.05.015`.

[6] Abo-el-nour N Abd-alla, Fatimah Alshaikh, Ivan Giorgio, and Alessandro Della Corte. "A mathematical model for longitudinal wave propagation in a magnetoelastic hollow circular cylinder of anisotropic material under the influence of initial hydrostatic stress". In: *Mathematics and Mechanics of Solids* 21.1 (2016), pp. 104–118. DOI: `10.1177/1081286515582883`.

[7] Ayman A. Abed and Wojciech T. Sołowski. "A study on how to couple thermo-hydro-mechanical behaviour of unsaturated soils: Physical equations, numerical implementation and examples". In: *Computers and Geotechnics* 92 (2017), pp. 132–155. ISSN: 0266-352X. DOI: `https://doi.org/10.1016/j.compgeo.2017.07.021`.

[8] Aybige Akinci, Luca Malagnini, and Fabio Sabetta. "Characteristics of the strong ground motions from the 6 April 2009 L'Aquila earthquake, Italy". In: *Soil Dynamics and Earthquake Engineering* 30.5 (2010), pp. 320–335. ISSN: 0267-7261. DOI: `https://doi.org/10.1016/j.soildyn.2009.12.006`.

[9] Mark Alexander and Hans Beushausen. "Durability, service life prediction, and modelling for reinforced concrete structures – review and critique". In: *Cement and Concrete Research* 122.April (Aug. 2019), pp. 17–29. ISSN: 00088846. DOI: `10.1016/j.cemconres.2019.04.018`.

[10] Gabriele Ameri, Dino Bindi, Francesca Pacor, and Fabrizio Galadini. "The 2009 April 6, Mw 6.3, L'Aquila (central Italy) earthquake: finite-fault effects on intensity data". In: *Geophysical Journal International* 186.2 (Aug. 2011), pp. 837–851. ISSN: 0956-540X. DOI: `10.1111/j.1365-246X.2011.05069.x`.

[11] Ugo Andreaus, Francesco dell'Isola, Ivan Giorgio, Luca Placidi, Tomasz Lekszycki, and Nicola Luigi Rizzi. "Numerical simulations of classical problems in two-dimensional (non) linear second gradient elasticity". In: *International Journal of Engineering Science* 108 (2016), pp. 34–50. ISSN: 0020-7225. DOI: `https://doi.org/10.1016/j.ijengsci.2016.08.003`.

[12] Michele De Angelo, Luca Placidi, Nima Nejadsadeghi, and Anil Misra. "Non-standard Timoshenko beam model for chiral metamaterial : Identification of stiffness parameters". In: 103 (2020). DOI: `10.1016/j.mechrescom.2019.103462`.

[13] Benedetta Antonielli, Marta Della Seta, Carlo Esposito, Gabriele Scarascia Mugnozza, Luca Schilirò, Marco Spadi, and Marco Tallini. "Quaternary rock avalanches in the Apennines: New data and interpretation of the huge clastic deposit of the L'Aquila Basin (central Italy)". In: *Geomorphology* 361 (2020), p. 107194.

[14] A. Apuzzo, R. Barretta, F. Fabbrocino, S. Ali Faghidian, R. Luciano, and F. Marotti de Sciarra. "Axial and torsional free vibrations of elastic nano-beams by stress-driven two-phase elasticity". In: *Journal of Applied and Computational Mechanics* 5.2 (2019), pp. 402–413. ISSN: 23834536. DOI: `10.22055/jacm.2018.26552.1338`.

[15] Ibrahim Tugrul Ardic, Mustafa Erden Yildizdag, and Ahmet Ergin. "An FE-BE Method for the Hydroelastic Vibration Analysis of Plates and Shells Partially in Contact with Fluid". In: *Developments and Novel Approaches in Nonlinear Solid Body Mechanics*. Ed. by Bilen Emek Abali and Ivan Giorgio. Cham: Springer International Publishing, 2020, pp. 267–300. ISBN: 978-3-030-50460-1. DOI: `10.1007/978-3-030-50460-1_16`.

[16] Harm Askes and Alexandra R Wallace. "Dynamic Bergan–Wang theory for thick plates". In: *Mathematics and Mechanics of Complex Systems* 10.2 (2022), pp. 191–204.

[17] N Auffray, F. Dell'Isola, V. A. Eremeyev, A. Madeo, and G Rosi. "Analytical continuum mechanics à la Hamilton-Piola least action principle for second gradient continua and capillary fluids". In: *Mathematics and Mechanics of Solids* 20.4 (Apr. 2015), pp. 375–417. ISSN: 17413028. DOI: `10.1177/1081286513497616`. arXiv: `1305.6744`.

[18] N Augenti and Fulvio Parisi. "Learning from Construction Failures due to the 2009 L'Aquila, Italy, Earthquake". In: *Journal of Performance of Constructed Facilities - J PERFORM CONSTR FACIL* 24 (Dec. 2010). DOI: `10.1061/(ASCE)CF.1943-5509.0000122`.

[19] Massimiliano Barchi, Giusy Lavecchia, Fabrizio Galadini, Paolo Messina, Alessandro Michetti, Laura Peruzza, Alberto Pizzi, Emanuele Tondi, and Eutizio Vittori. *Sintesi delle Conoscenze Sulle Faglie Attive in Italia Centrale: Parametrizzazione ai Fini della Caratterizzazione della Pericolosità Sismica.* Jan. 2000, p. 62.

[20] E Barchiesi, H Yang, CA Tran, L Placidi, and WH Müller. "Computation of brittle fracture propagation in strain gradient materials by the FEniCS library". In: *Mathematics and Mechanics of Solids* 26.3 (2021), pp. 325–340. DOI: `10.1177/1081286520954513`.

[21] Emilio Barchiesi and Nahiene Hamila. "Maximum mechano-damage power release-based phase-field modeling of mass diffusion in damaging deformable solids". In: *Zeitschrift für angewandte Mathematik und Physik* 73.1 (2022), p. 35.

[22] Emilio Barchiesi and Nahiene Hamila. "Maximum mechano-damage power release-based phase-field modeling of mass diffusion in damaging deformable solids". In: *Zeitschrift für angewandte Mathematik und Physik* 73.1 (Jan. 2022). ISSN: 1420-9039. DOI: `10.1007/s00033-021-01668-7`.

[23] Emilio Barchiesi, Anil Misra, Luca Placidi, and Emilio Turco. "Granular micromechanics-based identification of isotropic strain gradient parameters for elastic geometrically nonlinear deformations". In: *ZAMM Zeitschrift fur Angewandte Mathematik und Mechanik* 101.11 (2021), pp. 1–21. ISSN: 15214001. DOI: `10.1002/zamm.202100059`.

[24] Emilio Barchiesi, Anil Misra, Luca Placidi, Emilio Turco, Dmitry Timofeev, Valerii Maksimov, Nasrin Rezaei, Angelo Scrofani, et al. "Identification, based on granular micromechanics, of elastic isotropic strain gradient stiffness matrices for geometrically nonlinear deformations". In: *Book of abstracts*. 2021.

[25] Emilio Barchiesi, Mario Spagnuolo, and Luca Placidi. "Mechanical metamaterials: a state of the art". In: *Mathematics and Mechanics of Solids* 24.1 (2019), pp. 212–234. DOI: `http://doi.org/10.1177/1081286517735695`.

[26] Emilio Barchiesi, Hua Yang, Chuong Anthony Tran, Luca Placidi, and Wolfgang H Müller. "Computation of brittle fracture propagation in strain gradient materials by the FEniCS library". In: *Mathematics and Mechanics of Solids* (2020). DOI: `http://doi.org/10.1177/1081286520954513`.

[27] R. Barretta, S. Ali Faghidian, and R. Luciano. "Longitudinal vibrations of nano-rods by stress-driven integral elasticity". In: *Mechanics of Advanced Materials and Structures* 26.15 (2019), pp. 1307–1315. ISSN: 15376532. DOI: `10.1080/15376494.2018.1432806`.

[28] J. A. Bather. "A Diffusion Model for the Control of a Dam". In: *Advances in Applied Probability* 12.1 (2014), pp. 415–424.

[29] Zdenek P. Bazant and Spencer T. Wu. "DIRICHLET SERIES CREEP FUNCTION FOR AGING CONCRETE." In: *Journal of Engineering Mechanics - ASCE* 99.EM2 (Jan. 1973), pp. 367–387. ISSN: 0733-9399.

[30] Z. P. Bažant and S. T. Wu. "Rate-type creep law of aging concrete based on maxwell chain". In: *Matériaux et Constructions* 7.1 (Jan. 1974), pp. 45–60. ISSN: 0025-5432. DOI: `10.1007/BF02482679`.

[31] F. Bergamaschi, Giovanna Cultrera, Riccardo Azzara, Gabriele Ameri, P. Augliera, Bordoni Paola, F. Cara, R. Cogliano, Ezio D'Alema, Domenico Di Giacomo, Giuseppe Di Giulio, Antonio Fodarella, Gianlorenzo Franceschina, Fabrizio Galadini, Maria Gallipoli, Stefano Gori, P. Harabaglia, C. Ladina, and Monika Sobiesiak. "Evaluation of site effects in the Aterno river valley (Central Italy) from aftershocks of the 2009 L'Aquila earthquake". In: *Bulletin of Earthquake Engineering* 9 (June 2011), pp. 697–715. DOI: `10.1007/s10518-011-9245-7`.

[32] Alberto Maria Bersani, Paolo Caressa, and Alessandro Ciallella. "Numerical evidence for the approximation of dissipative systems by gyroscopically coupled oscillator chains". In: *Mathematics and Mechanics of Complex Systems* 10.3 (2022), pp. 265–278.

[33] D. Bindi, F. Pacor, L. Luzi, M. Massa, and G. Ameri. "The Mw 6.3, 2009 L'Aquila earthquake: Source, path and site effects from spectral analysis of strong motion data". In: *Geophysical Journal International* 179.3 (2009), pp. 1573–1579. ISSN: 0956540X. DOI: `10.1111/j.1365-246X.2009.04392.x`.

[34] M. Bîrsan, H. Altenbach, T. Sadowski, V.A. Eremeyev, and D. Pietras. "Deformation analysis of functionally graded beams by the direct approach". In: *Composites Part B: Engineering* 43.3 (2012), pp. 1315–1328. ISSN: 1359-8368. DOI: `https://doi.org/10.1016/j.compositesb.2011.09.003`.

[35] A. M. Blumetti, P. Di Manna, V. Comerci, L. Guerrieri, and E. Vittori. "Paleoseismicity of the San Demetrio ne' Vestini fault (L'Aquila Basin, Central Italy): Implications for seismic hazard". In: *Quaternary International* 451 (2017), pp. 129–142. ISSN: 10406182. DOI: `10.1016/j.quaint.2016.12.039`.

[36] AM Blumetti. "Neotectonic investigations and evidence of paleoseismicity in the epicentral area of the January–February 1703, Central Italy, earthquakes". In: *Perspectives in paleoseismology* 6 (1995), pp. 83–100.

[37] Paolo Boncio, Giusy Lavecchia, and Bruno Pace. " Defining a model of 3D seismogenic sources for Seismic Hazard Assessment applications: The case of central Apennines (Italy)". In: *Journal of Seismology* 8.9-10 (July 2004), pp. 4.7–425. ISSN: 3SN - 1573-157X. DOI: `10.1023/B:JOSE.0000038449.78801.05`.

[38] Peter Bormann, Michael Baumbach, Günther Bock, Helmut Grosser, George L. Choy, and John Boatwright. "Chapt 3: Seismic sources and source parameters". In: *New Manual of Seismological Observatory Practice (NMSOP-1)* (2009), pp. 1–94.

[39] Pier Paolo G. Bruno, Fabio Villani, and Luigi Improta. "High-Resolution Seismic Imaging of Fault-Controlled Basins: A Case Study From the 2009 Mw 6.1 Central Italy Earthquake". In: *Tectonics* 41.4 (2022), e2022TC007207. DOI: `https://doi.org/10.1029/2022TC007207`.

[40] Pierre Bruyelle. "Jean Demangeot.—Géomorphologie des Abruzzes adriatiques. Thèse pour le doctorat ès-lettres. Centre de Recherches et documentation cartographique et géographiques, n° hors-série-1965". In: *Hommes et Terres du Nord* 1.1 (1966), pp. 120–121.

[41] Habeger C.C. and Coffin D.W. "Institute of Paper Science and Technology A tanta , Georgia A Simple and Practical Pulp Kappa Test Method". In: 873 (2000).

[42] Giovanna Calderoni, Antonio Rovelli, and Rita Di Giovambattista. "Large amplitude variations recorded by an on-fault seismological station during the L'Aquila earthquakes: Evidence for a complex fault-induced site effect". In: *Geophysical Research Letters - GEOPHYS RES LETT* 37 (Dec. 2010). DOI: `10.1029/2010GL045697`.

[43] Luca Capacci, Fabio Biondini, and Andrea Titi. "Lifetime seismic resilience of aging bridges and road networks". In: *Structure and Infrastructure Engineering* 16.2 (2020), pp. 266–286. ISSN: 17448980. DOI: `10.1080/15732479.2019.1653937`.

[44] E. Carminati, Michele Lustrino, M. Cuffaro, and Carlo Doglioni. "Tectonics, magmatism and geodynamics of Italy: What we know and what we imagine, in: Beltrando, M., Peccerillo, A., Mattei, M., Conticelli, S., Doglioni, C. (Eds.), The Geology of Italy: tectonics and life along plate margins. Journal of Virtual Explorer, Electronic Edition". In: *ISSN* 36 (Jan. 2010), pp. 1441–8142.

[45] G. P. Cavinato and P. G. De Celles. "Extensional basins in the tectonically bimodal central Apennines fold-thrust belt, Italy: Response to corner flow above a subducting slab in retrograde motion". In: *Geology* 27.10 (Oct. 1999), pp. 955–958. ISSN: 0091-7613. DOI: `10.1130/0091-7613(1999)027<0955:EBITTB>2.3.CO;2`. eprint: `https://pubs.geoscienceworld.org/gsa/geology/article-pdf/27/10/955/3518268/i0091-7613-27-10-955.pdf`.

[46] Antonio Cazzani, Marcello Malagù, and Emilio Turco. “Isogeometric analysis of plane-curved beams”. In: *Mathematics and Mechanics of Solids* 21.5 (May 2016), pp. 562–577. ISSN: 1081-2865. DOI: `10.1177/1081286514531265`.

[47] N. Cefis and C. Comi. “Damage modelling in concrete subject to sulfate attack”. In: *Frattura ed Integrita Strutturale* 8.29 (2014), pp. 222–229. ISSN: 19718993. DOI: `10.3221/IGF-ESIS.29.19`.

[48] Nicola Cefis and Claudia Comi. “Chemo-mechanical modelling of the external sulfate attack in concrete”. In: *Cement and Concrete Research* 93.2017 (Mar. 2017), pp. 57–70. ISSN: 00088846. DOI: `10.1016/j.cemconres.2016.12.003`.

[49] Nicola Cefis, Roberto Fedele, and Marco G. Beghi. “An integrated methodology to estimate the effective elastic parameters of amorphous TiO2 nanostructured films, combining SEM images, finite element simulations and homogenization techniques”. In: *Mechanics Research Communications* 131 (2023), p. 104153. ISSN: 0093-6413. DOI: `https://doi.org/10.1016/j.mechrescom.2023.104153`. URL: `https://www.sciencedirect.com/science/article/pii/S0093641323001118`.

[50] Mehmet Çelebi, Paolo Bazzurro, Lauro Chiaraluce, Paolo Clemente, Luis Decanini, Adriano DeSortis, William Ellsworth, Antonella Gorini, Erol Kalkan, Sandro Marcucci, Guiliano Milana, Fabrizio Mollaioli, Marco Olivieri, Roberto Paolucci, Dario Rinaldis, Antonio Rovelli, Fabio Sabetta, and Christopher Stephens. “Recorded Motions of the 6 April 2009 Mw 6.3 L’Aquila, Italy, Earthquake and Implications for Building Structural Damage: Overview”. In: *Earthquake Spectra* 26.3 (2010), pp. 651–684. DOI: `10.1193/1.3450317`.

[51] Bernardino Chiaia, Valerio De Biagi, and Luca Placidi. “A damaged non-homogeneous Timoshenko beam model for a dam subjected to aging effects”. In: *Mathematics and Mechanics of Solids* 26.5 (May 2021), pp. 694–707. ISSN: 1081-2865. DOI: `10.1177/1081286520965644`.

[52] C. Chiarabba, A. Amato, M. Anselmi, P. Baccheschi, I. Bianchi, M. Cattaneo, G. Cecere, L. Chiaraluce, M. G. Ciaccio, P. De Gori, G. De Luca, M. Di Bona, R. Di Stefano, L. Faenza, A. Govoni, L. Improta, F. P. Lucente, A. Marchetti, L. Margheriti, F. Mele, A. Michelini, G. Monachesi, M. Moretti, M. Pastori, N. Piana Agostinetti, D. Piccinini, P. Roselli, D. Seccia, and L. Valoroso. “The 2009 L’Aquila (central Italy) Mw6.3 earthquake: main shock and aftershocks”. In: *Geophysical Research Letters* 36.18 (2009), pp. 1–6. ISSN: 00948276. DOI: `10.1029/2009GL039627`.

[53] A. Ciallella, D. Pasquali, M. Gołaszewski, F. D’Annibale, and I. Giorgio. “A rate-independent internal friction to describe the hysteretic behavior of pantographic structures under cyclic loads”. In: *Mechanics Research Communications* 116.August (Sept. 2021), p. 103761. ISSN: 00936413. DOI: `10.1016/j.mechrescom.2021.103761`.

[54] Alessandro Ciallella, Davide Pasquali, Francesco D'Annibale, and Ivan Giorgio. "Shear rupture mechanism and dissipation phenomena in bias-extension test of pantographic sheets: Numerical modeling and experiments". In: *Mathematics and Mechanics of Solids* 27.10 (2022), pp. 2170–2188. DOI: `10.1177/10812865221103573`.

[55] Alessandro Ciallella, Daria Scerrato, Mario Spagnuolo, and Ivan Giorgio. "A continuum model based on Rayleigh dissipation functions to describe a Coulomb-type constitutive law for internal friction in woven fabrics". In: *Zeitschrift fur Angewandte Mathematik und Physik* 73.5 (2022). ISSN: 14209039. DOI: `10.1007/s00033-022-01845-2`.

[56] R. Civico, V. Sapia, G. Di Giulio, F. Villani, S. Pucci, P. Baccheschi, S. Amoroso, L. Cantore, D. Di Naccio, S. Hailemikael, A. Smedile, M. Vassallo, M. Marchetti, and D. Pantosti. "Geometry and evolution of a fault-controlled Quaternary basin by means of TDEM and single-station ambient vibration surveys: The example of the 2009 L'Aquila earthquake area, central Italy". In: *Journal of Geophysical Research: Solid Earth* 122.3 (2017), pp. 2236–2259. DOI: `https://doi.org/10.1002/2016JB013451`.

[57] Martina Colombo and Claudia Comi. "Hydro-thermo-mechanical analysis of an existing gravity dam undergoing alkali-silica reaction". In: *Infrastructures* 4.3 (2019). ISSN: 24123811. DOI: `10.3390/infrastructures4030055`.

[58] C. Comi, R. Fedele, and U. Perego. "A chemo-thermo-damage model for the analysis of concrete dams affected by alkali-silica reaction". In: *Mechanics of Materials* 41.3 (Mar. 2009), pp. 210–230. ISSN: 01676636. DOI: `10.1016/j.mechmat.2008.10.010`.

[59] F. Cornacchia, F. Fabbrocino, N. Fantuzzi, R. Luciano, and R. Penna. "Analytical solution of cross- and angle-ply nano plates with strain gradient theory for linear vibrations and buckling". In: *Mechanics of Advanced Materials and Structures* 28.12 (2021), pp. 1201–1215. ISSN: 15376532. DOI: `10.1080/15376494.2019.1655613`.

[60] Domenico Cosentino, Riccardo Asti, Marco Nocentini, Elsa Gliozzi, Tassos Kotsakis, Massimo Mattei, Daniela Esu, Marco Spadi, Marco Tallini, Francesca Cifelli, Massimo Pennacchioni, Giuseppe Cavuoto, and Vincenzo Di Fiore. "New insights into the onset and evolution of the central Apennine extensional intermontane basins based on the tectonically active L'Aquila Basin (central Italy)". In: *GSA Bulletin* 129.9-10 (June 2017), pp. 1314–1336. ISSN: 0016-7606. DOI: `10.1130/B31679.1`.

[61] L. Cucci and A. Tertulliani. "Clues for a Relation between Rotational Effects Induced by the 2009 Mw 6.3 L'Aquila (Central Italy) Earthquake and Site and Source Effects". In: *Bulletin of The Seismological Society of America - BULL SEISMOL SOC AMER* 101 (May 2011), pp. 1109–1120. DOI: `10.1785/0120100264`.

[62] M. Cuomo and A. Nicolosi. "A poroplastic model for hygro-chemo-mechanical damage of concrete". In: *Computational Modelling of Concrete Structures - Proceedings of EURO-C 2006* (2006), pp. 533–542.

[63] Massimo Cuomo. “Continuum damage model for strain gradient materials with applications to 1D examples”. In: *Continuum Mechanics and Thermodynamics* 31 (2019), pp. 969–987. DOI: `10.1007/s00161-018-0698-7`.

[64] Massimo Cuomo, Loredana Contrafatto, and Leopoldo Greco. “A cohesive interface model with degrading friction coefficient”. In: *Mathematics and Mechanics of Complex Systems* 12.2 (2024), pp. 113–133.

[65] Hossein Darban, Raimondo Luciano, Andrea Caporale, and Francesco Fabbrocino. “Higher modes of buckling in shear deformable nanobeams”. In: *International Journal of Engineering Science* 154 (2020), p. 103338. ISSN: 00207225. DOI: `10.1016/j.ijengsci.2020.103338`.

[66] G. De Luca, R. Scarpa, L. Filippi, A. Gorini, S. Marcucci, P. Marsan, G. Milana, and E. Zambonelli. “A detailed analysis of two seismic sequences in Abruzzo, Central Apennines, Italy”. In: *Journal of Seismology* 4.1 (2000), pp. 1–21. ISSN: 13834649. DOI: `10.1023/A:1009870327083`.

[67] Gaetano De Luca, Sandro Marcucci, Giuliano Milana, and Tito Sanò. “Evidence of low-frequency amplification in the city of L’Aquila, central Italy, through a multidisciplinary approach including strong- and weak-motion data, ambient noise, and numerical modelling”. In: *Bulletin of the Seismological Society of America* 95.4 (2005), pp. 1469–1481. ISSN: 00371106. DOI: `10.1785/0120030253`.

[68] F. Dell’isola and Cz Woźniak. “On phase transition layers in certain micro-damaged two-phase solids”. In: *International Journal of Fracture* 83.2 (1997), pp. 175–189. ISSN: 03769429. DOI: `10.1023/A:1007331628395`.

[69] Francesco Dell’Isola, Alessandro Della Corte, and Ivan Giorgio. “Higher-gradient continua: The legacy of Piola, Mindlin, Sedov and Toupin and some future research perspectives”. In: *Mathematics and Mechanics of Solids* 22.4 (Apr. 2017), pp. 852–872. ISSN: 1081-2865. DOI: `10.1177/1081286515616034`.

[70] Francesco dell’Isola, Alessandro Della Corte, Antonio Battista, and Emilio Barchiesi. “Extensible Beam Models in Large Deformation Under Distributed Loading: A Numerical Study on Multiplicity of Solutions”. In: *Higher Gradient Materials and Related Generalized Continua*. Ed. by Holm Altenbach, Wolfgang H. Müller, and Bilen Emek Abali. Cham: Springer International Publishing, 2019, pp. 19–41. ISBN: 978-3-030-30406-5. DOI: `10.1007/978-3-030-30406-5_2`.

[71] Francesco dell’Isola, Ivan Giorgio, Marek Pawlikowski, and Nicola Luigi Rizzi. “Large deformations of planar extensible beams and pantographic lattices: heuristic homogenization, experimental and numerical examples of equilibrium”. In: *Proceedings of the Royal Society A: Mathematical, Physical and Engineering Sciences* 472.2185 (2016).

[72] Francesco dell'Isola, Tomasz Lekszycki, Mario Spagnuolo, Patrice Peyre, Corinne Dupuy, François Hild, Anil Misra, Emilio Barchiesi, Emilio Turco, and Justin Dirrenberger. "Experimental methods in pantographic structures". In: *Discrete and continuum models for complex metamaterials* (2020), p. 263. URL: `http://www.cambridge.org/it/academic/subjects/engineering/solid-mechanics-and-materials/discrete-and-continuum-models-complex-metamaterials?format=HB`.

[73] Francesco dell'Isola and Luca Placidi. "Variational principles are a powerful tool also for formulating field theories". In: *Variational Models and Methods in Solid and Fluid Mechanics*. Ed. by Francesco dell'Isola and Sergey Gavrilyuk. Vienna: Springer Vienna, 2011, pp. 1–15. ISBN: 978-3-7091-0983-0. DOI: `10.1007/978-3-7091-0983-0_1`.

[74] Francesco dell'Isola, Pierre Seppecher, Luca Placidi, Emilio Barchiesi, and Anil Misra. "8 Least Action and Virtual Work Principles for the Formulation of Generalized Continuum Models". In: *Discrete and Continuum Models for Complex Metamaterials* (2020), p. 327. URL: `http://www.cambridge.org/it/academic/subjects/engineering/solid-mechanics-and-materials/discrete-and-continuum-models-complex-metamaterials?format=HB`.

[75] Francesco dell'Isola, Pierre Seppecher, Mario Spagnuolo, Emilio Barchiesi, François Hild, Tomasz Lekszycki, Ivan Giorgio, Luca Placidi, Ugo Andreaus, Massimo Cuomo, et al. "Advances in pantographic structures: design, manufacturing, models, experiments and image analyses". In: *Continuum Mechanics and Thermodynamics* 31.4 (2019), pp. 1231–1282. DOI: `http://doi.org/10.1007/s00161-019-00806-x`.

[76] Francesco dell'Isola, Ivan A. Volkov, Leonid A. Igumnov, Simon R. Eugster, Svetlana Yu. Litvinchuk, Dmitri A. Kazakov, Vasilii A. Gorohov, and Bilen Emek Abali. "Estimating Fatigue Related Damage in Alloys under Block-type Non-symmetrical Low-cycle Loading". In: *New Achievements in Continuum Mechanics and Thermodynamics: A Tribute to Wolfgang H. Müller*. Ed. by Bilen Emek Abali, Holm Altenbach, Francesco dell'Isola, Victor A. Eremeyev, and Andreas Öchsner. Springer International Publishing, 2019, pp. 81–92. ISBN: 978-3-030-13307-8. DOI: `10.1007/978-3-030-13307-8_6`.

[77] Francesco dell'Isola, Simon R Eugster, Roberto Fedele, and Pierre Seppecher. "Second-gradient continua: From Lagrangian to Eulerian and back". In: *Mathematics and Mechanics of Solids* 27.12 (2022), pp. 2715–2750. DOI: `10.1177/10812865221078822`.

[78] A. Della Corte, A. Battista, F. dell'Isola, and P. Seppecher. "Large deformations of Timoshenko and Euler beams under distributed load". In: *Zeitschrift für angewandte Mathematik und Physik* 70.02 (2019). DOI: `10.1007/s00033-019-1098-y`.

[79] Alessandro Della Corte, Francesco dell'Isola, Raffaele Esposito, and Mario Pulvirenti. "Equilibria of a clamped Euler beam (Elastica) with distributed load: Large deformations". In: *Mathematical Models and Methods in Applied Sciences* 27.08 (2017), pp. 1391–1421. DOI: `10.1142/S0218202517500221`.

[80] Roberto Devoti, Grazia Pietrantonio, Anna Rita Pisani, Federica Riguzzi, and Enrico Serpelloni. "Present day kinematics of Italy". In: *Journal of the Virtual Explorer* 36.2 (2010).

[81] Giuseppe Di Giulio, Iolanda Gaudiosi, Fabrizio Cara, Giuliano Milana, and Marco Tallini. "Shear-wave velocity profile and seismic input derived from ambient vibration array measurements: The case study of downtown L'Aquila". In: *Geophysical Journal International* 198 (June 2014), pp. 848–866. DOI: `10.1093/gji/ggu162`.

[82] F. DI Michele, J. May, D. Pera, V. Kastelic, M. Carafa, C. Smerzini, I. Mazzieri, B. B. Rubino, P. F. Antonietti, A. Quarteroni, R. Aloisio, and P. Marcati. "Spectral element numerical simulation of the 2009 L'Aquila earthquake on a detailed reconstructed domain". In: *Geophysical Journal International* 230.1 (2022), pp. 29–49. ISSN: 1365246X. DOI: `10.1093/gji/ggac042`.

[83] John Douglas, Daniel Monfort, Caterina Negulescu, Agathe Roullé, and Olivier Sedan. "Limits on the potential accuracy of earthquake risk evaluations using the L'Aquila (Italy) earthquake as an example". In: *Annals of geophysics = Annali di geofisica* 58 (June 2015). DOI: `10.4401/ag-6651`.

[84] V. Eremeyev and L. Zubov. "On constitutive inequalities in nonlinear theory of elastic shells". In: *ZAMM - Journal of Applied Mathematics and Mechanics / Zeitschrift für Angewandte Mathematik und Mechanik* 87.2 (2007), pp. 94–101. DOI: `https://doi.org/10.1002/zamm.200610304`.

[85] Victor A Eremeyev. "Surface finite viscoelasticity and surface anti-plane waves". In: *International Journal of Engineering Science* 196 (2024), p. 104029.

[86] Victor A Eremeyev, Francesco dell'Isola, Claude Boutin, and David Steigmann. "Linear pantographic sheets: existence and uniqueness of weak solutions". In: *Journal of Elasticity* 132.2 (2018), pp. 175–196.

[87] Victor A. Eremeyev, Faris Saeed Alzahrani, Antonio Cazzani, Francesco Dell'Isola, Tasawar Hayat, Emilio Turco, and Violetta Konopińska-Zmysłowska. "On existence and uniqueness of weak solutions for linear pantographic beam lattices models". In: *Continuum Mechanics and Thermodynamics* 31.6 (2019), pp. 1843–1861. ISSN: 14320959. DOI: `10.1007/s00161-019-00826-7`.

[88] Victor A. Eremeyev, Antonio Cazzani, and Francesco Dell'Isola. "On nonlinear dilatational strain gradient elasticity". In: *Continuum Mechanics and Thermodynamics* 33.4 (2021), pp. 1429–1463. ISSN: 14320959. DOI: `10.1007/s00161-021-00993-6`.

[89] Victor A. Eremeyev, Leonid P. Lebedev, and Michael J. Cloud. “Acceleration waves in the nonlinear micromorphic continuum”. In: *Mechanics Research Communications* 93 (2018), pp. 70–74. ISSN: 0093-6413. DOI: `https://doi.org/10.1016/j.mechrescom.2017.07.004`.

[90] Victor A. Eremeyev and Wojciech Pietraszkiewicz. “The Nonlinear Theory of Elastic Shells with Phase Transitions”. In: *Journal of Elasticity* 74.1 (2004), pp. 67–86. DOI: `10.1023/B:ELAS.0000026106.09385.8c`.

[91] Simon Raphael Eugster. “Numerical analysis of nonlinear wave propagation in a pantographic sheet”. In: *Mathematics and Mechanics of Complex Systems* 9.3 (2022), pp. 293–310.

[92] Leonhard Euler. *Methodus inveniendi lineas curvas maximi minimive proprietate gaudentes sive solutio problematis isoperimetrici latissimo sensu accepti*. Vol. 1. Springer Science & Business Media, 1952.

[93] G. J.A.M. Eumelen, E. Bosco, A. S.J. Suiker, and J. J. Hermans. “Chemo-mechanical model for degradation of oil paintings by amorphous and crystalline metal soaps”. In: *European Journal of Mechanics, A/Solids* 97 (2023), p. 104827. ISSN: 09977538. DOI: `10.1016/j.euromechsol.2022.104827`.

[94] G. J.A.M. Eumelen, E. Bosco, A. S.J. Suiker, A. van Loon, and P. D. Iedema. “A computational model for chemo-mechanical degradation of historical oil paintings due to metal soap formation”. In: *Journal of the Mechanics and Physics of Solids* 132 (2019), p. 103683. ISSN: 00225096. DOI: `10.1016/j.jmps.2019.103683`.

[95] Francesco Fabbrocino, Marco Francesco Funari, Fabrizio Greco, Paolo Lonetti, Raimondo Luciano, and Rosa Penna. “Dynamic crack growth based on moving mesh method”. In: *Composites Part B: Engineering* 174.May (2019), p. 107053. ISSN: 13598368. DOI: `10.1016/j.compositesb.2019.107053`. URL: `https://doi.org/10.1016/j.compositesb.2019.107053`.

[96] R. Fedele and G. Maier. “Flat-jack tests and inverse analysis for the identification of stress states and elastic properties in concrete dams”. In: *Meccanica* 42.4 (2007), pp. 387–402. DOI: `10.1007/s11012-007-9061-y`.

[97] R. Fedele, S. Sessa, and N. Valoroso. “Image Correlation-Based Identification of Fracture Parameters for Structural Adhesives”. In: *Technische Mechanik - European Journal of Engineering Mechanics* 32.2-5 (July 2019), pp. 195–204.

[98] A. Ferraro, S. Grasso, M. Maugeri, and F. Totani. “Seismic response analysis in the southern part of the historic centre of the City of L’Aquila (Italy)”. In: *Soil Dynamics and Earthquake Engineering* 88 (2016), pp. 256–264. ISSN: 0267-7261. DOI: `https://doi.org/10.1016/j.soildyn.2016.06.009`.

[99] "Frequency variation in site response as observed from strong motion data of the L'Aquila (2009) seismic sequence". In: *Bulletin of Earthquake Engineering* 9.3 (2011), pp. 869–892. ISSN: 1573-1456. DOI: `10.1007/s10518-011-9266-2`.

[100] Marco Francesco Funari, Saverio Spadea, Francesco Fabbrocino, and Raimondo Luciano. "A moving interface finite element formulation to predict dynamic edge debonding in FRP-strengthened concrete beams in service conditions". In: *Fibers* 8.6 (2020). ISSN: 20796439. DOI: `10.3390/FIB8060042`.

[101] F. Galadini and P. Galli. "Active Tectonics in the Central Apennines (Italy) – Input Data for Seismic Hazard Assessment". In: *Natural Hazards* 22.3 (2000), pp. 225–268. ISSN: 1573-0840. DOI: `https://doi.org/10.1016/j.pepi.2006.07.008`.

[102] Iolanda Gaudiosi, Del Monaco Francesco, Milana Giuliano, and Tallini Marco. "Site effects in the Aterno River Valley (L'Aquila, Italy): Comparison between empirical and 2D numerical modelling starting from April 6th 2009 Mw 6.3 earthquake". In: *Bulletin of Earthquake Engineering* 12.2 (2014), pp. 697–716. ISSN: 15731456. DOI: `10.1007/s10518-013-9540-6`.

[103] Ivan Giorgio. "A variational formulation for one-dimensional linear thermoviscoelasticity". In: *Mathematics and Mechanics of Complex Systems* 9.4 (2022), pp. 397–412.

[104] Ivan Giorgio, Francesco dell'Isola, Ugo Andreaus, Faris Alzahrani, Tasawar Hayat, and Tomasz Lekszycki. "On mechanically driven biological stimulus for bone remodeling as a diffusive phenomenon". In: *Biomechanics and Modeling in Mechanobiology* 18.6 (Jan. 2019). ISSN: 1617-7940. DOI: `10.1007/s10237-019-01166-w`.

[105] Ivan Giorgio and Daria Scerrato. "Multi-scale concrete model with rate-dependent internal friction". In: *European Journal of Environmental and Civil Engineering* 21.7-8 (2017), pp. 821–839. DOI: `10.1080/19648189.2016.1144539`.

[106] Everardo Granda-Gutiérrez, S Pérez-Aguilar, Judi Fuentes Torres, J. C. Díaz-Guillén, A Campa-Castilla, A Garza-Gómez, J Candelas-Ramírez, and R. Mendez. "SYSTEM FOR DATA ACQUISITION AND STORAGE WITH APPLICATION IN A CREEP TEST MACHINE". In: Oct. 2010. DOI: `10.13140/2.1.4782.7207`.

[107] L. Greco, A. Scrofani, and M. Cuomo. "A non-linear symmetric G^1-conforming Bézier finite element formulation for the analysis of Kirchhoff beam". In: *Computer Methods in Applied Mechanics and Engineering* 387 (Dec. 2021), p. 114176. ISSN: 00457825. DOI: `10.1016/j.cma.2021.114176`.

[108] Leopoldo Greco, Massimo Cuomo, Domenico Castello, and Angelo Scrofani. "An updated Lagrangian Bézier finite element formulation for the analysis of slender beams". In: *Mathematics and Mechanics of Solids* 27.10 (2022), pp. 2110–2138. ISSN: 17413028. DOI: `10.1177/10812865221101549`.

[109] Alfio Grillo and Salvatore Di Stefano. "An a posteriori approach to the mechanics of volumetric growth". In: *Mathematics and Mechanics of Complex Systems* 11.1 (2023), pp. 57–86.

[110] Alfio Grillo and Salvatore Di Stefano. "Comparison between different viewpoints on bulk growth mechanics". In: *Mathematics and Mechanics of Complex Systems* 11.2 (2023), pp. 287–311.

[111] Chengchao Guo, Bo Sun, Dengping Hu, Fuming Wang, Mingsheng Shi, and Xiaolong Li. "A Field Experimental Study on the Diffusion Behavior of Expanding Polymer Grouting Material in Soil". In: *Soil Mechanics and Foundation Engineering* 56 (Aug. 2019). DOI: `10.1007/s11204-019-09586-7`.

[112] C. C. Habeger, D. W. Coffin, and B. Hojjatie. "Influence of humidity cycling parameters on the moisture-accelerated creep of polymeric fibers". In: *Journal of Polymer Science, Part B: Polymer Physics* 39.17 (2001), pp. 2048–2062. ISSN: 08876266. DOI: `10.1002/polb.1180`.

[113] Klaus Heiduschke. "On tensor projections, stress or stretch vectors and their relations to Mohr's three circles". In: *Mathematics and Mechanics of Complex Systems* 12.2 (2024), pp. 173–216.

[114] Wei Hong, Xuanhe Zhao, Jinxiong Zhou, and Zhigang Suo. "A theory of coupled diffusion and large deformation in polymeric gels". In: *Journal of the Mechanics and Physics of Solids* 56.5 (2008), pp. 1779–1793. ISSN: 00225096. DOI: `10.1016/j.jmps.2007.11.010`.

[115] T.V. Hromadka, C.E. Berenbrock, J.R. Freckleton, and G.L. Guymon. "A two-dimensional dam-break flood plain model". In: *Advances in Water Resources* 8.1 (1985), pp. 7–14. ISSN: 0309-1708. DOI: `https://doi.org/10.1016/0309-1708(85)90074-0`.

[116] *Italian Accelerometric Archive v4.0*. 2023. DOI: `10.13127/itaca.4.0`.

[117] A. Javili, F. dell'Isola, and P. Steinmann. "Geometrically nonlinear higher-gradient elasticity with energetic boundaries". In: *Journal of the Mechanics and Physics of Solids* 61.12 (2013), pp. 2381–2401. ISSN: 0022-5096. DOI: `https://doi.org/10.1016/j.jmps.2013.06.005`.

[118] In Ho Kim, Haemin Jeon, Seung Chan Baek, Won Hwa Hong, and Hyung Jo Jung. "Application of crack identification techniques for an aging concrete bridge inspection using an unmanned aerial vehicle". In: *Sensors (Switzerland)* 18.6 (2018), pp. 1–14. ISSN: 14248220. DOI: `10.3390/s18061881`.

[119] Kyaw Ye Ko and Yury Solyaev. "Explicit benchmark solution for topology optimization of variable-thickness plates". In: *Mathematics and Mechanics of Complex Systems* 11.3 (2023), pp. 381–392.

[120] F. dell'Isola L. Placidi and A. Madeo. "Nonlinear Analysis of Damaged Concrete Using Hemivariational Principles". In: *European Journal of Mechanics - A/Solids* 34 (2012), pp. 57–65.

[121] F. dell'Isola L. Placidi and V. V. Porubov. "Hemivariational Formulation for Problems with Non-Smooth Energy Functions". In: *Computers & Mathematics with Applications* 66 (2013), pp. 1714–1722.

[122] F. dell'Isola L. Placidi and V. V. Porubov. "Variational Formulation of Problems Involving Non-Smooth Constitutive Equations". In: *Continuum Mechanics and Thermodynamics* 17 (2005), pp. 409–422.

[123] F. dell'Isola L. Placidi and D. Tzarouchis. "On the Analysis of Non-Smooth Contact Problems Using Hemivariational Principles". In: *Mechanics Research Communications* 37 (2010), pp. 243–248.

[124] F. dell'Isola L. Placidi and G. M. Walker. "A Hemivariational Approach to the Analysis of Concrete Structures". In: *International Journal of Solids and Structures* 49 (2012), pp. 231–240.

[125] Joseph Louis Lagrange. *Mécanique analytique*. Vol. 1. Mallet-Bachelier, 1853.

[126] Joseph Louis Lagrange. *Mécanique analytique*. Vol. 2. Mallet-Bachelier, 1855.

[127] Giuseppe Lanzo and Alessandro Pagliaroli. "Seismic site effects at near-fault strong-motion stations along the Aterno River Valley during the Mw=6.3 2009 L'Aquila earthquake". In: *Soil Dynamics and Earthquake Engineering* 40 (2012), pp. 1–14. ISSN: 0267-7261. DOI: `https://doi.org/10.1016/j.soildyn.2012.04.004`.

[128] Marco Laudato and Emilio Barchiesi. "Non-linear Dynamics of Pantographic Fabrics: Modelling and Numerical Study". In: *Wave Dynamics, Mechanics and Physics of Microstructured Metamaterials: Theoretical and Experimental Methods*. Cham: Springer International Publishing, 2019, pp. 241–254. ISBN: 978-3-030-17470-5. DOI: `10.1007/978-3-030-17470-5_17`.

[129] Raimondo Luciano, Hossein Darban, Chiara Bartolomeo, Francesco Fabbrocino, and Daniela Scorza. "Free flexural vibrations of nanobeams with non-classical boundary conditions using stress-driven nonlocal model". In: *Mechanics Research Communications* 107 (2020). ISSN: 00936413. DOI: `10.1016/j.mechrescom.2020.103536`.

[130] Federica Magnoni, Emanuele Casarotti, Alberto Michelini, Antonio Piersanti, Dimitri Komatitsch, Daniel Peter, and Jeroen Tromp. "Spectral-element simulations of seismic waves generated by the 2009 L'Aquila earthquake". In: *Bulletin of the Seismological Society of America* 104.1 (2014), pp. 73–94. ISSN: 00371106. DOI: `10.1785/0120130106`.

[131] Mohammad Malikan and Victor A. Eremeyev. "A new hyperbolic-polynomial higher-order elasticity theory for mechanics of thick FGM beams with imperfection in the material composition". In: *Composite Structures* 249 (2020), p. 112486. ISSN: 0263-8223. DOI: `https://doi.org/10.1016/j.compstruct.2020.112486`.

[132] Mohammad Malikan and Victor A. Eremeyev. “On time-dependent nonlinear dynamic response of micro-elastic solids”. In: *International Journal of Engineering Science* 182 (2023), p. 103793. ISSN: 0020-7225. DOI: `https://doi.org/10.1016/j.ijengsci.2022.103793`.

[133] Geminiano Mancusi, Francesco Fabbrocino, Luciano Feo, and Fernando Fraternali. “Size effect and dynamic properties of 2D lattice materials”. In: *Composites Part B: Engineering* 112 (2017), pp. 235–242. ISSN: 13598368. DOI: `10.1016/j.compositesb.2016.12.026`.

[134] A. Mannella, L. Macerola, A. Martinelli, Antonio Sabino, and M. Tallini. “The local seismic response and the effects of the 2016 central Italy earthquake on the buildings of L’aquila downtown”. In: *Bollettino di Geofisica Teorica ed Applicata* 60.2 (2019), pp. 263–276. ISSN: 00066729. DOI: `10.4430/bgta0241`.

[135] Lucia Margheriti, Lauro Chiaraluce, Christophe Voisin, Giovanna Cultrera, Aladino Govoni, Milena Moretti, Bordoni Paola, Riccardo Azzara, Luisa Valoroso, Raffaele Di Stefano, Armand Mariscal, L. Improta, Francesca Pacor, Giuliano Milana, Marco Mucciarelli, Stefano Parolai, Alessandro Amato, Claudio Chiarabba, and Giulio Selvaggi. “Rapid response seismic networks in Europe: lessons learnt from the L’Aquila earthquake emergency”. In: *Annals of geophysics = Annali di geofisica* 54 (Sept. 2011).

[136] A Masi, V Manfredi, M Vona, F Braga, and A I Salvatori. “Prestazioni delle tamponature e tramezzature negli edifici in c . a .: implicazioni progettuali e costruttive alla luce dell ’ esperienza del terremoto dell ’ Abruzzo 2009”. In: (2009), pp. 51–66.

[137] Gennadi Mikhasev, Barış Erbaş, and Victor A Eremeyev. “Anti-plane shear waves in an elastic strip rigidly attached to an elastic half-space”. In: *International Journal of Engineering Science* 184 (2023), p. 103809.

[138] R. D. Mindlin. “Micro-structure in linear elasticity”. In: *Archive for Rational Mechanics and Analysis* 16.1 (Jan. 1964), pp. 51–78. DOI: `10.1007/BF00248490`.

[139] Anil Misra, Luca Placidi, Francesco dell’Isola, and Emilio Barchiesi. “Identification of a geometrically nonlinear micromorphic continuum via granular micromechanics”. In: *Zeitschrift für angewandte Mathematik und Physik* 72.4 (2021). DOI: `10.1007/s00033-021-01587-7`.

[140] Anil Misra, Luca Placidi, and Emilio Turco. “Variational Methods for Discrete Models of Granular Materials”. In: *Encyclopedia of Continuum Mechanics*. Ed. by Holm Altenbach and Andreas Öchsner. Berlin, Heidelberg: Springer Berlin Heidelberg, 2020, pp. 2621–2634. ISBN: 978-3-662-55771-6. DOI: `10.1007/978-3-662-55771-6_172`.

[141] Anil Misra and Payam Poorsolhjouy. “Elastic behavior of 2D grain packing modeled as micromorphic media based on granular micromechanics”. In: *Journal of Engineering Mechanics* 143.1 (2017), p. C4016005.

[142] Anil Misra and Payam Poorsolhjouy. "Grain-and macro-scale kinematics for granular micromechanics based small deformation micromorphic continuum model". In: *Mechanics Research Communications* 81 (2017), pp. 1–6.

[143] Anil Misra and Payam Poorsolhjouy. "Grain-and macro-scale kinematics for granular micromechanics based small deformation micromorphic continuum model". In: *Mechanics Research Communications* 81 (2017), pp. 1–6.

[144] Anil Misra and Payam Poorsolhjouy. "Granular micromechanics model for damage and plasticity of cementitious materials based upon thermomechanics". In: *Mathematics and Mechanics of Solids* 25.10 (2020), pp. 1778–1803.

[145] Paola Monaco and Sara Amoroso. "Site Effects from the Building Scale to the Seismic Microzonation Scale: Examples from the Experience of L'Aquila". In: *Procedia Engineering* 158 (2016), pp. 517–522. ISSN: 1877-7058. DOI: `https://doi.org/10.1016/j.proeng.2016.08.482`.

[146] Rogier Pieter Louis. Nijssen, Faculty of Aerospace Engineering. Design TU Delft, and Production of Composite Structures Group. *Fatigue life prediction and strength degradation of wind turbine reactor blade composites.* October. 2006. ISBN: 9789090212210.

[147] Marco Nocentini, Riccardo Asti, Domenico Cosentino, Federica Durante, Elsa Gliozzi, Luca Macerola, and Marco Tallini. "Plio-Quaternary geology of L'Aquila–Scoppito Basin (Central Italy)". In: *Journal of Maps* 13.2 (2017), pp. 563–574.

[148] Marco Nocentini, Domenico Cosentino, Marco Spadi, and Marco Tallini. *Plio-Quaternary geology of the Paganica-San Demetrio-Castelnuovo Basin (Central Italy).* 2018.

[149] C. Nunziata and M.R. Costanzo. "Ground motion modeling for site effects at L'Aquila and middle Aterno river valley (central Italy) for the MW 6.3, 2009 earthquake". In: *Soil Dynamics and Earthquake Engineering* 61-62 (2014), pp. 107–123. ISSN: 0267-7261. DOI: `https://doi.org/10.1016/j.soildyn.2014.01.011`.

[150] C. Nunziata, M.R. Costanzo, F. Vaccari, and G.F. Panza. "Evaluation of Linear and Nonlinear Site Effects for the MW 6.3, 2009 L'Aquila Earthquake". In: *Earthquake Research and Analysis*. Ed. by Sebastiano D'Amico. Rijeka: IntechOpen, 2012. Chap. 5. DOI: `10.5772/27355`.

[151] Concettina Nunziata, Franco Vaccari, and G. Panza. "The M w 6.3, 2009 L'Aquila earthquake: Linear and nonlinear site effects". In: (Jan. 2010), pp. 99–104.

[152] Marc Olive and Nicolas Auffray. "Symmetry classes in piezoelectricity from second-order symmetries". In: *Mathematics and Mechanics of Complex Systems* 9.1 (2021), pp. 77–105.

[153] P. D. Panagiotopoulos. *Hemivariational Inequalities: Applications in Mechanics and Engineering.* Springer, 1985.

[154] Massimo Paradiso, Salvatore Sessa, Nicolò Vaiana, Francesco Marmo, and Luciano Rosati. "Shear properties of isotropic and homogeneous beam-like solids having arbitrary cross sections". In: *International Journal of Solids and Structures* 216 (2021), pp. 231–249. ISSN: 00207683. DOI: `10.1016/j.ijsolstr.2021.01.012`.

[155] L Placidi, Emilio Barchiesi, Francesco Dell'Isola, Valerii Maksimov, Anil Misra, Nasrin Rezaei, Angelo Scrofani, Dmitry Timofeev, et al. "A granular-based elasto-plastic–damage energy formulation for strain gradient solids". In: *Book of Abstracts.* 2021.

[156] L. Placidi and F. dell'Isola. "A Variational Approach to Hemivariational Inequalities for Nonlinear Damped Oscillators". In: *Journal of Mathematical Analysis and Applications* 339 (2008), pp. 205–214.

[157] Luca Placidi. "A variational approach for a nonlinear 1-dimensional second gradient continuum damage model". In: *Continuum Mechanics and Thermodynamics* 27.4-5 (Sept. 2015), pp. 623–638. ISSN: 0935-1175. DOI: `10.1007/s00161-014-0338-9`.

[158] Luca Placidi. "A variational approach for a nonlinear one-dimensional damage-elasto-plastic second-gradient continuum model". In: (2016), pp. 119–137. DOI: `10.1007/s00161-014-0405-2`.

[159] Luca Placidi, Ugo Andreaus, Alessandro Della Corte, and Tomasz Lekszycki. "Gedanken experiments for the determination of two-dimensional linear second gradient elasticity coefficients". In: *Zeitschrift fur Angewandte Mathematik und Physik* 66.6 (2015), pp. 3699–3725. ISSN: 00442275. DOI: `10.1007/s00033-015-0588-9`.

[160] Luca Placidi and Emilio Barchiesi. "Energy approach to brittle fracture in strain-gradient modelling". In: *Proceedings of the Royal Society A: Mathematical, Physical and Engineering Sciences* 474.2210 (2018), p. 20170878. DOI: `10.1098/rspa.2017.0878`.

[161] Luca Placidi, Emilio Barchiesi, Francesco Dell'Isola, Valerii Maksimov, Anil Misra, Nasrin Rezaei, Angelo Scrofani, and Dmitry Timofeev. "On a hemi-variational formulation for a 2D elasto-plastic-damage strain gradient solid with granular microstructure". In: *Mathematics in Engineering* 5.1 (2022), pp. 1–24. ISSN: 2640-3501. DOI: `10.3934/mine.2023021`.

[162] Luca Placidi, Emilio Barchiesi, Anil Misra, and Ugo Andreaus. "Variational Methods in Continuum Damage and Fracture Mechanics". In: *Encyclopedia of Continuum Mechanics.* Ed. by Holm Altenbach and Andreas Öchsner. Berlin, Heidelberg: Springer Berlin Heidelberg, 2020, pp. 2634–2643. ISBN: 978-3-662-55771-6. DOI: `10.1007/978-3-662-55771-6_199`.

[163] Luca Placidi, Emilio Barchiesi, Anil Misra, and Dmitry Timofeev. "Micromechanics-based elasto-plastic – damage energy formulation for strain gradient solids with granular microstructure". In: *Continuum Mechanics and Thermodynamics* (2021). ISSN: 1432-0959. DOI: `10.1007/s00161-021-01023-1`.

[164] Luca Placidi, Fabio Di Girolamo, and Roberto Fedele. "Variational study of a Maxwell–Rayleigh-type finite length model for the preliminary design of a tensegrity chain with a tunable band gap". In: *Mechanics Research Communications* 136 (2024), p. 104255. ISSN: 0093-6413. DOI: `https://doi.org/10.1016/j.mechrescom.2024.104255`.

[165] Luca Placidi and Amr Ramadan El Dhaba. "Semi-inverse method à la Saint-Venant for two-dimensional linear isotropic homogeneous second-gradient elasticity". In: *Mathematics and Mechanics of Solids* 22.5 (2017), pp. 919–937. ISSN: 17413028. DOI: `10.1177/1081286515616043`.

[166] Luca Placidi, Mohammed Galal El Sherbiny, and Paolo Baragatti. "Experimental investigation for the existence of frequency band gap in a microstructure model". In: *Mathematics and Mechanics of Complex Systems* 9.4 (2022), pp. 413–421.

[167] Luca Placidi, Anil Misra, and Emilio Barchiesi. "Simulation results for damage with evolving microstructure and growing strain gradient moduli". In: *Continuum Mechanics and Thermodynamics* 31.4 (July 2019), pp. 1143–1163. ISSN: 1432-0959. DOI: `10.1007/s00161-018-0693-z`.

[168] Luca Placidi, Anil Misra, and Emilio Barchiesi. "Two-dimensional strain gradient damage modeling: a variational approach". In: *Zeitschrift fur Angewandte Mathematik und Physik* 69.3 (2018). ISSN: 00442275. DOI: `10.1007/s00033-018-0947-4`.

[169] Luca Placidi, Giuseppe Rosi, Ivan Giorgio, and Angela Madeo. "Reflection and transmission of plane waves at surfaces carrying material properties and embedded in second-gradient materials". In: *Mathematics and Mechanics of Solids* 19.5 (2014), pp. 555–578. DOI: `10.1177/1081286512474016`.

[170] S. Pondrelli, S. Salimbeni, G. Ekström, A. Morelli, P. Gasperini, and G. Vannucci. "The Italian CMT dataset from 1977 to the present". In: *Physics of the Earth and Planetary Interiors* 159.3 (2006), pp. 286–303. ISSN: 0031-9201. DOI: `https://doi.org/10.1016/j.pepi.2006.07.008`.

[171] Dmitry Ponomarev. "A generalised time-evolution model for contact problems with wear and its analysis". In: *Mathematics and Mechanics of Complex Systems* 10.3 (2022), pp. 279–319.

[172] Ermanno Ragozzino. "Nonlinear seismic response in the western L'Aquila basin (Italy): Numerical FEM simulations vs. ground motion records". In: *Engineering Geology* 174 (2014), pp. 46–60. ISSN: 0013-7952. DOI: `https://doi.org/10.1016/j.enggeo.2014.03.010`.

[173] K. R. Rajagopal. "Diffusion through polymeric solids undergoing large deformations". In: *Materials Science and Technology* 19.9 (2003), pp. 1175–1180. DOI: `10.1179/026708303225004729`.

[174] K.R. Rajagopal, A.R. Srinivasa, and A.S. Wineman. "On the shear and bending of a degrading polymer beam". In: *International Journal of Plasticity* 23.9 (Sept. 2007), pp. 1618–1636. ISSN: 07496419. DOI: `10.1016/j.ijplas.2007.02.007`.

[175] J. N. Reddy. *Energy Principles and Variational Methods in Applied Mechanics*. Wiley, 2002.

[176] Nasrin Rezaei, Emilio Barchiesi, Dmitry Timofeev, C Anthony Tran, Anil Misra, and Luca Placidi. "Solution of a paradox related to the rigid bar pull-out problem in standard elasticity". In: *Mechanics Research Communications* 126 (2022).

[177] G. Rosi, I. Giorgio, and V.A. Eremeyev. "Propagation of linear compression waves through plane interfacial layers and mass adsorption in second gradient fluids". In: *ZAMM - Journal of Applied Mathematics and Mechanics / Zeitschrift für Angewandte Mathematik und Mechanik* 93.12 (2013), pp. 914–927. DOI: `https://doi.org/10.1002/zamm.201200285`.

[178] Giuseppe Rosi, Nicolas Auffray, and Christelle Combescure. "On the failure of classic elasticity in predicting elastic wave propagation in gyroid lattices for very long wavelengths". In: *Symmetry* 12.8 (2020).

[179] A Rovida, M Locati, R Camassi, B Lolli, P Gasperini, and A Antonucci. *Catalogo Parametrico dei Terremoti Italiani (CPTI15), versione 4.0, INGV [data set]*. 2022.

[180] Andrea Rovida, Mario Locati, Romano Camassi, Barbara Lolli, and Paolo Gasperini. "The Italian earthquake catalogue CPTI15". In: *Bulletin of Earthquake Engineering* 18.7 (2020), pp. 2953–2984. ISSN: 1573-1456. DOI: `10.1007/s10518-020-00818-y`.

[181] R. Rupakhety and R. Sigbjörnsson. "A note on the L'Aquila earthquake of 6 April 2009: Permanent ground displacements obtained from strong-motion accelerograms". In: *Soil Dynamics and Earthquake Engineering* 30.4 (2010), pp. 215–220. ISSN: 0267-7261. DOI: `https://doi.org/10.1016/j.soildyn.2009.10.008`.

[182] Fernando Saitta, Paolo Clemente, Giacomo Buffarini, Giovanni Bongiovanni, Antonello Salvatori, and Cristian Grossi. "Base Isolation of Buildings with Curved Surface Sliders: Basic Design Criteria and Critical Issues". In: *Advances in Civil Engineering* 2018 (2018), p. 1569683. ISSN: 1687-8086. DOI: `10.1155/2018/1569683`.

[183] Vladimir Salnikov. "On numerical approaches to the analysis of topology of the phase space for dynamical integrability". In: *Chaos, Solitons & Fractals* 57 (2013), pp. 155–161. ISSN: 0960-0779. DOI: `https://doi.org/10.1016/j.chaos.2013.10.004`.

[184] Vladimir Salnikov and Aziz Hamdouni. “From modelling of systems with constraints to generalized geometry and back to numerics”. In: *ZAMM - Journal of Applied Mathematics and Mechanics / Zeitschrift für Angewandte Mathematik und Mechanik* 99.6 (2019), e201800218. DOI: `https://doi.org/10.1002/zamm.201800218`.

[185] Antonello Salvatori. “Seismic base isolation: retrofitting application in structures damaged by earthquake”. In: *Proceedings of 16th European conference on earthquake engineering ECEE, Thessaloniki, Greece*. 2018.

[186] Giulio Sciarra, Francesco dell’Isola, and Olivier Coussy. “Second gradient poromechanics”. In: *International Journal of Solids and Structures* 44.20 (2007), pp. 6607–6629. ISSN: 0020-7683. DOI: `https://doi.org/10.1016/j.ijsolstr.2007.03.003`.

[187] Angelo Scrofani, Emilio Barchiesi, Chiaia Bernardino, Anil Misra, and Luca Placidi. “Diffusion of an ammalorating fluid through a dam-shaped bidimensional body for the estimation of its life time”. In: (). unpublished.

[188] Angelo Scrofani, Emilio Barchiesi, Bernardino Chiaia, Anil Misra, and Luca Placidi. “Fluid diffusion related aging effect in a concrete dam modeled as a Timoshenko beam”. In: *Mathematics and Mechanics of Complex Systems* 11.2 (2023), pp. 313–334.

[189] “Seismic site characterisation of Red Soil and soil-building resonance effects in L’Aquila downtown (Central Italy)”. In: *Bulletin of Engineering Geology and the Environment* 79.8 (2020), pp. 4021–4034. ISSN: 1435-9537. DOI: `10.1007/s10064-020-01795-x`.

[190] I.H. Shames and J.M. Pitarresi. *Introduction to Solid Mechanics*. Prentice Hall, 2000. ISBN: 9780132677585.

[191] Basant Lal Sharma and Victor A Eremeyev. “Wave transmission across surface interfaces in lattice structures”. In: *International Journal of Engineering Science* 145 (2019), p. 103173.

[192] Chiara Smerzini and Manuela Villani. “Broadband Numerical Simulations in Complex Near-Field Geological Configurations: The Case of the 2009 Mw 6.3 L’Aquila Earthquake”. In: *Bulletin of the Seismological Society of America* 102.6 (Dec. 2012), pp. 2436–2451. ISSN: 0037-1106. DOI: `10.1785/0120120002`. URL: `https://doi.org/10.1785/0120120002`.

[193] Christian Soize. “An overview on uncertainty quantification and probabilistic learning on manifolds in multiscale mechanics of materials”. In: *Mathematics and Mechanics of Complex Systems* 11.1 (2023), pp. 87–174.

[194] Yury Solyaev, Sergey Lurie, Emilio Barchiesi, and Luca Placidi. “On the dependence of standard and gradient elastic material constants on a field of defects”. In: *Mathematics and Mechanics of Solids* 25.1 (Jan. 2020), pp. 35–45. ISSN: 1081-2865. DOI: `10.1177/1081286519861827`.

[195] Ha-Won Song, Seung-Jun Kwon, Keun-Joo Byun, and Chan-Kyu Park. "Predicting carbonation in early-aged cracked concrete". In: *Cement and Concrete Research* 36.5 (May 2006), pp. 979–989. ISSN: 00088846. DOI: `10.1016/j.cemconres.2005.12.019`.

[196] Marco Spadi, Marco Tallini, Matteo Albano, Domenico Cosentino, Marco Nocentini, and Michele Saroli. "New insights on bedrock morphology and local seismic amplification of the Castelnuovo village (L'Aquila Basin, Central Italy)". In: *Engineering Geology* 297 (2022), p. 106506. ISSN: 0013-7952. DOI: `https://doi.org/10.1016/j.enggeo.2021.106506`.

[197] M. Spagnuolo, K. Barcz, A. Pfaff, F. dell'Isola, and P. Franciosi. "Qualitative pivot damage analysis in aluminum printed pantographic sheets: Numerics and experiments". In: *Mechanics Research Communications* 83 (2017), pp. 47–52. ISSN: 0093-6413. DOI: `https://doi.org/10.1016/j.mechrescom.2017.05.005`.

[198] Mario Spagnuolo. "A targeted review on large deformations of planar elastic beams : extensibility , distributed loads , buckling and post-buckling". In: 24.1 (2019), pp. 258–280. DOI: `10.1177/1081286517737000`.

[199] Wilcot John Speelman, R. Lindsay, R. T. Newman, and A. D. Joseph. "Modelling and Measurement of Radon Diffusion Through Soil for Application on Mine Tailings Dams". In: *VII Radiation Physics & Protection Conference* November (2004), pp. 279–287.

[200] Jonathan P. Stewart, Giuseppe Lanzo, Alessandro Pagliaroli, Giuseppe Scasserra, Giuseppe Di Capua, Silvia Peppoloni, Robert Darragh, and Nicholas Gregor. "Ground Motion Recordings from the Mw 6.3 2009 L'Aquila Earthquake in Italy and their Engineering Implications". In: *Earthquake Spectra* 28.1 (2012), pp. 317–345. DOI: `10.1193/1.3673621`.

[201] Flavio Stochino, Antonio Cazzani, Gian Giaccu, and Emilio Turco. "Dynamics of Strongly Curved Concrete Beams by Isogeometric Finite Elements". In: Apr. 2018, pp. 231–247. ISBN: 978-3-319-78935-4. DOI: `10.1007/978-3-319-78936-1_17`.

[202] Marco Tallini, Marco Spadi, Domenico Cosentino, Marco Nocentini, Giuseppe Cavuoto, and Vincenzo Di Fiore. "High-resolution seismic reflection exploration for evaluating the seismic hazard in a Plio-Quaternary intermontane basin (L'Aquila downtown, central Italy)". In: *Quaternary international* 532 (2019), pp. 34–47.

[203] Michele Tepedino. "The mechanical role of the periodontal ligament for developing mathematical models in orthodontics". In: *Mathematics and Mechanics of Complex Systems* 11.4 (2023), pp. 525–539.

[204] A. Tertulliani, Luca Arcoraci, Michele Berardi, Filippo Bernardini, Camassi Romano, C. Castellano, S. Mese, Emanuela Ercolani, Laura Graziani, Ilaria Leschiutta, A. Rossi, and M. Vecchi. "An application of EMS98 in a medium-sized city: The case of L'Aquila (Central Italy) after the April 6, 2009 Mw 6.3 earthquake". In: *Bulletin of Earthquake Engineering* 9 (Feb. 2011), pp. 67–80. DOI: `10.1007/s10518-010-9188-4`.

[205] A. Tertulliani, I. Leschiutta, P. Bordoni, and G. Milana. "Damage Distribution in L'Aquila City (Central Italy) during the 6 April 2009 Earthquake". In: *Bulletin of the Seismological Society of America* 102.4 (Aug. 2012), pp. 1543–1553. ISSN: 0037-1106. DOI: `10.1785/0120110205`.

[206] "The contribution of seismic data in microzonation studies for downtown L'Aquila". In: *Bulletin of Earthquake Engineering* 9.3 (2011), pp. 741–759. ISSN: 1573-1456. DOI: `10.1007/s10518-011-9246-6`.

[207] "The L'Aquila earthquake—A view of site effects and building behavior from temporary networks". In: *Bulletin of Earthquake Engineering* 9.3 (2011), pp. 691–695. ISSN: 1573-1456. DOI: `10.1007/s10518-011-9270-6`.

[208] Michael D.A. Thomas and Phil B. Bamforth. "Modelling chloride diffusion in concrete". In: *Cement and Concrete Research* 29.4 (Apr. 1999), pp. 487–495. ISSN: 00088846. DOI: `10.1016/S0008-8846(98)00192-6`.

[209] *Time Domain Moment Tensor (TDMT) [Data set].* 2006. DOI: `https://doi.org/10.13127/TDMT`.

[210] Dmitry Timofeev, Emilio Barchiesi, Anil Misra, and Luca Placidi. "Hemivariational continuum approach for granular solids with damage-induced anisotropy evolution". In: *Mathematics and Mechanics of Solids* 26.5 (May 2021), pp. 738–770. ISSN: 1081-2865. DOI: `10.1177/1081286520968149`.

[211] José Manuel Torres Espino, Jaime Heman Espinoza Sandoval, Chuong Anthony Tran, Roberto Fedele, Emilio Turco, Francesco dell'Isola, Luca Placidi, Anil Misra, Francisco James León Trujillo, and Emilio Barchiesi. "Validation of a Hemi-Variational Block-Based Approach to the Modelling of Common In-plane Failures in Masonry Structures". In: *Sixty Shades of Generalized Continua: Dedicated to the 60th Birthday of Prof. Victor A. Eremeyev.* Springer, 2023, pp. 191–210.

[212] C Anthony Tran and Emilio Barchiesi. "A new block-based approach for the analysis of damage in masonries undergoing large deformations". In: *Continuum Mechanics and Thermodynamics* (2022), pp. 1–30.

[213] C Anthony Tran, Emilio Barchiesi, Luca Placidi, and Francisco James León Trujillo. "A block-based variational elasto-damage model for masonry analysis inspired from granular micromechanics: Preliminary study". In: *Mechanics Research Communications* 118 (2021).

[214] Emilio Turco and Emilio Barchiesi. "Kinematically triggered nonlinear vibrations of Hencky-type pantographic sheets". In: *Mathematics and Mechanics of Complex Systems* 9.3 (2022), pp. 311–335.

[215] Emilio Turco and Emilio Barchiesi. "Kinematically-triggered nonlinear vibrations of Hencky-type pantographic sheets". In: *Mathematics and Mechanics of Complex Systems* 9 (Dec. 2021), pp. 311–335. DOI: `10.2140/memocs.2021.9.311`.

[216] Emilio Turco, Emilio Barchiesi, Alessandro Ciallella, and Francesco dell'Isola. "A new block-based approach for the analysis of damage in masonries undergoing large deformations". In: *Continuum Mechanics and Thermodynamics* 35 (2023), pp. 1625–1654. ISSN: 1432-0959. DOI: `10.1007/s00161-022-01178-5`.

[217] Emilio Turco, Emilio Barchiesi, Alessandro Ciallella, and Francesco dell'Isola. "Nonlinear waves in pantographic beams induced by transverse impulses". In: *Wave Motion* 115 (2022), p. 103064. ISSN: 0165-2125. DOI: `https://doi.org/10.1016/j.wavemoti.2022.103064`.

[218] Emilio Turco, Francesco dell'Isola, and Anil Misra. "A nonlinear Lagrangian particle model for grains assemblies including grain relative rotations". In: *International Journal for Numerical and Analytical Methods in Geomechanics* 43.5 (2019), pp. 1051–1079. DOI: `https://doi.org/10.1002/nag.2915`.

[219] Beliz Ugurhan, Aysegul Askan, Aybige Akinci, and Luca Malagnini. "Strong-Ground-Motion Simulation of the 6 April 2009 L'Aquila, Italy, Earthquake". In: *Bulletin of the Seismological Society of America* 102.4 (Aug. 2012), pp. 1429–1445. ISSN: 0037-1106. DOI: `10.1785/0120110060`.

[220] US Army Corps of Engineers. "Gravity Dam Design". In: June (1995).

[221] Nicoló Vaiana, Raffaele Capuano, Salvatore Sessa, Francesco Marmo, and Luciano Rosati. "Nonlinear Dynamic Analysis of Seismically Base-Isolated Structures by a Novel OpenSees Hysteretic Material Model". In: *Applied Sciences* 11.3 (Jan. 2021), p. 900. ISSN: 2076-3417. DOI: `10.3390/app11030900`.

[222] Paola Vannoli, Pierfrancesco Burrato, and Gianluca Valensise. "The Seismotectonics of the Po Plain (Northern Italy): Tectonic Diversity in a Blind Faulting Domain". In: *Pure and Applied Geophysics* 172 (May 2015), pp. 1105–1142. DOI: `10.1007/s00024-014-0873-0`.

[223] Ivan Vlahinić, Jeffrey J. Thomas, Hamlin M. Jennings, and José E. Andrade. "Transient creep effects and the lubricating power of water in materials ranging from paper to concrete and Kevlar". In: *Journal of the Mechanics and Physics of Solids* 60.7 (2012), pp. 1350–1362. ISSN: 00225096. DOI: `10.1016/j.jmps.2012.03.003`.

[224] Jannik Voges, Fabian Duvigneau, and Daniel Juhre. "On the deformation dependency of the diffusion flux in solids at large deformations". In: *Continuum Mechanics and Thermodynamics* 34.3 (May 2022), pp. 829–839. ISSN: 0935-1175. DOI: `10.1007/s00161-022-01092-w`.

[225] J. Z. Wang, D. A. Dillard, and F. A. Kamke. "Transient moisture effects in materials". In: *Journal of Materials Science* 26 (19 Oct. 1991), pp. 5113–5126. DOI: `10.1007/BF01143201`.

[226] Lei Wang, Annan Zhou, Yongfu Xu, and Xiaohe Xia. "One-dimensional consolidation of unsaturated soils considering self-weight: Semi-analytical solutions". In: *Soils and Foundations* 61.6 (2021), pp. 1543–1554. ISSN: 0038-0806. DOI: `https://doi.org/10.1016/j.sandf.2021.09.003`.

[227] Bo Yang, Michele Bacciocchi, Nicholas Fantuzzi, Raimondo Luciano, and Francesco Fabbrocino. “Wave propagation in periodic nano structures through second strain gradient elasticity”. In: *International Journal of Mechanical Sciences* 260 (2023), p. 108639. ISSN: 0020-7403. DOI: `https://doi.org/10.1016/j.ijmecsci.2023.108639`.

[228] Yang Yang and Anil Misra. “Micromechanics based second gradient continuum theory for shear band modeling in cohesive granular materials following damage elasticity”. In: *International Journal of Solids and Structures* 49.18 (Sept. 2012), pp. 2500–2514. ISSN: 00207683. DOI: `10.1016/j.ijsolstr.2012.05.024`.

[229] M. Erden Yildizdag, I. Tugrul Ardic, and Ahmet Ergin. “An isogeometric FE-BE method to investigate fluid–structure interaction effects for an elastic cylindrical shell vibrating near a free surface”. In: *Ocean Engineering* 251.February (May 2022), p. 111065. ISSN: 00298018. DOI: `10.1016/j.oceaneng.2022.111065`.

La borsa di dottorato è stata cofinanziata con risorse del Programma Operativo Nazionale 2014-2020 (CCI 2014IT16M2OP005), Fondo Sociale Europeo, Azione I.1 “Dottorati Innovativi con caratterizzazione industriale”

UNIONE EUROPEA
Fondo Sociale Europeo

Ministero dell'Università
e della Ricerca

PON
RICERCA
E INNOVAZIONE
2014 - 2020